TECHNISCHE
UNIVERSITÄT
WIEN
Vienna | Austria

Dissertation

Quantitative phase and dark-field contrast computed tomography for industrial applications on lightweight materials

carried out for the purpose of obtaining the degree of Doctor technicae (Dr. techn.), submitted at
TU Wien, Faculty of Mechanical and Industrial Engineering, by

Jonathan Glinz, MSc

Mat.Nr.: 01528174

under the supervision of
Priv.-Doz. Dipl.-Ing. Dr.rer.nat. Johann Kastner
Institute of Materials Science and Technology, E308

Vienna, December 2023

Reviewed by

…………………………….	…………………………….
Univ.-Prof. Dr. techn. Guillermo Requena	Univ.-Prof. Dr. Wim Dewulf
Institute of Materials Science and Technology	Manufacturing Processes and Systems
Technische Universität Wien	Katholieke Universiteit Leuven

This work was supported by the federal government of Upper Austria within the framework of the project Phad-CT (FFG grant number: 875432).

I confirm, that going to press of this thesis needs the confirmation of the examination committee.

Affidavit

I declare in lieu of oath, that I wrote this thesis and performed the associated research myself, using only literature cited in this volume. If text passages from sources are used literally, they are marked as such.

I confirm that this work is original and has not been submitted elsewhere for any examination, nor is it currently under consideration for a thesis elsewhere.

I acknowledge that the submitted work will be checked electronically-technically using suitable and state-of-the-art means (plagiarism detection software). On the one hand, this ensures that the submitted work was prepared according to the high-quality standards within the applicable rules to ensure good scientific practice "Code of Conduct" at the TU Wien. On the other hand, a comparison with other student theses avoids violations of my personal copyright.

City and Date

Signature

Acknowledgements

I would like to express my heartfelt gratitude to the following individuals and groups whose unwavering support, guidance, and contributions have played a pivotal role in the completion of this doctoral thesis:

First and foremost, I extend my deepest appreciation to my esteemed supervisors, Sascha Senck, Johann Kastner, and Simon Zabler. Your expertise, encouragement, and dedication to my academic growth have been invaluable throughout this journey.

I would also like to express my sincere appreciation to my dedicated colleagues at work, whose collaboration, camaraderie, and willingness to share knowledge have greatly enriched my research experience. Your collective contributions have been invaluable in shaping the research presented in this thesis.

Special thanks are due to Joachim Schulz, from the company Microworks, for graciously lending experimental equipment critical to the success of my research. Your generosity and support exemplify the spirit of academic collaboration.

Last but certainly not least, I want to express my profound gratitude to my wife, Anna, whose unwavering love, patience, and understanding sustained me throughout the demanding times of my doctoral studies. Your constant encouragement and belief in me were my driving force.

To my family, who have always been a source of love, support, and inspiration, I extend my heartfelt appreciation. Your enduring faith in my abilities and your sacrifices along this journey have been instrumental in my success.

To all those whose names I have mentioned and to countless others who have contributed in ways seen and unseen, I am truly grateful. This thesis would not have been possible without your collective support.

Thank you from the depths of my heart.

Table of Contents

5 Publications and Scientific contribution 43

Abstract

With material properties including high mechanical strength and stiffness at moderate weight, composite materials are commonly selected for applications in the automotive, aerospace, and aeronautics industries. Consequently, the use of composites has been steadily increasing since the early 1980s, with composites currently accounting for roughly 50% of the materials used in modern passenger aircraft by weight. Non-destructive testing of manufactured components is fundamental to ensuring the high safety standards prevalent in these industries. While X-ray computed tomography (XCT) enables high-resolution, three-dimensional visualization, its ability to efficiently examine large industrial components is limited. Alternately, X-ray radiographic testing, while faster, provides only two-dimensional superimposed images with limited material contrast.

This thesis examines the potential of Talbot-Lau grating interferometry (TLGI), which measures the differential phase contrast (DPC) and dark-field contrast (DFC) modality, to overcome some of these limitations. DPC imaging enhances sensitivity to low-density materials, such as polymers, and shows reduced sensitivity to beam hardening artifacts. Conversely, the DFC visualizes X-ray small-angle scattering, potentially revealing sub-resolution structures like micro-cracks and porosity. Furthermore, the DFC signal is a function of the orientation of local microstructures and can therefore provide additional insights about fiber orientation in composite specimens.

The results achieved during this work were published in four scientific papers, providing guidelines and showcasing possible industrial applications for TLGI. These publications include the characterization of composite layup and resin-rich areas in vacuum infusion CFRP, a comparative study on metal artifacts in attenuation and phase contrast XCT, a new method for fast inspection and quantification of out-of-plane fiber waviness, and a study on the detection of porosity in cyanate ester CFRP considering the influence of variations in specimen thickness. The publication of these works is intended to increase the acceptance of TLGI and to take a step towards its application for industrial needs.

Kurzfassung

Verbundwerkstoffe zeichnen sich durch eine hohe mechanische Festigkeit und Steifigkeit bei relativ geringem Gewicht aus und sind dadurch eine gängige Wahl für Leichtbauanwendungen wie z.B. in der Automobil-, Luft- und Raumfahrtindustrie. Die zerstörungsfreie Prüfung von sicherheitskritischen Komponenten ist dabei von grundlegender Bedeutung, um die hohen Sicherheitsstandards, die in diesen Industrien vorherrschen, zu gewährleisten. Die Röntgen-Computertomographie (XCT) hat sich dazu als leistungsstarke Methode etabliert, um Bauteile dreidimensional und in hoher Auflösung zu visualisieren. Zur effizienten Charakterisierung großer industrieller Bauteile ist die XCT durch ihr limitiertes Sichtfeld jedoch oftmals nur begrenzt einsetzbar sowie Faserverbundwerkstoffe in absorptionsbasierten XCT-Messungen typischerweise schlechte Kontrastverhältnisse aufweisen.

Ziel dieser Arbeit ist es einige dieser Einschränkungen durch den Einsatz von Talbot-Lau-Gitterinterferometrie (TLGI) XCT und Radiographie zu überwinden, und damit das Potenzial der Methode für industrielle Anwendungen auszuschöpfen. Durch den Einsatz von TLGI können zwei komplementäre Modalitäten, der differentielle Phasenkontrast (DPC) und der Dunkelfeldkontrasts (DFC), extrahiert werden, welche zusätzliche Information über ein untersuchtes Bauteil liefern. Der DPC weist eine erhöhte Sensitivität zur Unterscheidung von Materialien mit geringer Dichte auf und ist robuster gegen Strahlaufhärtungsartefakte. Der DFC hingegen visualisiert die Röntgenkleinwinkelstreuung, wodurch Strukturen wie Mikrorisse und Porosität kleiner als die Bildauflösung sichtbar gemacht werden können sowie zusätzliche Information über die lokale Orientierung von Mikrostrukturen extrahiert werden kann.

Die im Rahmen dieser Arbeit erzielten Ergebnisse wurden in vier wissenschaftlichen Publikationen veröffentlicht, die als Guidelines für mögliche industrielle Anwendungen der TLGI dienen sollen. Diese Arbeiten umfassen die Charakterisierung des Faserverbundaufbaus und von Reinharz-Bereichen in Vakuuminfusions-CFK, eine Studie zum Vergleich von Metallartefakten in Absorptions- und Phasenkontrast- XCT, eine neue Methode zur schnellen Detektion und Quantifizierung von Faserwelligkeit sowie eine Studie zur Detektion von Porosität in Cyanatester-CFK unter Berücksichtigung des Einflusses von Variationen in der Probendicke. Mit der Veröffentlichung dieser Arbeiten hoffen wir, die allgemeine Akzeptanz der TLGI zu erhöhen und den zukünftig Einsatz in industriellen Anwendungen zu fördern.

1 Introduction

1.1 Motivation and problem statement

The first human-made composite materials are often dated as early as 4900 B.C., when bricks from straw and mud were used for building construction at Sumer in Mesopotamia [1]. Composite materials have since been utilized in various areas of application and have continuously advanced, until in the most recent century, synthetic polymers and first high-performance carbon fibers were developed, forming the basis for current state-of-the-art fiber-reinforced polymers (FRPs) [2]. At moderate weight compared to, for example, metallic construction materials, these advanced composites feature a variety of favorable material properties, including corrosion resistance and high mechanical strength and stiffness at improved fatigue life [1,3,4]. As the reduced material weight can ultimately result in higher payloads, consequently enabling lower fuel consumption and reduced CO_2 emissions, composites like carbon fiber-reinforced polymers (CFRPs) are consistently utilized in industries including automotive, aerospace, and aeronautics. As illustrated in Fig. 1, the use of composites in passenger aircraft has been steadily increasing since the early 1980s [5]. Today, composites account for roughly 50% of the materials used in modern passenger airplanes by weight—for example, a total of 32 tons of CFRPs in a Boeing 787 [6].

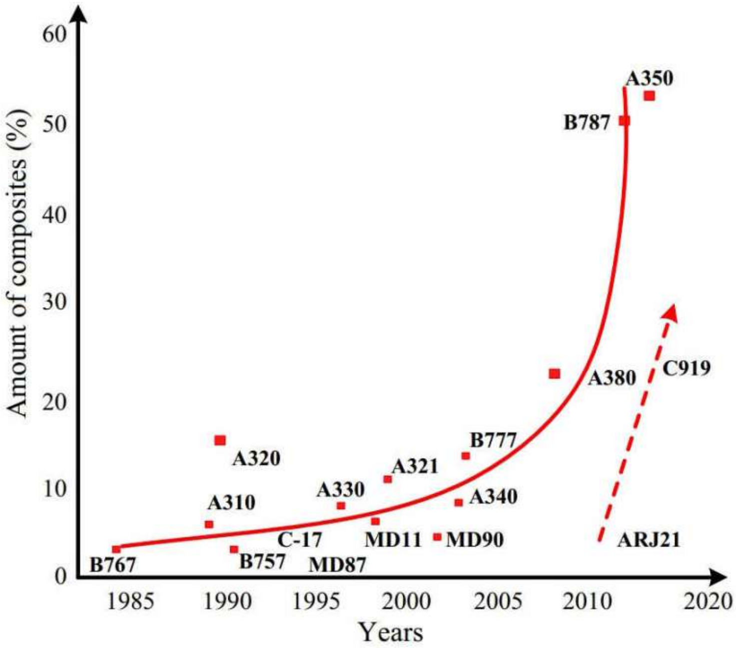

Fig. 1: Development of the composite amount by weight used in commercial passenger aircraft. (Image adapted and reprinted from [5] with permission from Springer Nature)

However, composite materials are not completely without shortcomings; their increased complexity makes them prone to internal defects and part-to-part variations, such as porosity, delamination, resin-rich areas, insufficient fiber impregnation, and fiber misalignment. This is even more the case if foreign materials, such as embedded electronics or metallic conductors for lightning protection, are introduced into a composite component. Consequently, in high demanding applications, as are often found in the automotive and aerospace industries, verification of manufactured components by non-destructive testing (NDT) methods is essential. For example, space applications often require the porosity content in finished components not to exceed 1–2% [7,8]. Furthermore, composites are susceptible to damages occurring during use, which means regular monitoring is typically required throughout the component's lifetime. In particular, impact damage (e.g., from flying debris or bird strike) can be a cause for microscopic matrix cracking that is invisible to the eye but severely reduces mechanical strength.

Therefore, a multitude of NDT methods have emerged, each with individual strengths and limitations, which is why developments of new, superior techniques are still in demand. Typical shortcomings of currently employed methods are the limited depth, field-of-view, and resolution of the evaluation; the need for direct contact of the probe (e.g., via coupling agents as in ultrasonic testing); and restrictions to conductive materials, as in eddy current testing [9]. X-ray computed tomography (XCT) and X-ray radiographic testing (XRT) are among the most versatile technologies for testing of CFRPs. XCT offers the ability to visualize internal structures of a specimen three-dimensionally, with a detail detectability of structures down to, and possible smaller than, 1 µm in size [10]. However, such high resolution is typically only achievable for relatively small specimens (≤ 1 mm in diameter), and industrial CFRP components are often too large to be inspected within a reasonable time and with the necessary detail. Using XRT, components can be investigated in a shorter time, but the results are superimposed, two-dimensional image data of three-dimensional objects or structures. Furthermore, the contrast between materials of similar density is typically low in standard attenuation-based radiographic imaging methods.

Some of these limitations may be overcome by measuring the complementary differential phase contrast (DPC) and dark-field contrast (DFC) modalities, for example, via Talbot-Lau grating interferometry (TLGI). The DPC modality is sensitive to the refraction of X-rays and, compared to standard attenuation contrast (AC) methods, offers higher sensitivity to low density and low atomic number materials. Consequently, better contrast and material differentiation can be achieved for specimens consisting of polymers or biological tissue [11,12]. Moreover, the influence of the X-ray energy on the DPC signal is lower than that on the AC, making the DPC more robust against artifacts caused by beam hardening [13,14]. In contrast, the DFC is sensitive to small-angle scattering caused by structures smaller than the actual system resolution. Consequently, structures like micro-cracks or porosity of size below the system resolution can possibly be detected in the DFC modality [15–17]. Furthermore, the scatter signal caused by a structure is influenced by its orientation in space, which can be utilized, for example, for investigations of fiber orientation in composite specimens [18–20]. A few examples for the use of TLGI are given in Fig. 2.

Fig. 2: Examples for the application of TLGI: **(a)** Radiography of a carbon fiber-reinforced polymer plate, including fiber waviness in five regions. Due to the directional sensitivity, dark-field visibility is reduced in regions featuring fiber waviness and therefore appears darker. **(b)** Three-dimensional visualization of fiber layup via DFC (left) and resin-rich areas via DPC (right) in a vacuum infusion CFRP specimen. **(c)** Comparison of beam hardening artifacts in a polymer specimen, including four metallic inserts. Attenuation-based XCT is shown on the left compared to DPC XCT on the right.

However, the extraction of the DPC and DFC modalities requires elaborate measurement setups and protocols. Over the past decades, several such methods applicable to laboratory X-ray devices have been developed, but they have yet to be established for industrial applications.

1.2 Aim of this work

Given the relative novelty of Talbot-Lau grating interferometry and its limitations, for example, in field-of-view (FOV), applicable X-ray energies, and lack of standard protocols, applications of this method are not yet well established for industry applications. Therefore, to increase the acceptance of this promising method, optimization of the systems' hardware components, measurement setup and protocols, as well as postprocessing and evaluation methods, is needed. Consequently, the overall aim of this thesis is to provide comprehensible guidelines and demonstrate use cases of TLGI with a focus on industrial lightweight materials. These include methods of full TLGI computed tomography for a three-dimensional, in-depth characterization of specimens as well as two-dimensional radiographic testing to provide means for fast investigation of larger components.

Computed tomography is used to examine structural features in fiber-reinforced polymers that are of poor detail and contrast in standard attenuation-based XCT, such as fiber orientation within the layer sequence and the visualization of inhomogeneities (e.g., resin-rich areas). Furthermore, metal artifacts in metal-polymer composites—which are a common problem in attenuation-based imaging—are investigated and compared. Thereby, the insensitivity of phase contrast imaging to beam hardening effects will be elucidated. Since computed tomography requires several hundreds or even thousands of projection images to be recorded, measurement times are typically long, especially for industrial applications. Therefore, this work further intends to provide non-destructive testing methods that rely on radiographic imaging, possibly at only a few tens of projection angles. These methods will focus on the characterization of fiber waviness and porosity in carbon fiber-reinforced polymers which are common defect types known for their negative influence on mechanical strength. A new method for characterizing out-of-plane fiber waviness, alongside a comprehensive study of the effects of specimen porosity on all three imaging modalities obtained by TLGI, will provide a basis for faster, more detailed characterization of CFRP components.

To this end, this doctoral thesis covers the basics of composite materials, their non-destructive testing, and X-ray radiographic methods in Chapter 2, followed by an introduction to X-ray phase contrast imaging (PCI) with a focus on Talbot-Lau grating interferometry in Chapter 3. Chapter 5 summarizes the research output and findings of this work, including the investigation of composite layup and resin-rich areas in vacuum infusion CFRP via TLGI computed tomography, a comparative study on metal artifacts in attenuation and phase contrast XCT, a new method for fast inspection and quantification of out-of-plane fiber waviness via dark-field contrast radiography, and an investigation of porosity in cyanate ester CFRP via TLGI radiographic testing considering the influence of variations in specimen thickness on the measured radiography data.

2 Composite materials and their non-destructive testing

Composites can be considered the most important and most heavily researched material in modern technology. As their characteristics are largely adaptable to individual requirements, composite applications can be found in a wide range of industrial fields, including automotive, aerospace and aeronautics, construction, sports equipment, and biomedical [21]. Consequently, a variety of composite materials and material combinations aiming to satisfy different industrial needs are available on the market. Generally, composites can be classified into four types [22]:

(1) Matrix materials reinforced by fibers

(2) Matrix materials reinforced by particles

(3) Laminates from layers of two or more different materials

(4) Combinations of the above

However, the focus of this work primarily is on the investigation of fiber-reinforced polymers.

2.1 Fiber-reinforced composite materials

Fiber-reinforced composites can be differentiated according to the matrix material type and the embedded fiber material, shape, and arrangement within the composite. While the fibers are the main load-bearing structure of a composite, the matrix material is designed to provide protection and support for these fibers and to distribute applied loads between them. In the case of individual fiber breakage, the load previously carried by the fiber is transferred to the surrounding matrix and subsequently distributed to surrounding fibers [22]. Although matrix materials can be of metallic or ceramic nature, polymeric matrix materials are most common. These can be further categorized as thermosetting or thermoplastic polymers. Thermoset composite materials have prevailed over many metallic alternatives due to their higher strength and stiffness and the associated possibility of weight reduction. However, thermoset composites are susceptible to impact damage due to the brittleness of the matrix, which often leads to delamination, especially between differently oriented layers [23]. Furthermore, thermosetting polymers are typically cured under high heat and pressure and, once fully hardened, cannot be reprocessed. In comparison, composites from thermoplastic matrix materials can be remolten and reshaped, consequently offering higher flexibility in recycling or repairing damaged structures [24,25]. Although this flexibility comes at the cost of high-temperature resistance, the strengths of thermoplastic composites lie in their increased fracture toughness and fatigue strength [24]. Furthermore, short fiber-reinforced thermoplastics can be easily implemented for high volume production, for example, via injection molding.

The main reinforcement materials used in industrial applications are carbon, glass, and aramid fibers, although demand for natural, biodegradable composite materials has increased with awareness for sustainable production [26]. These fibers can be embedded in continuous form as sheets of unidirectional (UD) or woven fiber cloth, or as discontinuous fibers. Discontinuous fibers can be distinguished as either short (sometimes referred to as "chopped") and long fibers. Fig. 3 shows schematic examples of continuous and discontinuous fiber reinforcement, including a fabric woven from 0°/90° oriented fibers. More complex weaving patterns with more than two main fiber orientations are also possible.

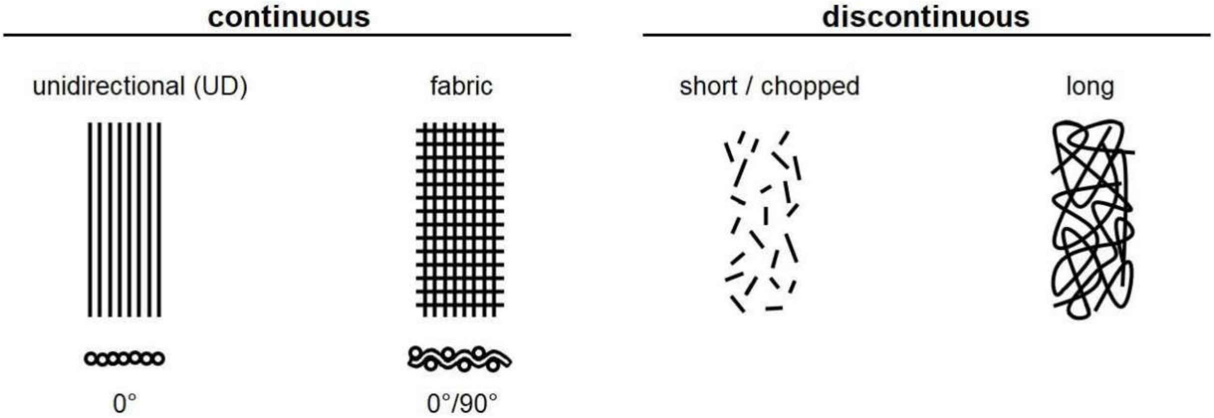

Fig. 3: Examples for continuous and discontinuous fiber reinforcement. (Image inspired by [1])

Compared to woven fiber fabrics, UD fibers, sometimes referred to as "non-crimp" fibers [27], show the highest strength in fiber direction, as woven fiber structures are weakened by undulation. However, UD fiber composites are susceptible, for example, to matrix fractures owing to low shear strength and tensile strength in the transverse direction [27]. Consequently, continuous layers or plies of fibers are commonly stacked to form a laminate structure with fiber orientations designed to achieve desired strength and stiffness for the intended application. Tapes or filaments of UD fibers can also be woven in winding processes, as is the case, for example, with carbon fiber-overwrapped pressure vessels [28,29]. Fig. 4 displays a schematic of an exemplary composite layup from continuous UD plies in a quasi-isotropic arrangement.

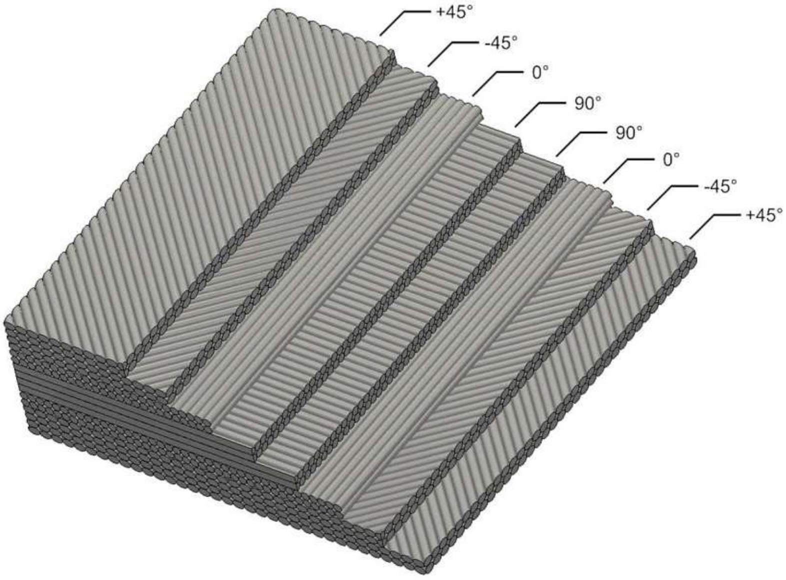

Fig. 4: Schematic of an exemplary composite layup from continuous unidirectional plies in a quasi-isotropic arrangement of [+45°/-45°/0°/90°]2S.

There is no generally accepted length that distinguishes between long and short discontinuous fibers. Some authors state that fibers of 5–20 mm length in a finished component can be considered long fibers [30], while others characterize the fibers according to their shape and interaction between each other. According to the latter, short fibers tend to be straight and show little interaction between fibers, while long fibers can be significantly curved and show more interaction [31]. Discontinuous fibers are typically randomly oriented, as in fiber spaying or sheet molding processes [32,33], which is why the fibers cannot be as densely packed and fiber volume content is typically low [34]. Consequently, discontinuous fiber-reinforced composites have lower strength and stiffness in comparison to their continuous fiber counterparts and are predominantly used in high-volume production and low-cost applications [34]. However, injection-molded discontinuous fibers can show some anisotropic alignment based on material flow direction during mold filling as well [31,35].

2.2 Manufacturing and typical defects in fiber-reinforced composites

Based on the structural demands and complexity of a composite component, different types of manufacturing methods have established. However, a full review of the existing methods considering all their various factettes is beyond the scope of this work. Therefore, this chapter includes only a brief overview of the most significant methods. Generally, methods for thermoplastic and thermosetting composites are distinguished since not all methods are applicable to both material types. For thermosetting composites, open molding via hand or spray layup is commonly used for large components of low complexity, while resin infusion methods allow for production of components of more complex shape [36]. Large, high-performance composites, such as those used in the aerospace industry, are mostly fabricated by automated tape laying of preimpregnated sheets of continuous fibers, which are subsequently cured in an autoclave. One of the main advantages of thermoplastic composites is the possibility of their compression molding or injection molding for cheap, high-volume manufacturing. Filament winding and pultrusion methods for producing profiles of constant cross-section exist for both material types [37,38]. Furthermore, additive manufacturing methods, such as fused filament fabrication, have recently been extended to enable the integration of both short and continuous fiber reinforcement in both thermosetting and thermoplastic materials [39].

Depending on these manufacturing methods, different defects in the composite structure can be introduced during production, thus affecting the properties of the final component. An overview of manufacturing defect types and their typical scale is given in Fig. 5.

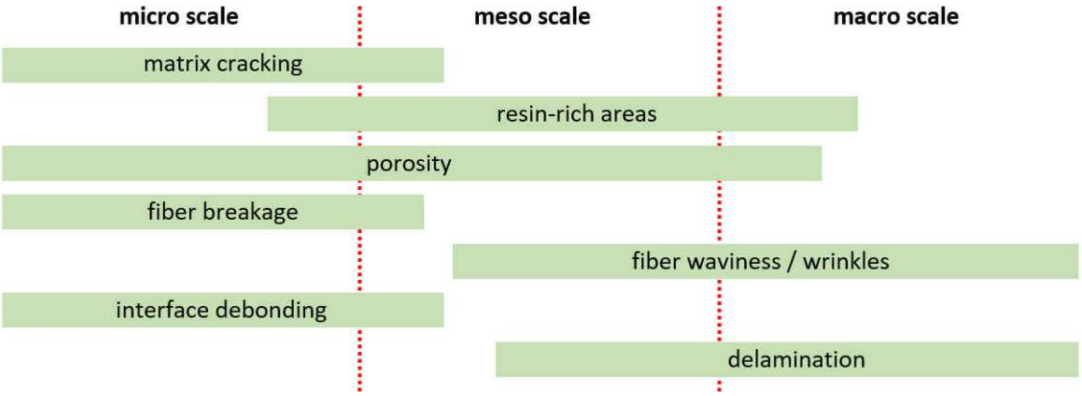

Fig. 5: Overview of common manufacturing defects occurring in FRPs according to their typical scale. (Image inspired by [40])

These defects can be related to the fiber material, matrix material, or the interface between them. Although no manufacturing method can guarantee the absence of manufacturing defects, some are more or less susceptible to certain defect types. In injection molding, for example, fibers are susceptible to breakage during injection. Consequently, average fiber length in a finished injection molded part will always be shorter than in the raw material [41]. Laminated composites, in contrast, are naturally prone to delamination because of their low inter-layer shear and tensile strength [40]. Fiber waviness is one of the most encountered and most significant fiber-related manufacturing effects in continuous FRPs and, depending on the severity, can also be considered a defect. Waviness can form in-plane and out-of-plane in reference to ply orientation, but out-of-plane waviness is more common, as the bending stiffness of fibers is higher in-plane of plies than out-of-plane [42]. Causes for waviness or wrinkles in

FRPs are manyfold and include internal stress due to mismatching thermal expansion coefficients (between differently oriented fiber layers or fiber and matrix material), interactions between the component and tool, path length differences at curvatures, consolidation at corners and radii, or embedded foreign objects that distort the fiber layup [42–44]. Fig. 6 provides an example of an infusion-assisted resin transfer-molded specimen with out-of-plane waviness.

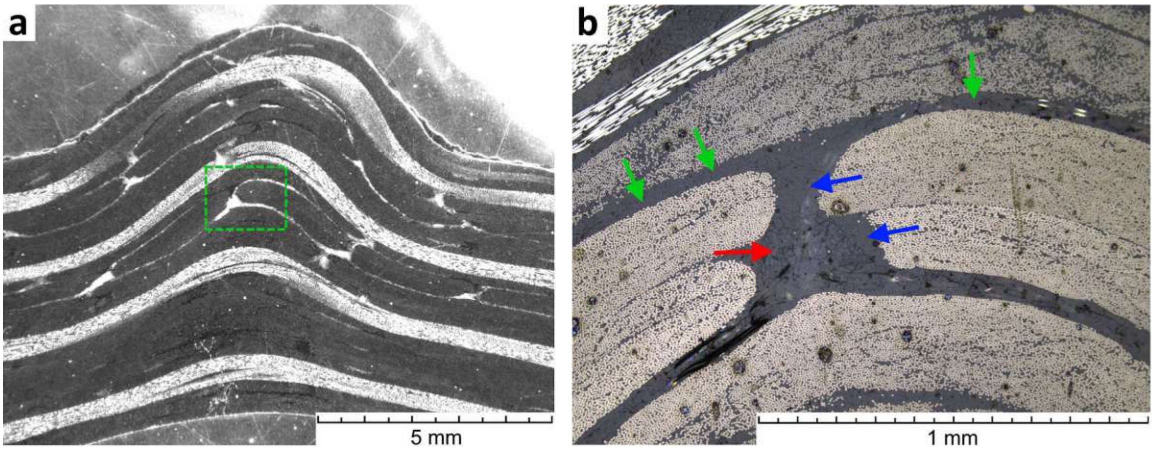

Fig. 6: (a) Microsection of an infusion-assisted resin transfer-molded CFRP specimen showing significant out-of-plane fiber waviness. **(b)** Zoomed section of the specimen revealing resin-rich areas within layers (blue arrows) from fiber consolidation by binder yarns (red arrow), and between layers (green arrows) from gaps caused by out-of-plane waviness.

Defects that typically occur within the matrix material are porosity (e.g., macro porosity between layers of a laminate or micro porosity between individual fibers of a fiber bundle), inclusions of foreign material, and resin-rich areas. Resin-rich areas can be formed in different shapes and sizes depending on the type of fiber reinforcement and the manufacturing process. As shown in Fig. 6, misalignments between layers of fiber reinforcement caused by fiber waviness often leave gaps in the laminate that are filled with resin during infusion, creating resin-rich areas. Another cause of resin-rich areas is the collimation of fibers by binder yarns, which results in voids lacking fibers that also fill with resin during infusion [45]. Furthermore, when foreign structures that are thicker than the actual fiber reinforcement or plies are integrated into a laminate, the resulting deviations in the composite structure can cause similar effects, such as those recently observed in composites with embedded electronics [46] or optical fibers [47]. [48]

Voids or porosity in composites typically originate from air entrapped during layup or impregnation, or from moisture and volatiles emerging from the resin during curing [40,49]. Thus, thermosetting composites cured within an autoclave under high temperature and pressure typically show lower porosity than out-of-autoclave cured composites [49]. Conversely, thermoplastic composites are more prone to insufficient impregnation resulting in porosity within the material because of the high viscosity of the polymer compared to thermosetting resins [50]. In fused filament fabrication additively manufactured FRP, macro porosity is predominantly caused by inter-bead or inter-layer gaps [10,51], as shown in Fig. 7a. Micro porosity between carbon fibers of the continuous fiber reinforcement can also be found. Fig. 7b shows an XCT cross-section of a preimpregnated thermoplastic carbon fiber filament, as used for manufacturing of the specimen in Fig. 7a. Micro porosity is already inherently present in the prepreg material due to insufficient impregnation of the carbon fibers, leaving dry fibers with voids in between [10].

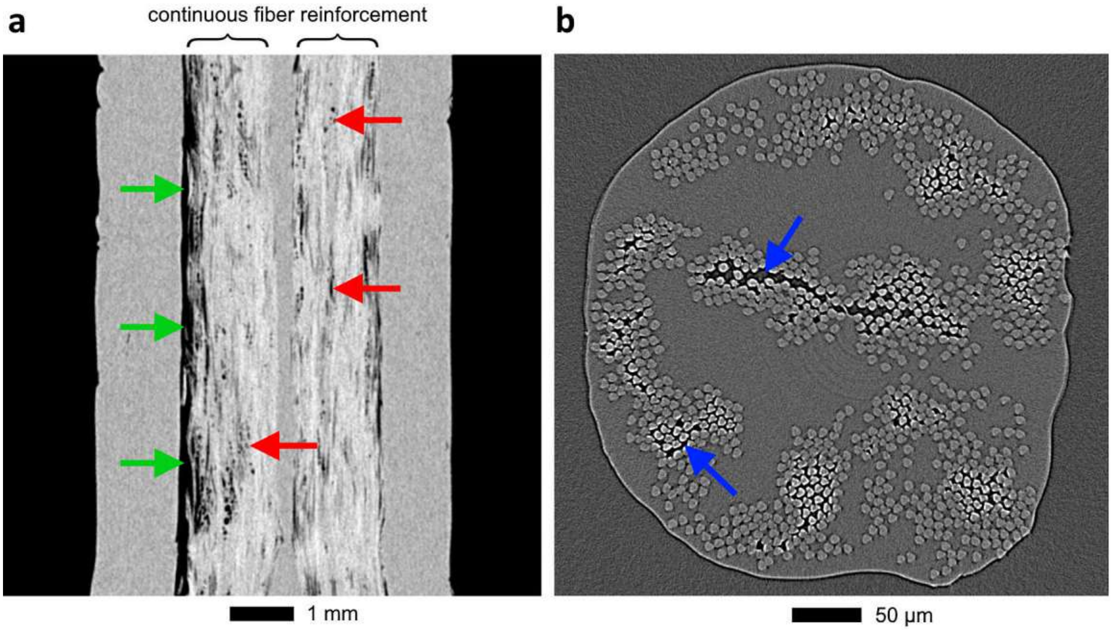

Fig. 7: **(a)** XCT cross-sectional image of a fiber-reinforced, additively manufactured component. Two rovings of continuous carbon fibers are vertically aligned in the center. Macro porosity (green arrows) caused by gaps between continuous fiber rovings and matrix material is visible as is micro porosity (red arrows) between individual fibers of the rovings. **(b)** XCT cross-sectional image of a preimpregnated continuous carbon fiber filament. Insufficient impregnation leads to voids between dry fibers (blue arrows).

It has been widely shown that mechanical properties of a FRP component are directly related to the void content and its distribution within the component [49,52,53]. Therefore, high-demand industries (like aerospace and aeronautics) typically require a void content of less than 1–2% in primary structural components [7,8]. In addition, voids in FRPs often form an interconnected network that can serve as a pathway for moisture ingress, promoting further degradation of the material properties [54].

Apart from inherently existing manufacturing defects, damage during use can also induce component failure. Damages occurring in FRPs largely depend on their application but, especially in the aerospace and renewable energy sector, impact damage, thermal damage, and damage from lightning strike are common [4,55]. Composites have been found to be highly susceptible to impact forces, which can cause barely visible microcracks that significantly weaken the structure and are one of the main causes of unexpected early component failure. Residual compression strength can be reduced to as much as 30% of the original material value [56]. Such barely visible damage can be caused by high-velocity impact from debris or bird strike in aerospace applications, as well as low-velocity impact (e.g., caused by tool drop). For wind turbines, lightning strikes are one of the most serious threats causing decomposition of the matrix resin, fiber damage, surface ablation, and delamination [4,57,58]. Furthermore, damage can be induced by machining of composite materials. Fibers and matrix have different ablation mechanisms, which constantly change during processing because of the anisotropy of the material. As a result, defects such as fiber pullout, matrix burning, delamination, burrs, and matrix cracks frequently occur, causing poor cut surface quality and reducing assembly tolerance and fatigue strength, for example, of drillholes[59,60]. A graphical overview of typical damages encountered in composites is given in Fig. 8.

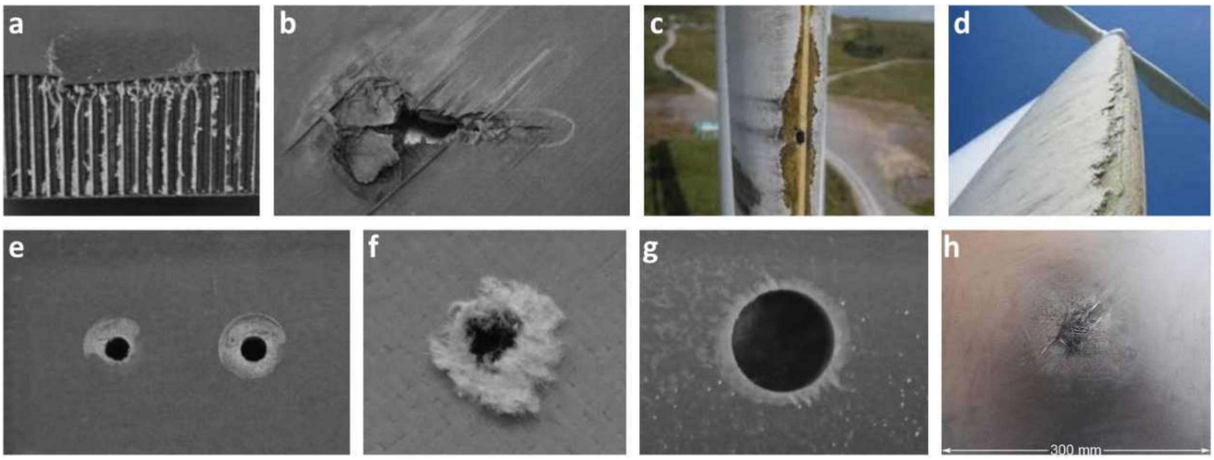

Fig. 8: Overview of typical composite damages. **(a)** Impact damage on a sandwich composite; **(b)** projectile damage; **(c-d)** erosion on wind turbine blades; **(e)** surface damage from fasteners; **(f)** fiber fuzzing from drilling; **(g)** damage on drill-hole exit site; **(h)** lightning damage. (Images **(a–g)** adapted and reused from [61] under CC BY 4.0. Image **(h)** reprinted from [4] with permission from Elsevier.)

2.3 Non-destructive testing

Non-destructive testing involves the detection and characterization of defects and damages in components while maintaining their physical integrity so they can subsequently be put to their intended use [44]. This chapter provides a basic overview of NDT methods for fiber-reinforced polymers, as well as a more detailed introduction to X-ray radiographic testing and computed tomography. Generally, different defect and material types will require different NDT approaches; therefore, a multitude of methods have been established in various industries. While surface defects of macroscopic scale can often be detected by visual inspection, internal and microscopic defects typically require more elaborate NDT methods. However, many of these methods can complement each other, and utilizing multiple inspection methods to investigate a specific component is common. Fig. 9 shows an overview of established NDT methods for FRP and the approximate scale of defects that can be detected by their application.

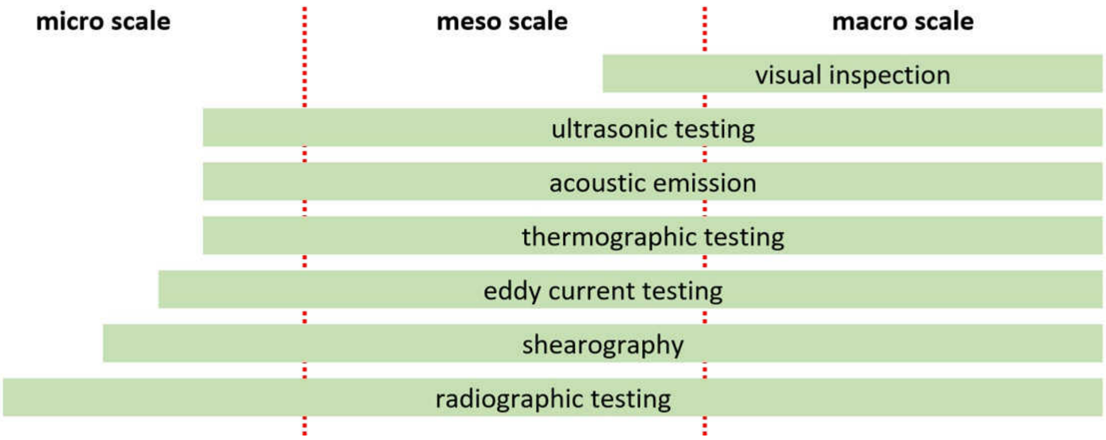

Fig. 9: Overview of NDT methods for FRPs arranged in order of detectable defect scale. (Image inspired by [40])

Among these methods, ultrasonic testing (UT) can be considered the most-established NDT method for in-service inspection of aerospace components, although thermographic and eddy current methods are also capable of detecting defects, possibly down to the micrometer scale. Both UT and eddy current testing are approved methods for detecting and quantifying fiber waviness in CFRP [44,62]. Thermographic imaging and UT have also proven to be capable of porosity estimation in CFRP [54,63], [53,62], and efforts to enable three-dimensional tomographic reconstruction from thermographic imaging have been made [64,65]. Acoustic emission is typically used for in-service monitoring, as damages occurring in components can be observed and located during their formation [66]. However, static defects, which do not emit acoustic signals, will be undetected. While shearography is technically mature for aerospace applications, it is in competition with existing methods of ultrasonic inspection. The advantages of shearography are a contactless inspection providing direct two-dimensional information, while among the mentioned methods, the largest FOVs can possibly be covered in a single acquisition [67]. Additionally, the possibility to detect impact damage and delaminations makes shearography a natural choice for in-service applications [67].

The ability to reconstruct three-dimensional data from a series of radiographic images makes XCT the most versatile method for inspecting damages and defects. Typical examples of NDT via XCT and XRT are the inspection of weld lines [68], porosity and damage in FRP [69–71], and adhesive bonds [72,73]. However, while mobile solutions exist for radiographic methods, XCT devices are typically stationary and limited to rather small components. The following subsection will provide a more detailed introduction to radiographic imaging.

2.3.1 X-ray radiographic testing and computed tomography

The basic principle of radiographic imaging relies on the differences in attenuation of X-rays between two or more materials. The attenuation of an incident X-ray beam of intensity I_0 can be described by Beer-Lambert's law:

$$I_1 = I_0 \cdot e^{-\mu t} \tag{2.1}$$

where I_1 is the remaining intensity after propagation through an object of thickness t with the attenuation coefficient μ. The attenuation coefficient μ is a function of the material's atomic number A and density ρ, and the applied X-ray photon energy E or its X-ray wavelength λ, respectively, which is inversely proportional to the photon energy as follows:

$$\lambda = \frac{h \cdot c}{E} \tag{2.2}$$

with the Planck's constant h and the speed of light c. Thus, at a given X-ray photon energy, contrast formation depends only on material constants and transmission length. A schematic overview of the effects of these parameters on the attenuation of X-rays is shown in Fig. 10. Based on this principle, intensity changes caused by foreign materials or voids inside a component can be detected in radiographic images.

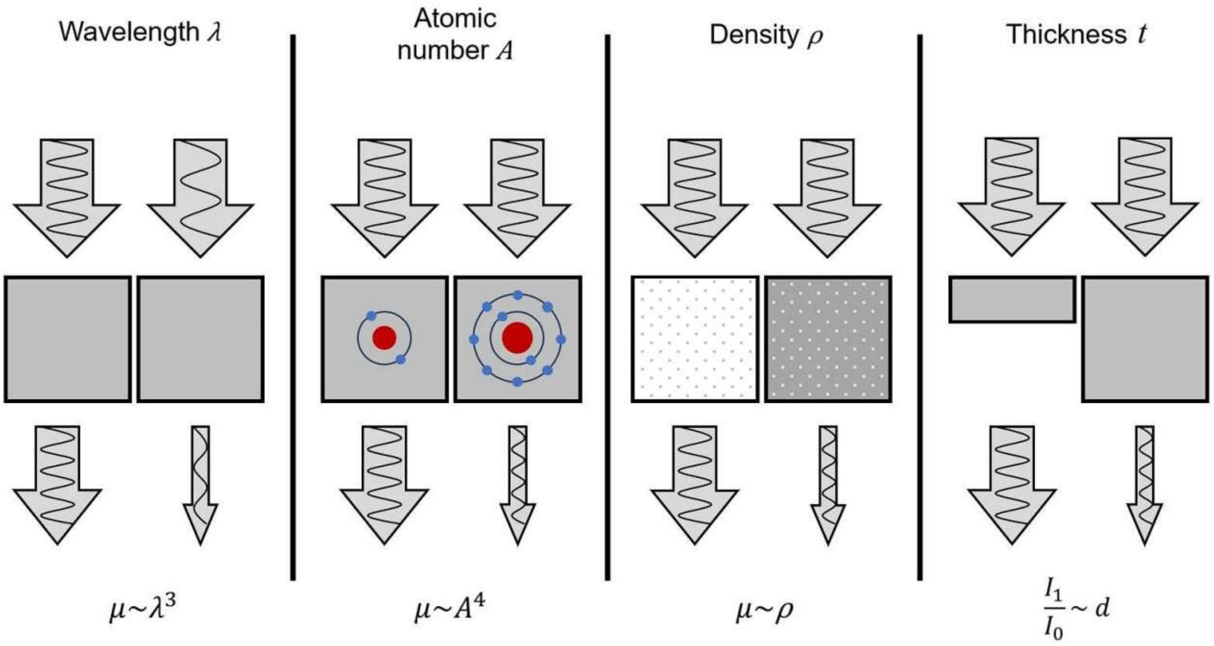

Fig. 10: Schematic overview visualizing the effects of different material and X-ray parameters on the attenuation of X-rays (Image inspired by [74])

However, radiographic images provide information of a three-dimensional object superimposed on a two-dimensional image. Consequently, to retrieve three-dimensional information, tomographic reconstruction can be performed. Most industrial XCT systems operate an X-ray tube emitting X-rays in a cone beam geometry which is why the method often is also referred to as cone beam XCT. The specimen under investigation is placed on a high-precision rotary stage between the X-ray source and a flat panel detector for image acquisition as schematically shown in Fig. 11. Because of the cone beam geometry, the projection image cast onto the detector experiences a magnification by the factor M, depending on the source-to-object distance (*SOD*) and the source-to-detector distance (*SDD*) as follows:

$$M = \frac{SDD}{SOD} \quad . \tag{2.3}$$

Consequently, the imaging resolution of an XCT measurement can be adjusted by varying this distance ratio. However, due to the limited size of the detector, an increase in image resolution usually comes with a reduction in the covered FOV. Therefore, microscopic defects in large components might be difficult to detect by conventional radiographic methods, which is why special developments capable of detecting micro scale defects in large field-of-views are still demanded [15].

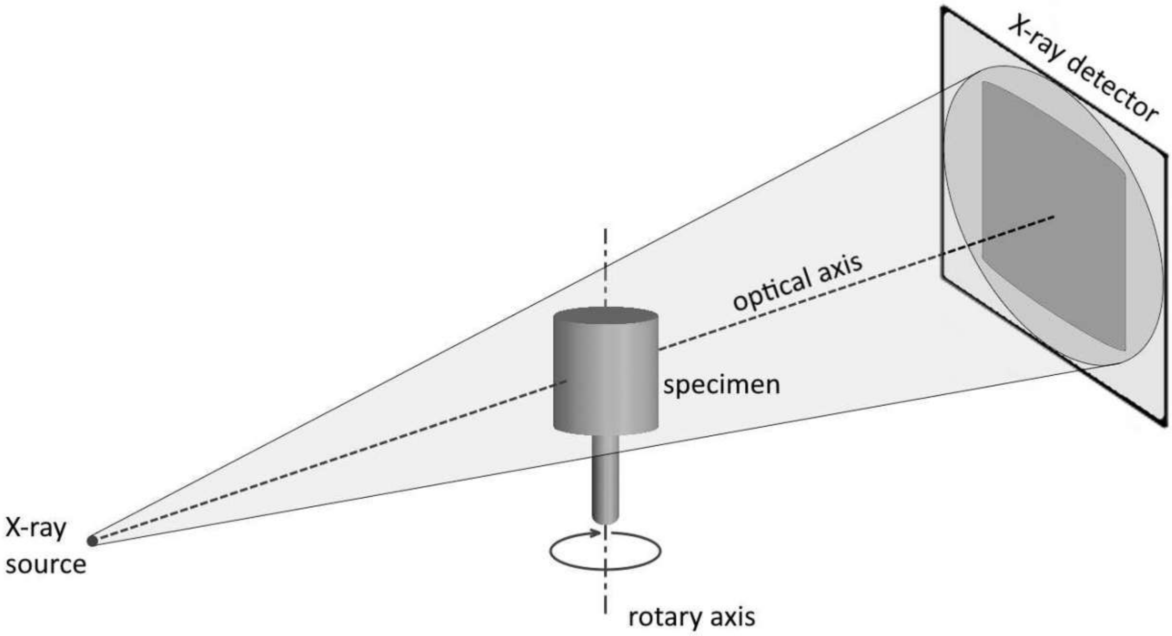

Fig. 11: Schematic image of a cone beam XCT system. The specimen or object is placed on a rotary stage between the X-ray source and a flat-panel X-ray detector.

To enable tomographic reconstruction, radiographic projection images are usually recorded over a 360° rotation of the specimen at angular steps of a fraction of a degree. The most commonly applied reconstruction algorithm was introduced by Feldkamp, Davis, and Kress (FDK) [75] which filters the projection images and performs a back projection into the three-dimensionally reconstructed space [76]. However, there are also a multitude of other reconstruction algorithms developed and used.

As previously mentioned, Beer-Lambert's law is valid only for a discrete X-ray photon energy, but typical laboratory X-ray sources generate a polychromatic spectrum. Consequently, as a polychromatic beam propagates through a material, X-rays of low photon energy are attenuated more easily than high energy photons, leading to an increase in the mean energy of the spectrum. This effect is referred to as beam hardening and is one of the most important factors causing artifacts in XCT that appear as grey value gradients in otherwise homogeneous materials (see Fig. 12a) and black and white streaks or bands especially between materials of high attenuation (see Fig. 12b) [14]. These artifacts can lead to the impression of changes in density within a homogeneous material or obscure other features of a specimen and thereby hinder proper characterization. However, there are many more causes for different artifacts in XCT. A brief overview of the most important ones is given in Fig. 12.

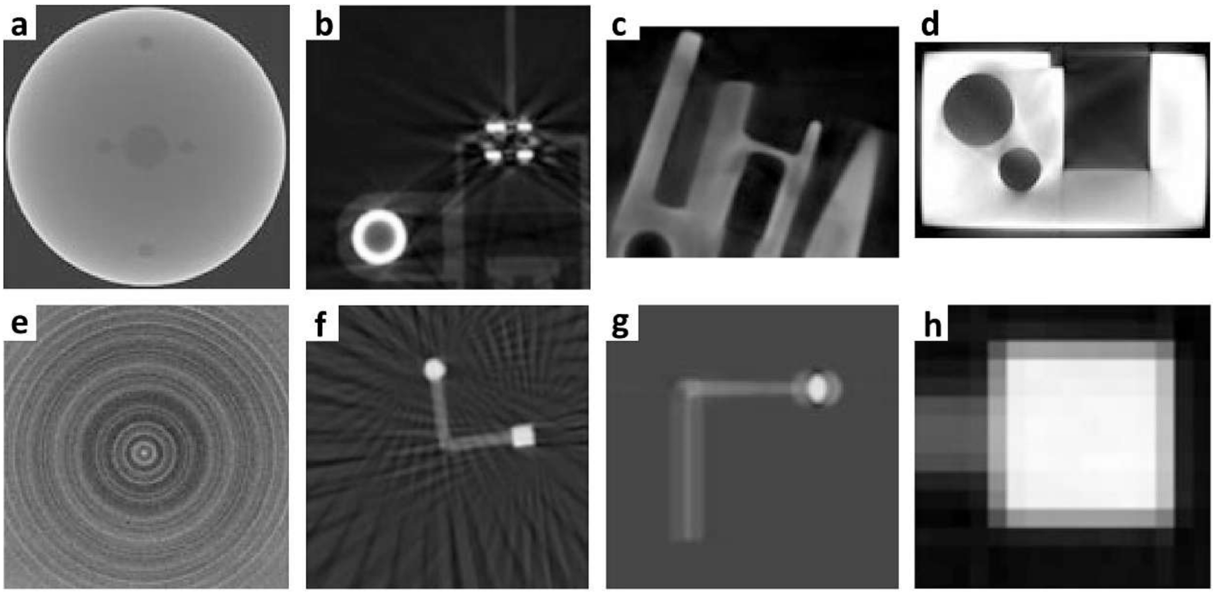

Fig. 12: **(a)** Cupping artifacts caused by beam hardening; **(b)** Streak artifacts caused by beam hardening and amplified by high pass filter during FBP reconstruction [77]; **(c)** Scattered radiation artifacts**;** **(d)** Cone beam reconstruction artifacts; **(e)** Ring artifacts caused by nonlinear or defect X-ray detector pixels; **(f)** Anti-aliasing artifacts from insufficient number of projections; **(g)** Specimen motion artifacts; **(h)** Partial volume artifacts from insufficient X-ray detector resolution. (Image adapted and reprinted from [76] with permission from Springer Nature)

3 X-ray phase contrast and dark-field imaging

3.1 Basic principles

While for the formation of image contrast in conventional radiographic methods, differences in the attenuation of X-rays are measured, phase contrast and dark-field imaging rely on differences in refraction and small-angle scattering, respectively. Consequently, for materials with similar attenuation coefficients or low thickness that cannot be distinguished via conventional radiographic imaging, the extraction of phase- and dark-field contrast can yield additional information for NDT. The following subchapters will provide an introduction to the basic principles of X-ray refraction and small-angle scattering necessary to understand and measure these additional modalities.

3.1.1 Phase contrast imaging

The X-ray phase contrast modality can best be explained by the refractive index, which is defined as:

$$n = 1 - \delta + i\beta \quad . \tag{3.1}$$

While the attenuation of X-rays is explained by the imaginary part β of the refractive index via the attenuation coefficient

$$\mu = \frac{4\pi\beta}{\lambda} \quad , \tag{3.2}$$

the phase shift within a wave front Φ is represented within the refractive index decrement δ of the real part via the linear phase-shift coefficient

$$\psi = -\frac{2\pi\delta}{\lambda} \quad , \tag{3.3}$$

including the X-ray wavelength λ [78]. Consequently, an X-ray wavefront propagating through a material with defined, homogeneous linear phase-shift coefficient and thickness t experiences a phase shift equal to [78]

$$\Phi = \psi \cdot t \quad . \tag{3.4}$$

The refractive index decrement then again is a function of the electron density ρ_e of the material transmitted which far from absorption edges of the material can be approximated by

$$\delta = \frac{r_e \rho_e \lambda^2}{2\pi} \quad , \tag{3.5}$$

with the constant classical electron radius r_e [79].

Looking at X-rays as waves propagating through a material with refractive index n, the phase shift Φ within the wavefront after an object represents the change in phase of an X-ray wave after passing through the material with respect to its incident wave form as depicted in Fig. 13.

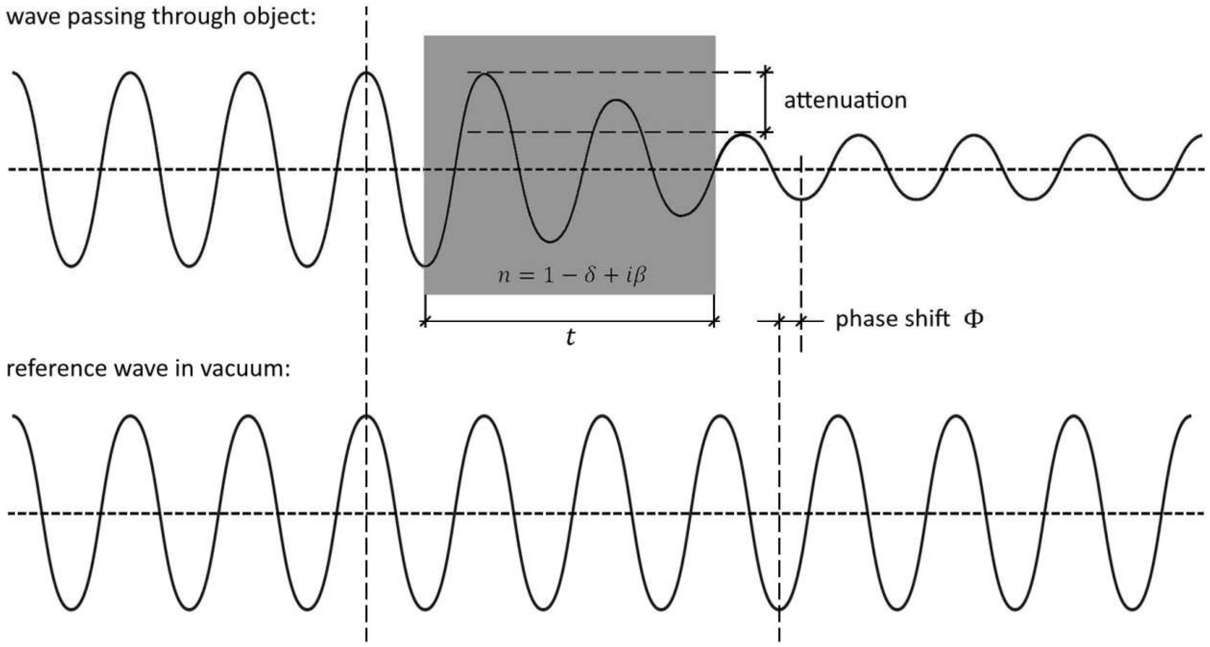

Fig. 13: X-ray wave passing through an object of refractive index n (top) in reference to the same wave propagating through vacuum (bottom). The phase shift Φ caused by the object relative to the reference wave as well as the effects of attenuation are indicated. (Image inspired by [80])

Alternatively, phase effects can also be visualized in terms of refraction of X-rays, since a phase shift in the wave front also leads to a local change in propagation direction of incoming X-rays, which is always perpendicular to the wave front. This change in the propagation direction can be expressed as refraction angle α as schematically introduced in Fig. 14. Thus, for thin objects in a parallel beam geometry and under the small-angle approximation, the refraction angle α relates to the phase shift within the wave front via [13]

$$\alpha = \frac{\lambda}{2\pi} \frac{\Delta\Phi}{\Delta x} \quad , \tag{3.6}$$

where $\Delta\Phi/\Delta x$ is the differential phase shift in lateral direction as indicated in Fig. 14 [13].

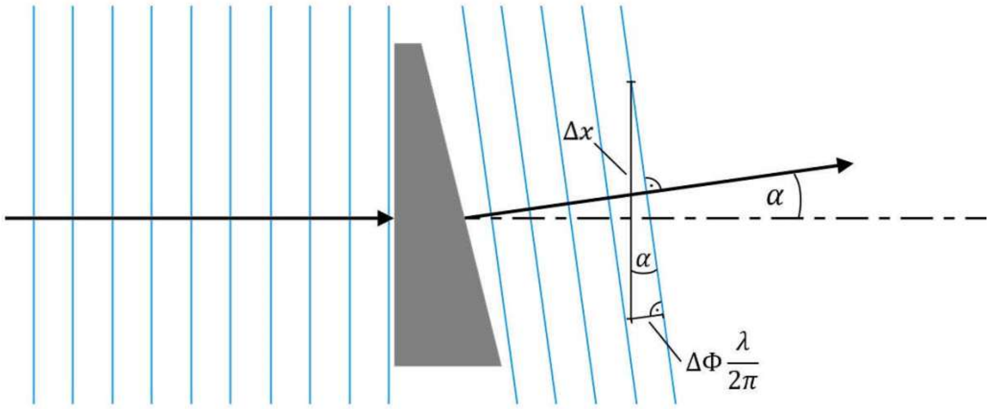

Fig. 14: Object inducing a phase shift to an incoming plane wave which causes refraction of the X-ray beam at angle α as the propagation direction is always perpendicular to the wave front. The refraction angle is proportional to the difference in the optical path $\Delta\Phi \cdot (\lambda/2\pi)$ at a lateral beam distance Δx [11]. (Image inspired by [11])

In terms of X-ray interaction cross sections, the phase cross section σ_p and attenuation cross section σ_a, show significantly different dependencies on X-ray energy as shown in Fig. 15 by Mayo et al. [78]. Especially for low atomic number materials, σ_p is up to three magnitudes higher than σ_a [81,82]. Consequently, for these materials higher contrast can possibly be achieved by phase contrast imaging. Furthermore, the phase shift is influenced less severely by changes in the X-ray energy than the attenuation, which makes phase contrast measurements less prone to beam hardening effects [13,14].

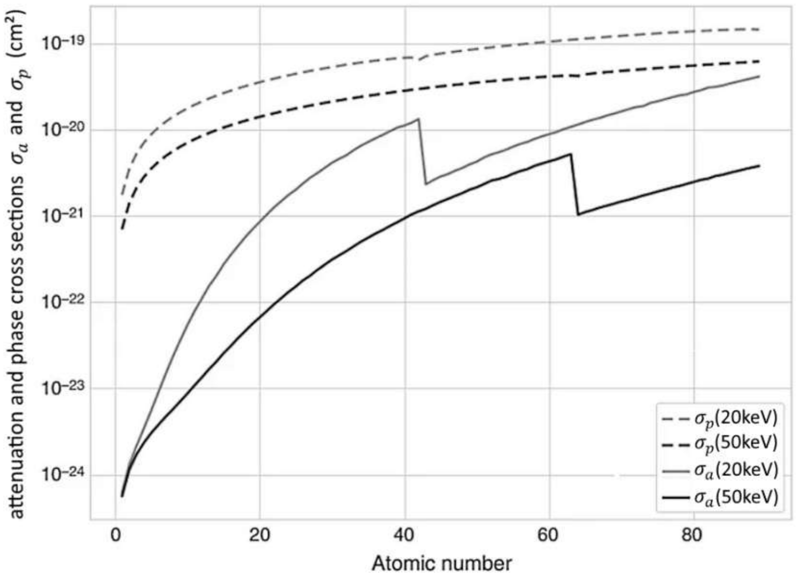

Fig. 15: Phase cross section σ_p and attenuation cross section σ_a at 20 keV and 50 keV X-ray energies respectively over atomic number of a penetrated test specimen. Steps in σ_a correspond to absorption edges of materials at specific atomic numbers. (Image reprinted from [78] with permission from Springer Nature)

With these features, several publications have proven phase contrast imaging to be a promising modality for medical imaging, for example, for the reduction of artifacts caused by metal implants [14,83], or contrast enhancement for the imaging of soft tissue [84,85]. Furthermore, various industrial applications for the characterization of weakly absorbing materials, such as polymers [86] and fiber-reinforced specimens [48,87], have been presented as well.

3.1.2 Dark-field imaging

Dark-field imaging relies on the effect of X-ray small and ultra-small angle scattering (SAS, USAS), caused by microstructures or differences in the electron density within an inhomogeneous specimen [88]. Typically, these features are too small to be resolved by common X-ray detectors directly. However, the blurring of an X-ray beam associated with the (U)SAS, as schematically visualized in Fig. 16, can be quantified by application of different specific measurement setups. Consequently, a dark-field image can reveal otherwise hidden additional information about (sub-) micron structures within a specimen, offering huge potential in both medical/biological [89–91] and industrial [15,92] applications.

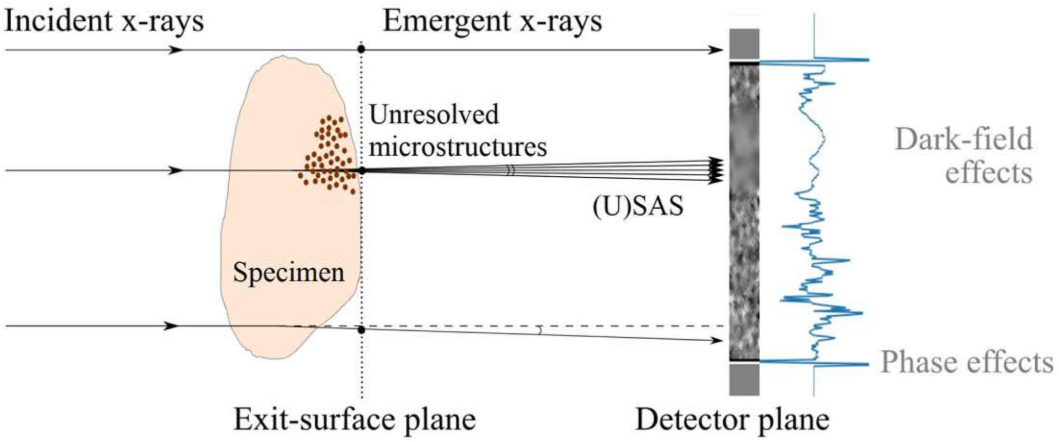

Fig. 16: Schematic example of (U)SAS effects caused by unresolvable microstructures within an otherwise homogeneous specimen leading to a blurring of high frequency components in the intensity line profile. However, special setups/methods are needed for extraction of the dark-field signal. (Image modified and reused from [93] under CC BY 4.0)

The name of the dark-field modality was chosen as an analogy to earlier methods from light and scanning electron microscopy, in which scattering structures are similarly depicted as brighter regions on otherwise dark background [94]. The idea of dark-field imaging was initially sparked by Johnston et al. [95] and Chapman et al. [96] and their experiments with monochromatic synchrotron radiation in combination with crystal analyzers. These experiments finally led to the extraction of the first dark-field images by analyzer-based imaging (ABI) after researchers observed a broadening of the rocking curve caused by (U)SAS [79,97]. However, the need for rather high temporal coherence of the X-ray beam, typically found only at synchrotron facilities, was limiting the applicability and therefore the potential of this early method for practical use. It was not until 2007 when Pfeiffer et al. introduced a grating interferometric method to extract both phase contrast [98] and dark-field contrast [99] using hard X-ray spectra in typical laboratory setups, that the DFC modality gained wider attention within the scientific community.

Similar to the linear attenuation coefficient, the small-angle scattering can be described by the linear diffusion coefficient ϵ, which is a function of the chemical as well as structural properties of the material and the energy of the X-ray beam scattered [100,101]. Also similarly, given the assumption of ideal random scattering and monochromatic X-ray energy, the dark-field signal D can be expressed as

$$D = e^{-\epsilon t} \tag{3.7}$$

measured after a homogeneous specimen of thickness t. Since the measurement of the DFC modality greatly depends on system specific parameters of the respective measurement method, further explanations will be given in a following chapter (3.3) dedicated to TLGI.

3.2 Different phase contrast and dark-field methods

Although the X-ray phase contrast and dark-field modalities can provide additional information for materials characterization, their extraction is not as straight forward as standard attenuation-based imaging. This chapter will cover a brief overview of methods for the extraction of phase and dark-field images, as a detailed introduction to all methods existing is beyond the scope of this work. Since the first introduction of X-ray PCI by Bonse & Hart in 1965 [102], various methods with different limitations and advantages have been developed. The interferometry-based phase contrast imaging using a single crystal as by Bonse & Hart was followed by analyzer-based methods first developed by Goetz et al. in 1979 [103,104]. Thereby, a rocking analyzer crystal placed after the specimen is used to convert effects of X-ray refraction into intensity signals on the detector in dependence of its rocking angle. Consequently, the first derivative of the phase shift caused by the specimen in the beam path can be extracted [78] (see Fig. 17).

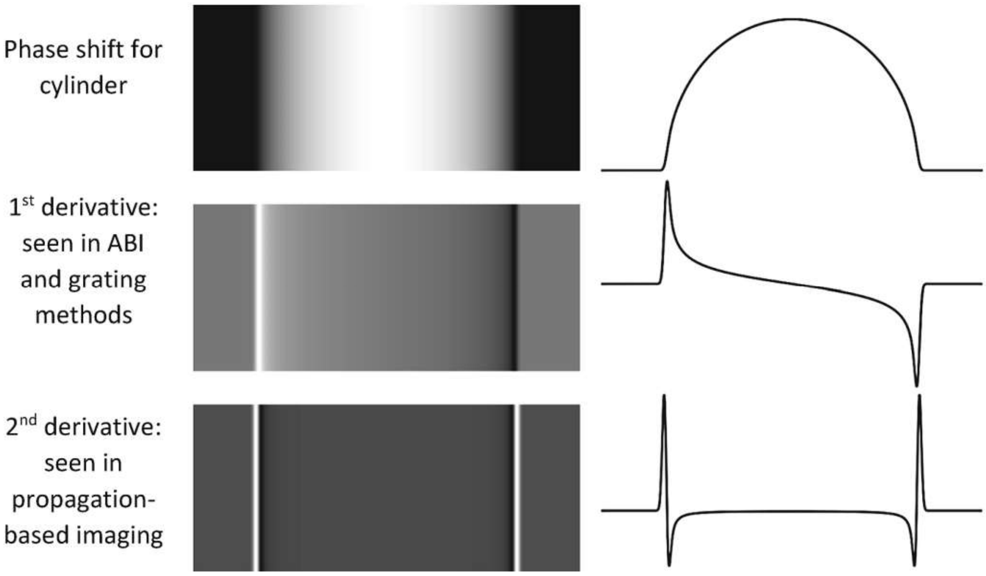

Fig. 17: Phase shift profile of a cylindrical specimen (top) with its first derivative (middle) as captured by analyzer-based imaging (ABI) and grating-interferometry methods, and its second derivative (bottom) as captured by PB-PCI. The corresponding line profiles are shown to the right. (Image reprinted from [78] with permission from Springer Nature)

One of the simplest PCI methods is propagation-based phase contrast (PB-PCI) as it only requires sufficiently spatially coherent X-rays, for example, produced by a micro-focus X-ray tube, and a propagation distance after the specimen long enough for interference patterns to form. Consequently, the second derivative of the phase shift can be measured by a standard X-ray detector (see Fig. 17). However, the measured image will contain attenuation as well as phase information which is why several phase retrieval algorithms have been developed, among which the method introduced by Paganin et al. [105] is probably the most commonly known [78]. Furthermore, the extraction of dark-field images is not possible using this method.

In the last decades many more methods have been developed, for example, using coded apertures [106] or even random absorption masks [107] (also referred to as speckle-based imaging [108]) to create a structured illumination of a specimen and subsequently track the changes in the pattern projected on a detector to extract information on attenuation and refraction of a specimen. Among them, the edge illumination method introduced by Olivo et al. is probably worth mentioning separately, as it supposedly has the most relaxed requirements in spatial and temporal coherence of the X-ray beam [109]. Moreover, many but not all the methods mentioned provide the possibility to extract dark-field contrast as well, as exemplarily demonstrated for speckle-based imaging [110], edge illumination [111], and analyzer-based imaging [112]. However, the extraction of dark-field contrast mostly requires the recording of images at additional aperture positions or rocking crystal angles respectively.

Another method which makes use of gratings but, different from the aperture-based methods mentioned, works by use of interferometric effects, is Talbot-Lau grating interferometry-based imaging (TLGI). Thereby, the intensity modulations projected onto a detector caused by a set of gratings in Talbot-Lau formation are analyzed to extract attenuation, phase, and dark-field information. As this work aims to develop and investigate industrial applications of TLGI for the inspection of lightweight materials, this method will be explained in more detail in a separate chapter.

3.3 Talbot-Lau grating interferometry

The first method based on a Talbot interferometer was demonstrated by Momose et al. [113] in 2003 and is based on the observations made by H.F. Talbot [114] in 1836 that coherent light passing through an absorbing grating creates a self-image of said grating at repeated distances. These are referred to as Talbot distances d_T and are based on the period of the grating p_1 and the wavelength of the incident radiation via [115]

$$d_T = \frac{2{p_1}^2}{\lambda} \quad . \tag{3.8}$$

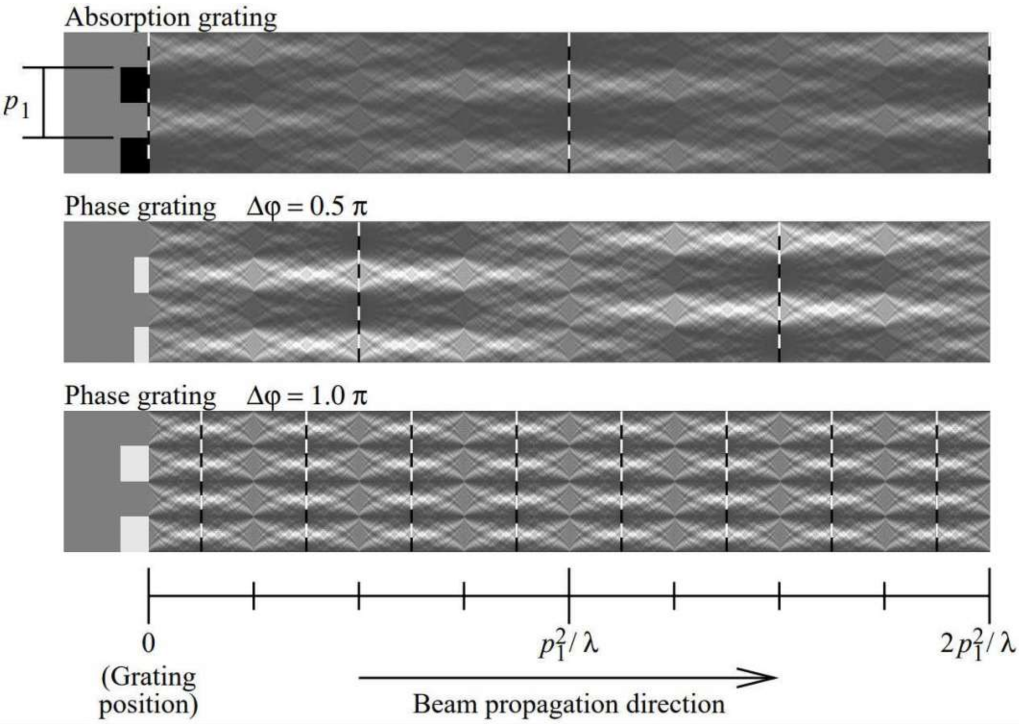

Fig. 18: Interference patterns (Talbot carpet) from a coherent plane wave generated after an absorption grating (top) a 0.5 π shifting (middle) and a 1.0 π shifting phase grating (bottom) respectively. The pattern is shown for a propagation length of one Talbot distance d_T. Positions at which highest contrast of the self-images of the gratings are present are indicated with vertical black and white dashed lines. (Reprinted with adaptations from [116] with permission from SPIE Digital Library)

By replacing the absorbing structures of the grating with a material that induces a phase shift to the incoming radiation, self-images of this now so-called phase grating are observable at fractions of the Talbot distance as well. Thereby, maximum visibility of the self-image is achieved when the phase grating causes a phase shift in X-rays passing through the grating bars by either π or $\pi/2$ [116]. Consequently, an interference pattern also referred to as "Talbot carpet" is formed after the grating as illustrated in Fig. 18. When a phase grating is used, Eq. (3.8) has to be adapted to calculate the fractional Talbot distance by

$$d_{T,n} = \frac{1}{\eta^2}\frac{n{p_1}^2}{2\lambda} \tag{3.9}$$

where n is an integer number referring to the Talbot order of the interferometer and η is a factor accounting for the change in the fractional Talbot distance depending on the phase shift induced by the phase grating via

$$\eta = 1 \text{ for a shift of } \pi/2 \text{ or} \tag{3.10}$$

$$\eta = 2 \text{ for a shift of } \pi \text{ [116].} \tag{3.11}$$

Furthermore, the period of the self-image p_2 changes with respect to

$$p_2 = p_1 \text{ for a phase shift of } \pi/2 \text{ and} \tag{3.12}$$

$$p_2 = p_1/2 \text{ for a phase shift of } \pi \text{ [116].} \tag{3.13}$$

However, the Talbot effect can only be exploited using coherent X-ray radiation which is why Pfeiffer et al. [117] introduced another grating into the setup placed directly in front of an incoherent X-ray source and thereby formed a Talbot-Lau interferometer as schematically depicted in Fig. 19. This source grating G0 thereby creates an array of line sources that are mutually incoherent but individually thin enough for sufficient spatial coherency [118]. To meet the requirements in coherence length ξ_s for the Talbot effect to appear the setup must satisfy

$$\xi_s = \frac{\lambda l_0}{\gamma_0 p_0} \geq p_1 \tag{3.14}$$

with the ratio γ_0 between the period p_0 and the width of the apertures of the source grating, and the distance l_0 between the source grating and phase grating G1 [117]. Furthermore, for the application with an approximately spherical wave front as from laboratory X-ray sources the Talbot distance changes to [119]

$$d_T^{sphere} = \frac{l_0 \cdot d_T^{plane}}{l_0 - d_T^{plane}} \quad . \tag{3.15}$$

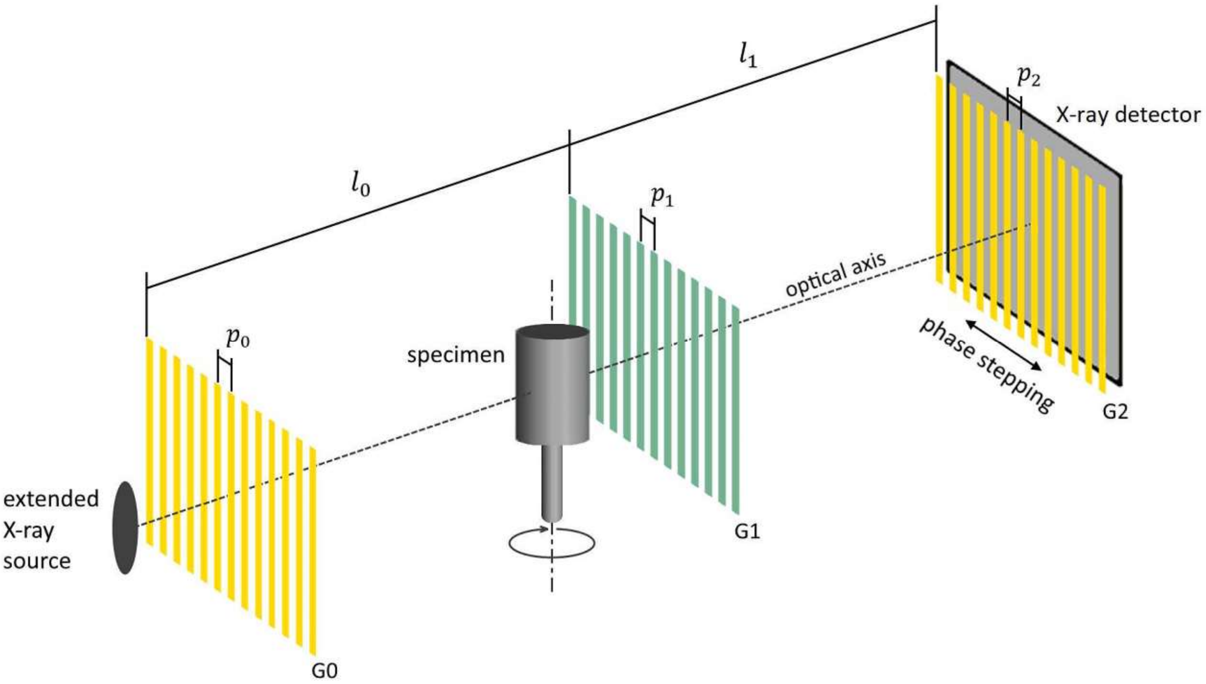

Fig. 19: Schematic of a Talbot-Lau interferometer with source grating G0, phase grating G1, and analyzer grating G2 at respective grating periods p_0, p_1, and p_2. Note that a specimen can be placed before or after the phase grating. The direction of the phase stepping is indicated as well. Note that phase stepping basically can be performed by any one of the three gratings.

Under these conditions, each aperture within the source grating will create an interference pattern at the (fractional) Talbot distances after the phase grating. However, the condition

$$p_0 = p_2 \frac{l_0}{l_1} \tag{3.16}$$

with the distance l_1 between phase and analyzer grating must be met in order to shift the patterns by exactly one period of the analyzer grating G2 and therefore to add up constructively [117]. This analyzer grating completes the Talbot-Lau interferometer setup and is needed for the extraction of the attenuation, phase, and dark-field contrast, since the period of the interference pattern created by the phase grating typically is much too small to be resolved by common X-ray detectors directly. Consequently, this grating is placed directly before the X-ray detector with a grating period matching that of the created interference pattern.

3.3.1 Imaging with a Talbot-Lau grating interferometer

To record a projection image from which phase and dark-field information can be extracted, a stepwise displacement of one of the gratings over one period in direction perpendicular to its grating bars must be performed. During this displacement, the intensity in each detector pixel is monitored creating a sinusoidal intensity modulation as visualized in Fig. 20. This procedure is also referred to as phase stepping [120].

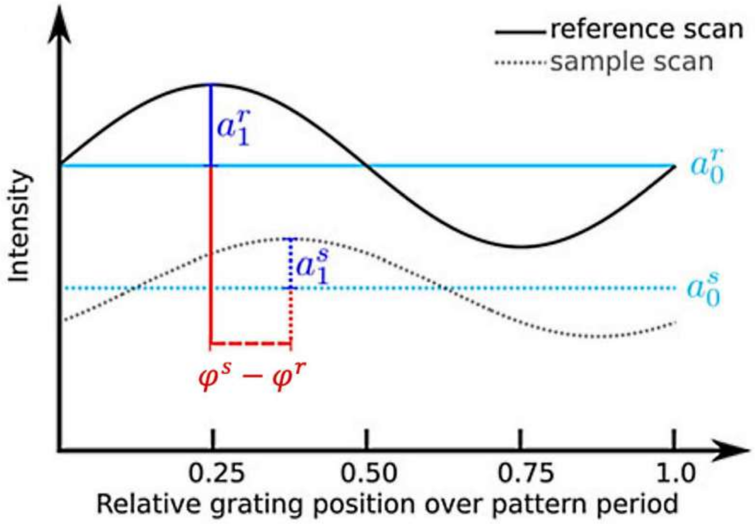

Fig. 20: Intensity modulation measured within a single detector pixel with respect to the lateral grating position. Mean values a_0, amplitudes a_1, and phase shift $\varphi = \varphi^s - \varphi^r$ between sample and reference curve are indicated. (Image modified and reused from [121] under CC BY-NC-ND 4.0)

By comparing the intensity modulation to a reference recording without a specimen in the beam path three complementary modalities can be extracted. The attenuation contrast (AC) corresponds to the change in mean intensity a_0 of the sinusoidal curve. The phase contrast is represented by the lateral shift in phase φ between the two curves and extracted by calculation of the difference between the two, as indicated in Fig. 20. Since this phase shift in the interference pattern is a direct measure of the first derivative of the phase shift in the wave front, the phase contrast measured in TLGI is typically referred to as differential phase contrast (DPC) [117]. However, note that a phase shift exceeding one period of the analyzer grating cannot be detected correctly and leads to a phenomenon referred to as phase wrapping [122]. Finally, the dark-field contrast (DFC) is represented by the change in amplitude a_1 of the intensity signal. For that matters the visibility V is introduced which is defined as the normalized oscillation amplitude of the intensity curve [99]:

$$V = \frac{a_1}{a_0} \qquad . \tag{3.17}$$

The reduction in visibility caused by an X-ray scattering specimen in the beam path normalized to the visibility within a reference image is referred to as the dark-field signal D [99]:

$$D = \frac{V^s}{V^r} \tag{3.18}$$

The superscripts s and r thereby indicate the measurement with specimen in the beam path and the reference measurement without specimen in the beam path, respectively. The dark-field signal is inversely proportional to the integrated (U)SAS power caused by sub-micron structures within the specimen. Consequently, in a homogeneous specimen with negligibly small (U)SAS contribution the dark-field signal $D = 1$, while strongly scattering specimens will cause a reduction in the dark-field signal of $D < 1$ [18].

Considering the actual lateral shift s of the projected self-image which is represented by the phase shift φ within the intensity curves via

$$s = \frac{p_2}{2\pi}\varphi \tag{3.19}$$

the refraction angle α can be calculated under the small-angle approximation and thereby is directly related to the phase shift in the interference pattern via [123]

$$\alpha = \frac{p_2}{2\pi l_1}\varphi \quad . \tag{3.20}$$

By combining Eq. (3.20) with Eq. (3.6) the differential phase shift $\Delta\Phi/\Delta x$ in the wave front after the object can be related to the phase shift φ in the interference pattern via

$$\frac{\Delta\Phi}{\Delta x} = \frac{p_2}{\lambda l_1}\varphi \qquad [13]. \tag{3.21}$$

However, this formula strictly is valid only for flat objects in a parallel beam setup, and also only for a discrete monochromatic X-ray energy. Practically, the phase shift φ in the interference pattern is measured with a Talbot-Lau grating interferometer in a polychromatic spectrum and therefore is a direct measure of the effective differential phase shift in the wavefront [13,117]. Consequently, the effective phase shift in the wavefront can be extracted by simple one-dimensional linear integration of the recorded image data of φ in direction perpendicular to the gratings [13]. However, image noise might cause severe artifacts which is why typically additional filters are applied [124]. In case that a full computed tomography (CT) scan was recorded, the phase shift data subsequently can be reconstructed via a standard filtered back projection algorithm, likewise to the AC and DFC data [98].

Furthermore, by incorporation of TLGI setup specific parameters the refractive index decrement can be evaluated from the phase shift via [12]

$$\delta = \varphi \frac{p_2}{2\pi l_1}\frac{l_s}{r} \tag{3.22}$$

where p_2 is the period of the analyzer grating and l_1 the distance between phase and analyzer grating. The multiplication by l_s/r is necessary to correct for the reduction in sensitivity occurring in cone beam setups, where l_s is the distance from the X-ray source to the phase grating and r the distance from the X-ray source to the specimen [82]. Following this, the electron density of a measured sample can be derived directly from the recorded phase contrast data by use of Eq. (3.5).

The blurring width σ_s of the interference pattern at the plane of the analyzer grating and the angular standard deviation σ_α within the scatter angle after the specimen can be calculated analogous to Eq. (3.19) and (3.20) by substituting the phase shift φ with the standard deviation of the phase shift σ_φ [97]. The angular standard deviation σ_α is a property unaffected by the measurement setup and therefore a measure for specimen related scattering properties. It is related to the linear diffusion coefficient by [97]

$$\epsilon = \frac{\sigma_\alpha^2}{\Delta t} \tag{3.23}$$

which is normalized to the specimen thickness Δt. Consequently, σ_α describes the specific scattering width per unit length [125] and is directly related to the dark-field signal via Eq. (3.7). However, this definition is strictly true only for isotropic scattering specimens in a parallel beam setup [97].

The AC and DFC are by convention expressed as the negative natural logarithm of the transmission $T = a_0^s/a_0^r$ and the dark-field signal D. Consequently, the three modalities are ultimately written as:

$$AC = -\ln\left(\frac{a_0^s}{a_0^r}\right), \qquad DFC = -\ln\left(\frac{V^s}{V^r}\right), \qquad DPC = \varphi^s - \varphi^r \,. \tag{3.24}$$

As introduced and demonstrated by Wang et al. [126], the dependency of the DFC on the specimen thickness furthermore can be compensated by taking the ratio between the DFC and AC signal. The so generated normalized image is referred to as R image or the normalized dark-field contrast (nDFC):

$$nDFC = \frac{DFC}{AC} \quad . \tag{3.25}$$

Since both the AC and DFC scale linearly with a homogeneous specimen's thickness (at monochromatic radiation) the signal thereby becomes decoupled from the thickness. Therefore, the nDFC measured behind two samples of identical material is expected to be the same regardless of differences in thickness, which makes the nDFC a potential modality for material discrimination [126]. The experimental example conducted by Wang et al. [126] is shown in Fig. 21, demonstrating the relatively constant nDFC regardless of changes in specimen thickness. However, noise in nDFC becomes dominant at low specimen thickness, particularly for weakly scattering materials. This is visible at the example of Nylon and Delrin in Fig. 21.

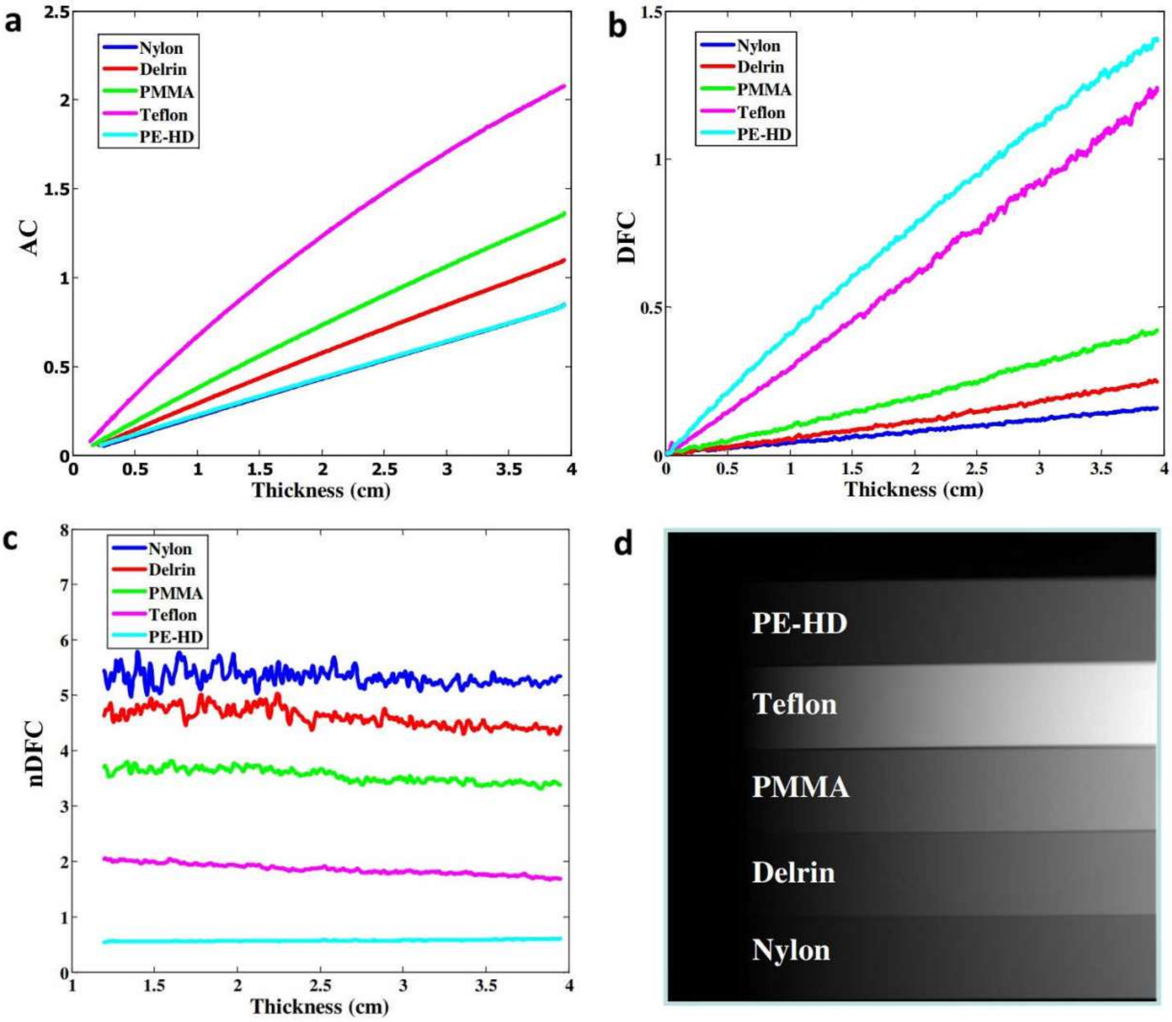

Fig. 21: Experimental results of wedges of high-density polyethylene (PE-HD), Teflon, Polymethyl methacrylate (PMMA), Delrin, and Nylon. The AC, DFC, and nDFC are plotted as a function of the material thickness in **(a)**, **(b)**, and **(c)** respectively. The AC projection image of the specimens with thickness increasing from left to right is shown in **(d)**. Note that noise in nDFC can become dominant at low specimen thickness and weakly scattering materials. (Image reprinted from [126]. © Institute of Physics and Engineering in Medicine. Reproduced by permission of IOP Publishing Ltd. All rights reserved)

3.3.2 Visibility and angular sensitivity

The maximum achievable visibility within the reference scan is also an indicator for the quality of a TLGI system as a higher visibility will ultimately allow for the detection of smaller changes in the refraction angle α. The smallest detectable refraction angle α_{min} therefore is a measure for the angular sensitivity of a system and highly dependent on the standard deviation σ_φ (or blurring width [97]) within the measured φ via [123]

$$\alpha_{min} = \frac{p_2}{2\pi l_1} \sigma_\varphi \quad . \tag{3.26}$$

Strictly speaking, this equation is valid only for flat specimens positioned directly in the plane of the phase grating. Practically, an additional factor considering the actual positioning of the specimen between G0 and G1 has to be added according to

$$\alpha_{min} = \frac{p_2}{2\pi d} \frac{l_0 + l_s}{r + l_s} \sigma_\varphi \tag{3.27}$$

with l_s being the distance from the X-ray source to G0 [123]. As evident from Eq. (3.26) also setup specific parameters effect the absolute sensitivity of a measurement or TLGI system respectively, whereas from Eq. (3.27) it becomes obvious that a positioning of the specimen as close as possible to the phase grating will yield the highest angular sensitivity. As demonstrated by Donath et al. [127] the sensitivity decreases linearly with distance of the specimen to the phase grating, reaching zero in the plane of the source or the analyzer grating, respectively.

A major factor in achieving a high fringe visibility and therefore also high sensitivity is the choice of the X-ray spectrum with regards to the design energy E_0 of a TLGI system. The visibility decreases the more the applied X-ray energy deviates from the design energy as the (fractional) Talbot distance is directly influenced by the X-ray wavelength as by Eq. 3.8. Furthermore, the efficiency of the phase grating to apply the desired phase shift of π or $\pi/2$ will also be diminished for X-ray energies deviating from E_0[120]. Both of these effects cause a blurring of the interference pattern in the plane of the analyzer grating, leading to a reduction of the visibility. Ludwig et al. [88], for example, simulated the visibility of a given TLGI system with a design energy of 45 keV to demonstrate the dependency of the visibility with respect to the X-ray energy as shown in Fig. 22. Consequently, maximum visibility of 37% could be achieved with a spectrum of 60 kV peak voltage (kVp), while at the 120 kVp spectrum visibility was reduced to only 16%. Although TLGI systems are commonly described by their design energy, it is obvious from Fig. 22 that the visibility is a somewhat periodically rising function. However, many other factors are limiting the effectively achievable sensitivity such as vibrations within the setup or temperature fluctuations during measurements [123]. The optimization of TLGI setups for high sensitivity is already extensively covered, for example, in works by Thuering et al. [128].

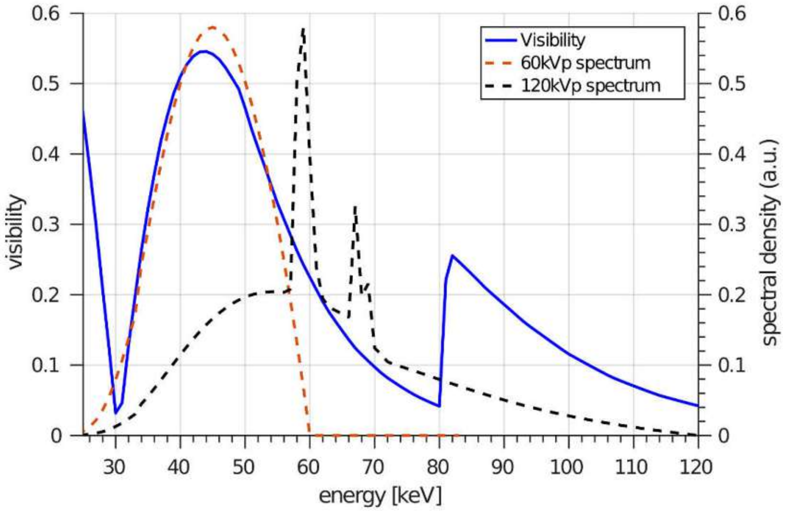

Fig. 22: Visibility as a function of photon energy simulated for a given TLGI setup of 45 keV design energy. Two typical X-ray spectra at 60 kVp and 120 kVp are plotted alongside. (Image modified and reused from [88] under CC BY 4.0)

3.3.3 Structure size selectivity of DFC

Unlike to the linear diffusion interpretation of the dark-field signal as applied in previous chapters, Yashiro et al. [129] presented a model taking into account variations in refractive effects caused by differently sized microstructures as well as setup specific parameters. They thereby consider the phase shift Φ within a wavefront as the sum of unresolvable high frequency Φ_f and resolvable low frequency Φ_s components. When Φ_f is assumed as a random Gaussian distribution at a width of σ_f, the dark-field signal can be expressed as [129]

$$D = e^{-\sigma_f{}^2(1-\gamma(\xi))} \tag{3.28}$$

with the autocorrelation function γ, which is a function of the autocorrelation length

$$\begin{aligned} \xi &= \frac{d_{S,G2}}{p_2} \cdot \lambda && \text{for specimens placed between G1 and G2, and} \\ \xi &= \frac{d_{G0,S}}{p_0} \cdot \lambda && \text{for specimens placed between G0 and G1 [101].} \end{aligned} \tag{3.29}$$

Therein, the positioning of the specimen is represented by the distance $d_{S,G2}$ between specimen and G2, and the distance $d_{G0,S}$ between the specimen and G0, while setup specific parameters are represented by the periods p_0 and p_2 of G0 and G2 respectively. Thus, by combining Eq. (3.29) with Eq. (3.28), the dark-field signal at a given X-ray energy is expressed as a function of material and setup related parameters.

As previous related works have demonstrated [119,130,131], the dark-field sensitivity reaches its maximum when specific relations between the size of microstructures within a specimen and the autocorrelation length are met [132]. Since for a given TLGI setup and photon energy the autocorrelation length varies only with the positioning of the specimen, it can easily be tuned in order to achieve maximum sensitivity for microstructures of desired size. Lynch et al. [131], for example, investigated this phenomenon experimentally by measuring microsphere suspensions of different sphere diameter at varying autocorrelation lengths by changing the specimen position with respect to the gratings. As visible in Fig. 23, the experiment provided evidence that the dark-field signal is strongest when particles with a radius approximately equal to the autocorrelation length are measured.

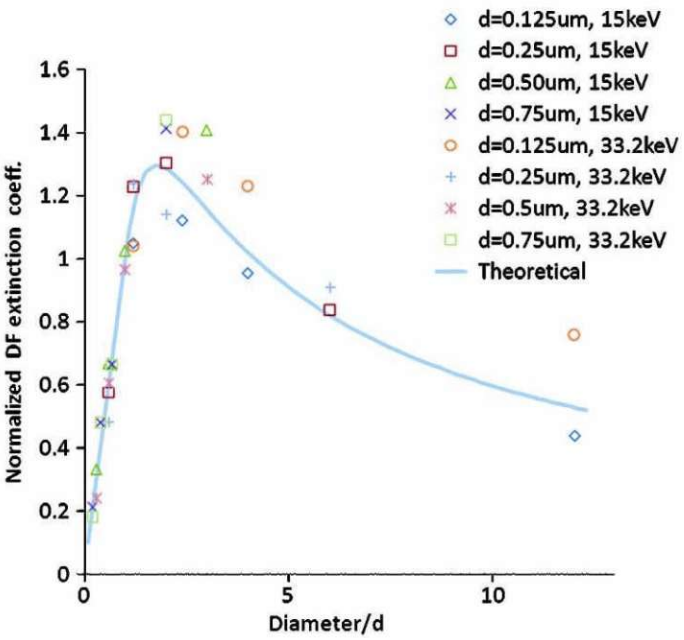

Fig. 23: The normalized dark-field extinction coefficient as a function of the ratio between the microsphere diameter and the autocorrelation length (in this figure denoted as d). Experimental values recorded at 15 and 33.2 keV photon energy are displayed alongside theoretical values. Obviously, the dark-field signal reaches its maximum at a ratio of approximately $Diameter/d = 2$. (Reprinted with permission from [131] © The Optical Society.)

Consequently, this effect can be exploited for the discrimination of materials with equal attenuation but different structural properties. However, for particles of size below 1.8 times the autocorrelation length the dark-field signal in this experiment decreases, which is unexpected as smaller structures should cause larger scattering angles and consequently stronger dark-field signal. This trend most likely can be explained by the effect that the total amount of scattered X-rays at some point rapidly decreases with structure size which effectively counteracts the otherwise larger scattering angle [131].

3.3.4 Directional DFC

The approach of directional dark-field imaging was first introduced by Jensen et al. [18], wo theoretically and experimentally demonstrated the relationship of the dark-field signal to the orientation of the grating bars relative to scattering structures within a specimen. Since a Talbot-Lau interferometer is typically formed by line gratings, such a system is sensitive only to scattering and phase effects in direction perpendicular to the grating bars, while scattering and phase shifts in direction parallel to the gratings remain undetected.

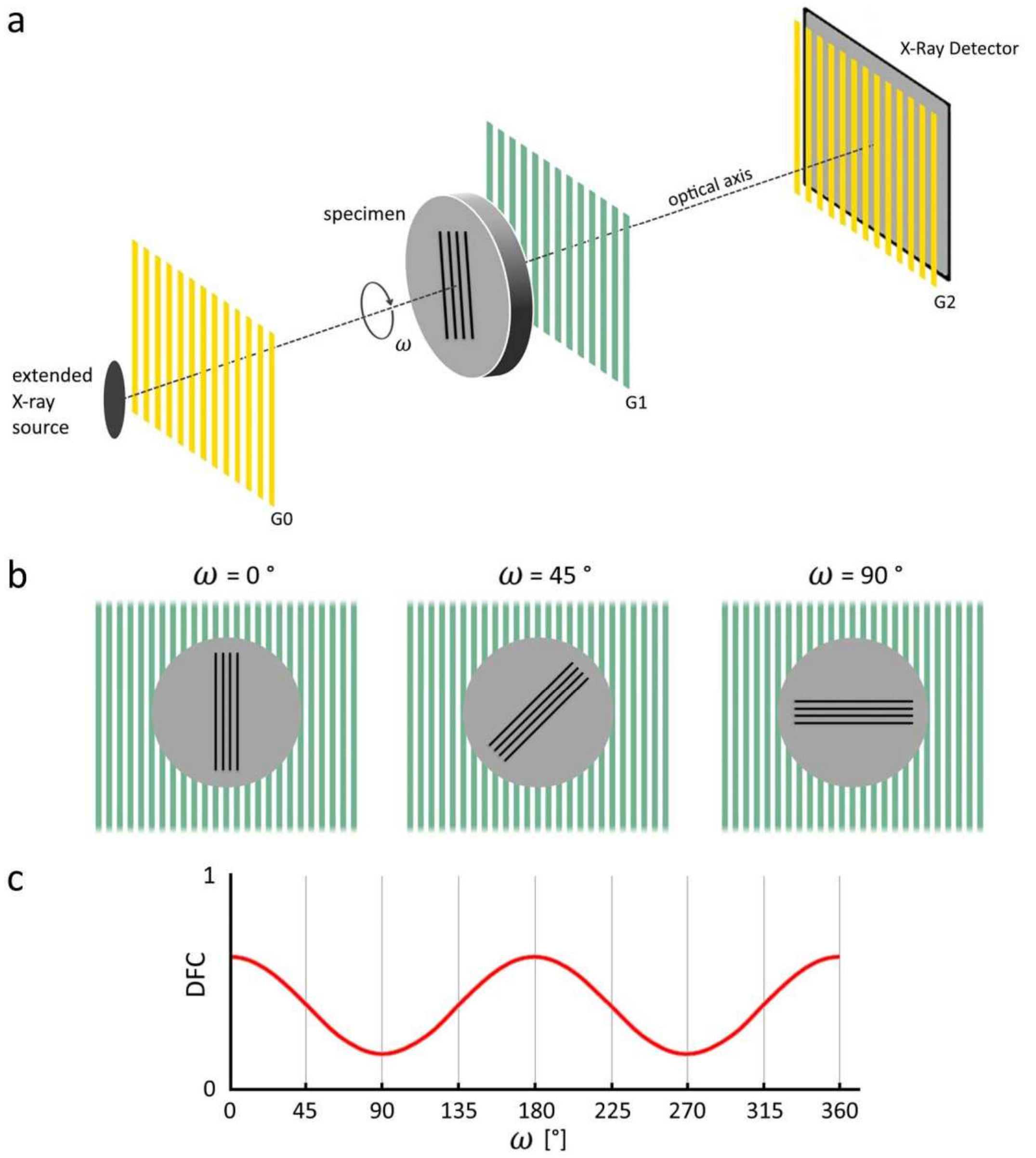

Fig. 24: Directional dark-field imaging in the plane parallel to the gratings also known as vector radiography. The schematic setup with a specimen containing fiber structures rotating around the optical axis is shown in **(a)**. In **(b)** different rotation angles ω before the phase grating are shown with the respective DFC measured in **(c)**. Maximum DFC is measured when microstructures (fibers) are aligned parallel to the grating bars and minimum DFC when they are aligned perpendicular. (Figure inspired by [18])

Consequently, depending on the orientation of microstructures within a specimen, the detected scattering intensity changes. As schematically illustrated in Fig. 24, it has been shown that microstructures like natural or synthetic fibers within a plane parallel to the gratings evoke the strongest scatter signal when aligned parallel to the grating bars and the weakest when oriented perpendicular to them [133]. This effect can be exploited in order to extract information about the orientation of scattering microstructures within a specimen. To do so, a specimen is placed in the beam path and several DFC images at different rotation angles ω around the optical axis are recorded as explained previously. After the alignment of these images to the $\omega = 0$ orientation, the data set recorded for each pixel will show a periodic DFC intensity curve as a function of the rotation angle ω that can be expressed by [133]

$$DFC(\omega) = a_0 + a_1 \cos(2(\omega + \phi)) \quad . \tag{3.30}$$

This function can be solved similarly to the intensity modulation acquired by the phase stepping procedure as introduced in Chapter 3.3.1. For directional dark-field imaging a_0 represents the average scattering strength within a pixel, a_1 describes the change in scattering with respect to ω, and the main orientation of scattering structures ϕ relative to the orientation of the grating bars [88,133]. In other words, the average scattering strength a_0 can also be considered as the isotropic part of the scattering, which is independent of the orientation of a specimen or structure while a_1 is the anisotropic part, changing with the orientation [134]. The ratio between a_1 and a_0 is a measure for the degree of anisotropy A within the specimen and ranges from 1 for perfectly aligned structures to 0 for a random distribution [135].

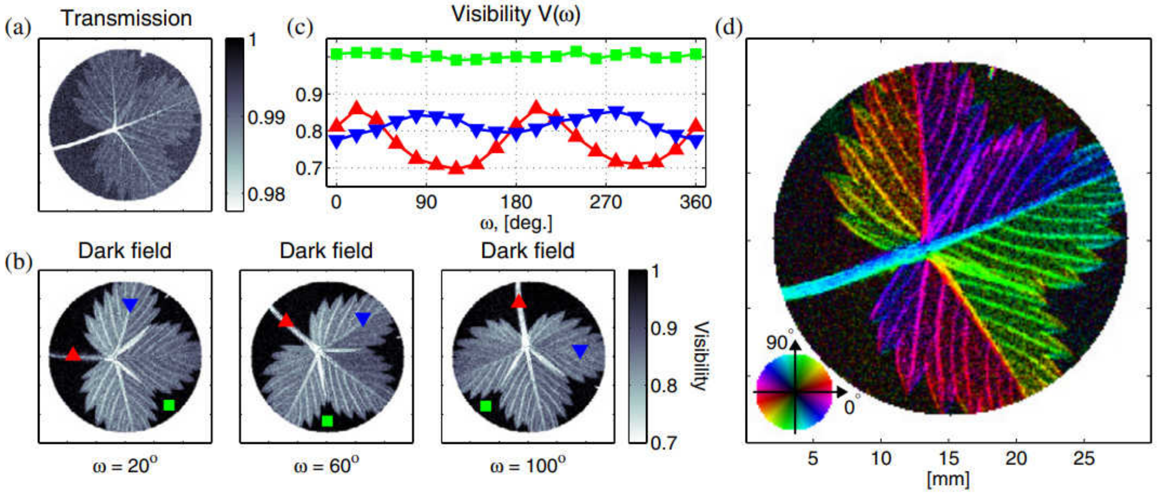

Fig. 25: Directional analysis of a strawberry leaf. An X-ray transmission image is shown in **(a)** alongside the dark-field images of the specimen at three different rotation angles ω in **(b)**. It becomes obvious that the dark-field signal changes with respect to the structural orientation within the specimen. The visibility within the red, blue, and green regions indicated in **(b)** are displayer as a function of ω in **(c)**. The main orientation angle of

microstructures within the specimen is mapped according to the color wheel in **(d)**, with the image brightness representing the degree of orientation. [18] (Image reprinted from [18]. © Institute of Physics and Engineering in Medicine. Reproduced by permission of IOP Publishing Ltd. All rights reserved)

An example for the orientational analysis of a strawberry leaf is given in Fig. 25, illustrating the change in visibility with respect to the rotation angle ω as well as color-coded results of the structural orientation evaluated in 2D. This method of orientational analysis within a plain parallel to the gratings is sometimes also referred to as X-ray vector radiography [133,135].

However, the scattering strength detected via dark-field imaging is also affected by the orientation of microstructures in the three-dimensional space. As experimentally demonstrated by Bayer et al. [136] and exemplarily shown in Fig. 26, the closer a structure comes to an orientation parallel to the optical axis ($\theta = 90°$ and $\phi = 0°$ or $180°$), the stronger the scattering signal detected. Consequently, if a computed tomography scan is performed, the anisotropic part of the scattering causes a change in the DFC. This change is not accounted for in a standard FBP reconstruction, which assumes a constant scatter signal for a given volume element independent of its orientation in space [19]. This fact can lead to imaging artifacts especially for specimens containing strongly ordered microstructures such as fiber-reinforced polymers. However, the peak in the scattering signal caused by structures aligned with the beam path also allows for the extraction of orientational information, for example, within CFRPs [20].

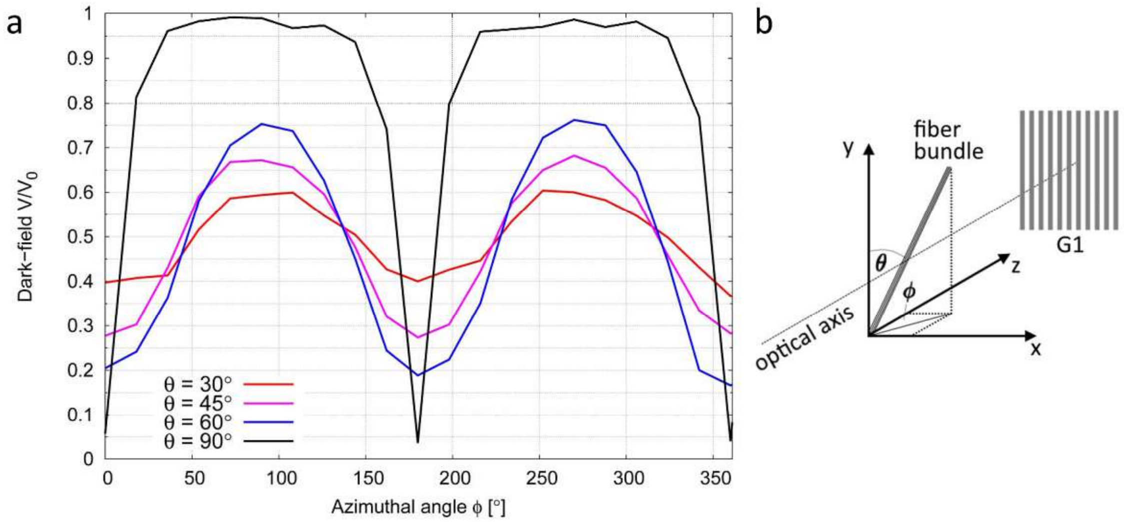

Fig. 26: **(a)** Dark-field visibility caused by a carbon fiber bundle in the beam path as a function of its azimuthal angle ϕ (= CT rotation angle) at four different tilt angles θ. It becomes obvious that the visibility is lowest, and therefore the scattering is highest, when the fibers are aligned with the optical axis. The coordinate system including CT rotation angle ϕ around the y-axis and tilt angle θ around the x-axis are shown in **(b)** [136]. The orientation of the phase grating G1 is shown for reference. (Figure part **(a)** reprinted from [136] with permission from Optica Publishing Group)

4 Bibliography

[1] Campbell FC. Structural Composite Materials. ASM International; 2010. https://doi.org/10.31399/asm.tb.scm.9781627083140.

[2] Fitzer E, Manocha LM. Carbon Reinforcements and Carbon/Carbon Composites. Springer Berlin, Heidelberg; 1998. https://doi.org/10.1007/978-3-642-58745-0.

[3] Che D, Saxena I, Han P, Guo P, Ehmann KF. Machining of carbon fiber reinforced plastics/polymers: A literature review. Journal of Manufacturing Science and Engineering, Transactions of the ASME 2014;136. https://doi.org/10.1115/1.4026526.

[4] Guo Y, Xu Y, Wang Q, Dong Q, Yi X, Jia Y. Enhanced lightning strike protection of carbon fiber composites using expanded foils with anisotropic electrical conductivity. Compos Part A Appl Sci Manuf 2019;117:211–8. https://doi.org/10.1016/j.compositesa.2018.11.022.

[5] Zhang L, Wang X, Pei J, Zhou Y. Review of automated fibre placement and its prospects for advanced composites. J Mater Sci 2020;55:7121–55. https://doi.org/10.1007/s10853-019-04090-7.

[6] Kesarwani S. Polymer Composites in Aviation Sector A Brief Review Article. International Journal of Engineering Research & Technology 2017;6. https://doi.org/10.17577/IJERTV6IS060291.

[7] Fernlund G, Wells J, Fahrang L, Kay J, Poursartip A. Causes and remedies for porosity in composite manufacturing. IOP Conf Ser Mater Sci Eng, vol. 139, Institute of Physics Publishing; 2016. https://doi.org/10.1088/1757-899X/139/1/012002.

[8] Greenhalgh ES. Defects and damage and their role in the failure of polymer composites. Woodhead Publishing Series in Composites Science and Engineering, Failure Analysis and Fractography of Polymer Composites, Woodhead Publishing; 2009, p. 356–440. https://doi.org/10.1533/9781845696818.356.

[9] Towsyfyan H, Biguri A, Boardman R, Blumensath T. Successes and challenges in non-destructive testing of aircraft composite structures. Chinese Journal of Aeronautics 2020;33:771–91. https://doi.org/10.1016/j.cja.2019.09.017.

[10] Glinz J, Pace F, Maurer J, Holzleitner M, Eckl M, Vopálenský M, et al. Influence of continuous fiber reinforcement on tensile properties in fused filament fabricated specimens. AIAA Science and Technology Forum and Exposition, AIAA SciTech Forum 2023 2023. https://doi.org/10.2514/6.2023-2199.

[11] Birnbacher L, Braig EM, Pfeiffer D, Pfeiffer F, Herzen J. Quantitative X-ray phase contrast computed tomography with grating interferometry: Biomedical applications of quantitative X-ray grating-based phase contrast computed tomography. Eur J Nucl Med Mol Imaging 2021;48:4171–88. https://doi.org/10.1007/s00259-021-05259-6.

[12] Willner M, Herzen J, Grandl S, Auweter S, Mayr D, Hipp A, et al. Quantitative breast tissue characterization using grating-based x-ray phase-contrast imaging. Phys Med Biol 2014;59:1557–71. https://doi.org/10.1088/0031-9155/59/7/1557.

[13] Chabior M, Donath T, David C, Bunk O, Schuster M, Schroer C, et al. Beam hardening effects in grating-based x-ray phase-contrast imaging. Med Phys 2011;38:1189–95. https://doi.org/10.1118/1.3553408.

[14] Glinz J, Zabler S, Kastner J, Senck S. Metal Artifacts in Attenuation and Phase Contrast X-Ray Microcomputed Tomography: A Comparative Study. Exp Mech 2022;62:837–47. https://doi.org/10.1007/s11340-022-00835-9.

[15] Senck S, Scheerer M, Revol V, Plank B, Hannesschläger C, Gusenbauer C, et al. Microcrack characterization in loaded CFRP laminates using quantitative two- and three-dimensional X-ray dark-field imaging. Compos Part A Appl Sci Manuf 2018;115:206–14.

https://doi.org/10.1016/j.compositesa.2018.09.023.

[16] Revol V, Jerjen I, Kottler C, Schtz P, Kaufmann R, Lthi T, et al. Sub-pixel porosity revealed by x-ray scatter dark field imaging. J Appl Phys 2011;110. https://doi.org/10.1063/1.3624592.

[17] Lauridsen T, Willner M, Bech M, Pfeiffer F, Feidenhans'l R. Detection of sub-pixel fractures in X-ray dark-field tomography. Appl Phys A Mater Sci Process 2015;121:1243–50. https://doi.org/10.1007/s00339-015-9496-2.

[18] Jensen TH, Bech M, Bunk O, Donath T, David C, Feidenhans'L R, et al. Directional x-ray dark-field imaging. Phys Med Biol 2010. https://doi.org/10.1088/0031-9155/55/12/004.

[19] Schaff F, Prade F, Sharma Y, Bech M, Pfeiffer F. Non-iterative Directional Dark-field Tomography. Sci Rep 2017;7:1–9. https://doi.org/10.1038/s41598-017-03307-6.

[20] Glinz J, Thor M, Schulz J, Zabler S, Kastner J, Senck S. Non-destructive characterisation of out-of-plane fibre waviness in carbon fibre reinforced polymers by X-ray dark-field radiography. Nondestructive Testing and Evaluation 2022;37:497–507. https://doi.org/10.1080/10589759.2022.2063860.

[21] Rajak DK, Pagar DD, Kumar R, Pruncu CI. Recent progress of reinforcement materials: A comprehensive overview of composite materials. Journal of Materials Research and Technology 2019;8:6354–74. https://doi.org/10.1016/j.jmrt.2019.09.068.

[22] Jones RM. MECHANICS OF COMPOSITE MATERIALS. vol. SECOND EDITION. 2nd ed. Taylor & Francis Group; 1999. https://doi.org/10.1201/9781498711067.

[23] Reis JP, de Moura M, Samborski S. Thermoplastic composites and their promising applications in joining and repair composites structures: A review. Materials 2020;13:1–33. https://doi.org/10.3390/ma13245832.

[24] Barroeta Robles J, Dubé M, Hubert P, Yousefpour A. Repair of thermoplastic composites: an overview. Advanced Manufacturing: Polymer and Composites Science 2022;8:68–96. https://doi.org/10.1080/20550340.2022.2057137.

[25] Kiss P, Stadlbauer W, Burgstaller C, Stadler H, Fehringer S, Haeuserer F, et al. In-house recycling of carbon- and glass fibre-reinforced thermoplastic composite laminate waste into high-performance sheet materials. Compos Part A Appl Sci Manuf 2020;139. https://doi.org/10.1016/j.compositesa.2020.106110.

[26] Thyavihalli Girijappa YG, Mavinkere Rangappa S, Parameswaranpillai J, Siengchin S. Natural Fibers as Sustainable and Renewable Resource for Development of Eco-Friendly Composites: A Comprehensive Review. Front Mater 2019;6. https://doi.org/10.3389/fmats.2019.00226.

[27] Mikhaluk DS, Truong TC, Borovkov AI, Lomov S V., Verpoest I. Experimental observations and finite element modelling of damage initiation and evolution in carbon/epoxy non-crimp fabric composites. Eng Fract Mech 2008;75:2751–66. https://doi.org/10.1016/j.engfracmech.2007.03.010.

[28] Alam S, Yandek GR, Lee RC, Mabry JM. Design and development of a filament wound composite overwrapped pressure vessel. Composites Part C: Open Access 2020;2. https://doi.org/10.1016/j.jcomc.2020.100045.

[29] Regassa Y, Gari J, Lemu HG. Composite Overwrapped Pressure Vessel Design Optimization Using Numerical Method. Journal of Composites Science 2022;6. https://doi.org/10.3390/jcs6080229.

[30] Henning F, Ernst H, Brüssel R. LFTs for automotive applications. Reinforced Plastics 2005;49:24–33. https://doi.org/10.1016/S0034-3617(05)00546-1.

[31] Gandhi UN, Goris S, Osswald TA, Song Y-Y. Discontinuous Fiber-Reinforced Composites. Hanser; 2020. https://doi.org/10.3139/9781569906958.001.

[32] Winkelbauer J, Puchas G, Krenkel W, Schafföner S. Short fiber spraying process of all-oxide ceramic matrix composites: A parameter study. Int J Appl Ceram Technol 2022. https://doi.org/10.1111/ijac.14196.

[33] Dumont P, Orgéas L, Favier D, Pizette P, Venet C. Compression moulding of SMC: In situ experiments, modelling and simulation. Compos Part A Appl Sci Manuf 2007;38:353–68. https://doi.org/10.1016/j.compositesa.2006.03.010.

[34] Nawafleh N, Celik E. Additive manufacturing of short fiber reinforced thermoset composites with unprecedented mechanical performance. Addit Manuf 2020;33. https://doi.org/10.1016/j.addma.2020.101109.

[35] Maurer J, Jerabek M, Salaberger D, Thor M, Kastner J, Major Z. Stress relaxation behaviour of glass fibre reinforced thermoplastic composites and its application to the design of interrupted in situ tensile tests for investigations by X-ray computed tomography. Polym Test 2022;109. https://doi.org/10.1016/j.polymertesting.2022.107551.

[36] Al-Furjan MSH, Shan L, Shen X, Zarei MS, Hajmohammad MH, Kolahchi R. A review on fabrication techniques and tensile properties of glass, carbon, and Kevlar fiber reinforced rolymer composites. Journal of Materials Research and Technology 2022;19:2930–59. https://doi.org/10.1016/j.jmrt.2022.06.008.

[37] Joshi SC. The pultrusion process for polymer matrix composites. In: Advani SG, Hsiao K-T, editors. Woodhead Publishing Series in Composites Science and Engineering, Manufacturing Techniques for Polymer Matrix Composites (PMCs), Woodhead Publishing; 2012, p. 381–413. https://doi.org/10.1533/9780857096258.3.381.

[38] Biron M. Thermoplastic Processing. In: Biron M, editor. Thermoplastics and Thermoplastic Composites. 3rd ed., William Andrew Publishing; 2018, p. 767–820. https://doi.org/10.1016/b978-0-08-102501-7.00005-9.

[39] Kabir SMF, Mathur K, Seyam AFM. A critical review on 3D printed continuous fiber-reinforced composites: History, mechanism, materials and properties. Compos Struct 2020;232. https://doi.org/10.1016/j.compstruct.2019.111476.

[40] Fu Y, Yao X. A review on manufacturing defects and their detection of fiber reinforced resin matrix composites. Composites Part C: Open Access 2022;8. https://doi.org/10.1016/j.jcomc.2022.100276.

[41] Fu S-Y, Lauke B. EFFECTS OF FIBER LENGTH AND FIBER ORIENTATION DISTRIBUTIONS ON THE TENSILE STRENGTH OF SHORT-FIBER-REINFORCED POLYMERS. Compos Sci Technol 1996;56:1179–90. https://doi.org/10.1016/S0266-3538(96)00072-3.

[42] Thor M, Sause MGR, Hinterhölzl RM. Mechanisms of Origin and Classification of Out-of-Plane Fiber Waviness in Composite Materials—A Review. Journal of Composites Science 2020;4:130. https://doi.org/10.3390/jcs4030130.

[43] Alves MP, Cimini Junior CA, Ha SK. Fiber waviness and its effect on the mechanical performance of fiber reinforced polymer composites: An enhanced review. Compos Part A Appl Sci Manuf 2021;149. https://doi.org/10.1016/j.compositesa.2021.106526.

[44] Kulkarni P, Mali KD, Singh S. An overview of the formation of fibre waviness and its effect on the mechanical performance of fibre reinforced polymer composites. Compos Part A Appl Sci Manuf 2020;137:106013. https://doi.org/10.1016/j.compositesa.2020.106013.

[45] Leong KH, Lee B, Herszberg I, Bannister MK. The effect of binder path on the tensile properties and failure of multilayer woven CFRP composites. Compos Sci Technol 2000;60:149–56. https://doi.org/10.1016/S0266-3538(99)00108-6.

[46] Kousourakis A, Bannister MK, Mouritz AP. Tensile and compressive properties of polymer laminates containing internal sensor cavities. Compos Part A Appl Sci Manuf 2008;39:1394–403. https://doi.org/10.1016/j.compositesa.2008.05.003.

[47] Shivakumar K, Emmanwori L. Mechanics of Failure of Composite Laminates with an Embedded Fiber Optic Sensor. J Compos Mater 2004;38:669–80. https://doi.org/10.1177/0021998304042393.

[48] Glinz J, Šleichrt J, Kytýř D, Ayalur-Karunakaran S, Zabler S, Kastner J, et al. Phase-contrast and dark-field imaging for the inspection of resin-rich areas and fiber orientation in non-crimp vacuum infusion carbon-fiber-reinforced polymers. J Mater Sci 2021;56:9712–27. https://doi.org/10.1007/s10853-021-05907-0.

[49] Mehdikhani M, Gorbatikh L, Verpoest I, Lomov S V. Voids in fiber-reinforced polymer composites: A review on their formation, characteristics, and effects on mechanical performance. J Compos Mater 2019;53:1579–669.

https://doi.org/10.1177/0021998318772152.

[50] Han SH, Oh HJ, Kim SS. Evaluation of the impregnation characteristics of carbon fiber-reinforced composites using dissolved polypropylene. Compos Sci Technol 2014;91:55–62. https://doi.org/10.1016/j.compscitech.2013.11.021.

[51] Pace F, Stamopoulos A, Eckl M, Senck S, Glinz J. Analysis of the Manufacturing Porosity in Additively Manufactured Onyx/Long Fiber Reinforced Composites Using X-Ray Computed Tomography. Journal of Nondestructive Evaluation (Accepted Preprint) 2023.

[52] Olivier P, Cottu JP, Ferret B. Effects of cure cycle pressure and voids on some mechanical properties of carbon/epoxy laminates. Composites 1995;26:509–15. https://doi.org/10.1016/0010-4361(95)96808-J.

[53] Stamopoulos AG, Tserpes KI, Prucha P, Vavrik D. Evaluation of porosity effects on the mechanical properties of carbon fiber-reinforced plastic unidirectional laminates by X-ray computed tomography and mechanical testing. J Compos Mater 2016;50:2087–98. https://doi.org/10.1177/0021998315602049.

[54] Bayat S, Jamzad A, Zobeiry N, Poursartip A, Mousavi P, Abolmaesumi P. Temporal enhanced Ultrasound: A new method for detection of porosity defects in composites. Compos Part A Appl Sci Manuf 2023;164. https://doi.org/10.1016/j.compositesa.2022.107259.

[55] Kytýř D, Fíla T, Valach J, Šperl M. Evaluation of impact damage effect on fatigue life of carbon fibre composites. UPB Scientific Bulletin, Series D: Mechanical Engineering 2013;75:157–64.

[56] Kreculj D, Rašuo B. REVIEW OF IMPACT DAMAGES MODELLING IN LAMINATED COMPOSITE AIRCRAFT STRUCTURES. Tehnički Vjesnik - Tehnical Gazette 2013;20:485–95.

[57] Ogasawara T, Hirano Y, Yoshimura A. Coupled thermal-electrical analysis for carbon fiber/epoxy composites exposed to simulated lightning current. Compos Part A Appl Sci Manuf 2010;41:973–81. https://doi.org/10.1016/j.compositesa.2010.04.001.

[58] Guo Z, Li Q, Yu W, Arif W, Ma Y, Wah Hoon S. Experimental Study on Lightning Attachment Manner to Rotation Wind Turbine Blade. 34th International Conference on Lightning Protection, Rzeszow: 2018. https://doi.org/10.1109/ICLP.2018.8503300.

[59] Xu J, Yin Y, Paulo Davim J, Li L, Ji M, Geier N, et al. A critical review addressing drilling-induced damage of CFRP composites. Compos Struct 2022;294. https://doi.org/10.1016/j.compstruct.2022.115594.

[60] Bhatnagar N, Nayak D, Singh I, Chouhan H, Mahajan P. Determination of Machining-Induced Damage Characteristics of Fiber Reinforced Plastic Composite Laminates. Materials and Manufacturing Processes 2004;19:1009–23. https://doi.org/10.1081/AMP-200035177.

[61] Fotouhi S, Pashmforoush F, Bodaghi M, Fotouhi M. Autonomous damage recognition in visual inspection of laminated composite structures using deep learning. Compos Struct 2021;268. https://doi.org/10.1016/j.compstruct.2021.113960.

[62] Mizukami K, Mizutani Y, Kimura K, Sato A, Todoroki A, Suzuki Y, et al. Visualization and size estimation of fiber waviness in multidirectional CFRP laminates using eddy current imaging. Compos Part A Appl Sci Manuf 2016;90:261–70. https://doi.org/10.1016/j.compositesa.2016.07.008.

[63] Plasser H, Mayr G, Thummerer G, Hendorfer G, Burgholzer P, Major Z. Photothermal Porosity Estimation in CFRP by the Time-of-Flight of Virtual Waves. J Nondestr Eval 2020;39. https://doi.org/10.1007/s10921-020-00722-0.

[64] Burgholzer P, Thor M, Gruber J, Mayr G. Three-dimensional thermographic imaging using a virtual wave concept. J Appl Phys 2017;121. https://doi.org/10.1063/1.4978010.

[65] Thummerer G, Mayr G, Haltmeier M, Burgholzer P. Photoacoustic reconstruction from photothermal measurements including prior information. Photoacoustics 2020;19. https://doi.org/10.1016/j.pacs.2020.100175.

[66] Huijer A, Kassapoglou C, Pahlavan L. Acoustic emission monitoring of carbon fibre reinforced composites with embedded sensors for in-situ damage identification. Sensors 2021;21. https://doi.org/10.3390/s21206926.

[67] Schnars U, Henrich R. Applications of NDT Methods on Composite Structures in Aerospace

Industry. Proceedings of Conference on Damage in Composite Materials, 2006.
[68] Besher Baradi M, Cruz C, Riedel T, Régnier G. Frontal weld lines in injection-molded short fiber-reinforced PBT: Extensive microstructure characterization for mechanical performance evaluation. Polym Compos 2019;40:4547–58. https://doi.org/10.1002/pc.25310ï.
[69] Kastner J, Plank B, Salaberger D, Sekelja J. Defect and Porosity Determination of Fibre Reinforced Polymers by X-ray Computed Tomography. 2nd International Symposium on NDT in Aerospace, Hamburg: 2010, p. 1–12.
[70] Symons DD. Characterisation of indentation damage in 0/90 lay-up T300/914 CFRP. Compos Sci Technol 2000;60:391–401. https://doi.org/doi.org/10.1016/S0266-3538(99)00139-6.
[71] Tan KT, Watanabe N, Iwahori Y. X-ray radiography and micro-computed tomography examination of damage characteristics in stitched composites subjected to impact loading. Compos B Eng 2011;42:874–84. https://doi.org/10.1016/j.compositesb.2011.01.011.
[72] Jasiūnienė E, Yilmaz B, Smagulova D, Bhat GA, Cicėnas V, Žukauskas E, et al. Non-Destructive Evaluation of the Quality of Adhesive Joints Using Ultrasound, X-ray, and Feature-Based Data Fusion. Applied Sciences (Switzerland) 2022;12. https://doi.org/10.3390/app122412930.
[73] Rique AM, Machado AC, Oliveira DF, Lopes RT, Lima I. X-ray imaging inspection of fiberglass reinforced by epoxy composite. Nucl Instrum Methods Phys Res B 2015;349:184–91. https://doi.org/10.1016/j.nimb.2015.03.003.
[74] Dössel O. Bildgebende Verfahren in der Medizin - Von der Technik zur medizinischen Anwendung. 2nd ed. Heidelberg: Springer Vieweg Berlin; 2016. https://doi.org/10.1007/978-3-642-54407-1.
[75] Feldkamp LA, Davis LC, Kress JW. Practical cone-beam algorithm. J Opt Soc Am A 1984;1:612–9. https://doi.org/10.1364/JOSAA.1.000612.
[76] Kastner J, Heinzl C. X-Ray Tomography. In: Ida N, Meyendorf N, editors. Handbook of Advanced Nondestructive Evaluation, Springer, Cham; 2019, p. 1095–166. https://doi.org/10.1007/978-3-319-26553-7_5.
[77] Boas FE, Fleischmann D. CT artifacts: causes and reduction techniques. Imaging Med 2012;4:229–40. https://doi.org/10.2217/iim.12.13.
[78] Mayo S, Endrizzi M. X-Ray Phase Contrast Methods. In: Nathan I, Meyendorf N, editors. Handbook of Advanced Non-Destructive Evaluation, Springer, Cham; 2018, p. 1–42. https://doi.org/10.1007/978-3-319-30050-4_54-1.
[79] Olivo A, Castelli E. X-ray phase contrast imaging: From synchrotrons to conventional sources. Rivista Del Nuovo Cimento 2014;37:467–508. https://doi.org/10.1393/ncr/i2014-10104-8.
[80] Auweter SD, Herzen J, Willner M, Grandl S, Scherer K, Bamberg F, et al. X-ray phase-contrast imaging of the breast - Advances towards clinical implementation. British Journal of Radiology 2014;87. https://doi.org/10.1259/bjr.20130606.
[81] Zanette I, Weitkamp T, Lang S, Langer M, Mohr J, David C, et al. Quantitative phase and absorption tomography with an X-ray grating interferometer and synchrotron radiation. Physica Status Solidi (A) Applications and Materials Science 2011;208:2526–32. https://doi.org/10.1002/pssa.201184276.
[82] Herzen J, Donath T, Pfeiffer F, Bunk O, Padeste C, Beckmann F, et al. Quantitative phase-contrast tomography of a liquid phantom using a conventional x-ray tube source. Opt Express 2009;17:10010–8. https://doi.org/10.1364/oe.17.010010.
[83] Glinz J, Senck S, Reiter M, Schrempf A, Fürst D, Kastner J. Improved Visualization of Polymer Foams using Talbot-Lau Grating Interferometry to Reduce Metal Artifacts. Proceedings of the International Symposium on Digital Industrial Radiology and Computed Tomography, Fürth, Germany: 2019, p. 1–9.
[84] Donath T, Pfeiffer F, Bunk O, Grünzweig C, Hempel E, Popescu S, et al. Toward clinical X-ray phase-contrast CT: Demonstration of enhanced soft-tissue contrast in human specimen. Invest Radiol 2010;45:445–52. https://doi.org/10.1097/RLI.0b013e3181e21866.
[85] Kottler C, Revol V, Kaufmann R, Maake C, Stübinger S, Von Rechenberg B, et al. X-ray phase contrast imaging of soft tissue specimens. 2011 IEEE Nuclear Science Symposium Conference

Record, IEEE; 2011. https://doi.org/10.1109/NSSMIC.2011.6153855.

[86] Birnbacher L, Willner M, Marschner M, Pfeiffer D, Pfeiffer F, Herzen J. Accurate effective atomic number determination with polychromatic grating-based phase-contrast computed tomography. Opt Express 2018;26:15153–66. https://doi.org/10.1364/oe.26.015153.

[87] Gresil M, Revol V, Kitsianos K, Kanderakis G, Koulalis I, Sauer MO, et al. EVITA Project: Comparison Between Traditional Non-Destructive Techniques and Phase Contrast X-Ray Imaging Applied to Aerospace Carbon Fibre Reinforced Polymer. Applied Composite Materials 2017;24:513–24. https://doi.org/10.1007/s10443-016-9540-1.

[88] Ludwig V, Seifert M, Niepold T, Pelzer G, Rieger J, Ziegler J, et al. Non-destructive testing of archaeological findings by grating-based X-ray phase-contrast and dark-field imaging. J Imaging 2018;4. https://doi.org/10.3390/jimaging4040058.

[89] Gusenbauer C, Leiss-Holzinger E, Senck S, Mathmann K, Kastner J, Hunger S, et al. Characterization of medical and biological samples with a Talbot–Lau grating interferometer µXCT in comparison to reference methods. Case Studies in Nondestructive Testing and Evaluation 2016;6:30–8. https://doi.org/10.1016/j.csndt.2016.02.001.

[90] Arboleda C, Wang Z, Jefimovs K, Koehler T, Stevendaal U Van, Kuhn N, et al. Towards clinical grating-interferometry mammography. Eur Radiol 2019;30:1419–25. https://doi.org/10.1007/s00330-019-06362-x.

[91] Viermetz M, Gustschin N, Schmid C, Haeusele J, von Teuffenbach M, Meyer PBF, et al. Dark-field computed tomography reaches the human scale. Proceedings of the National Academy of Sciences 2022;119. https://doi.org/10.1073/pnas.2118799119.

[92] Kastner J, Plank B, Gusenbauer C, Senck S, Sasov A. Talbot-Lau grating interferometer X-ray computed tomography for the characterization of fiber-reinforced polymers. Digital Industrial Radiology and Computed Tomography, Ghent: 2015.

[93] Leatham TA, Paganin DM, Morgan KS. X-Ray Dark-Field and Phase Retrieval Without Optics, via the Fokker-Planck Equation. IEEE Trans Med Imaging 2023;42:1681–95. https://doi.org/10.1109/TMI.2023.3234901.

[94] Gassert FT, Urban T, Frank M, Willer K, Noichl W, Buchberger P, et al. X-ray dark-field chest imaging: Qualitative and quantitative results in healthy humans. Radiology 2021;301:389–95. https://doi.org/10.1148/radiol.2021210963.

[95] Johnston RE, Washburn D, Pisano E, Burns C, Thomlinson WC, Chapman LD, et al. Mammographic phantom studies with synchrotron radiation. Radiology 1996;200:659–63. https://doi.org/10.1148/radiology.200.3.8756911.

[96] Chapman D, Thomlinson W, Johnston RE, Washburn D, Pisano E, Gmür N, et al. Diffraction enhanced x-ray imaging. Phys Med Biol 1997;42:2015–25. https://doi.org/10.1088/0031-9155/42/11/001.

[97] Graetz J, Balles A, Hanke R, Zabler S. Review and experimental verification of X-ray dark-field signal interpretations with respect to quantitative isotropic and anisotropic dark-field computed tomography. Phys Med Biol 2020;65. https://doi.org/10.1088/1361-6560/abb7c6.

[98] Pfeiffer F, Kottler C, Bunk O, David C. Hard X-ray phase tomography with low-brilliance sources. Phys Rev Lett 2007;98:1–4. https://doi.org/10.1103/PhysRevLett.98.108105.

[99] Pfeiffer F, Bech M, Bunk O, Kraft P, Eikenberry EF, Brönnimann C, et al. Hard-X-ray dark-field imaging using a grating interferometer. Nat Mater 2008;7:134–7. https://doi.org/10.1038/nmat2096.

[100] Willer K, Fingerle AA, Gromann LB, De Marco F, Herzen J, Achterhold K, et al. X-ray dark-field imaging of the human lung - A Feasibility study on a deceased body. PLoS One 2019;13. https://doi.org/10.1371/journal.pone.0204565.

[101] Taphorn K, Kaster L, Sellerer T, Hötger A, Herzen J. Spectral X-ray dark-field signal characterization from dual-energy projection phase-stepping data with a Talbot-Lau interferometer. Sci Rep 2023;13. https://doi.org/10.1038/s41598-022-27155-1.

[102] Bonse U, Hart M. An X-ray interferometer with long separated interfering beam paths. Appl Phys Lett 1965;6:155–6. https://doi.org/10.1063/1.1754212.

[103] Goetz K, Kalashnikov MP, Mikhailov YA, Sklizkov G V, Fedotov SI, Foerster E, et al. Measurements of the parameters of shell targets for laser thermonuclear fusion using an x-ray schlieren method. Soviet Journal of Quantum Electronics 1968;9:607–10. https://doi.org/10.1070/QE1979v009n05ABEH009038.

[104] Wilkins SW, Nesterets YI, Gureyev TE, Mayo SC, Pogany A, Stevenson AW. On the evolution and relative merits of hard X-ray phase-contrast imaging methods. Philosophical Transactions of the Royal Society A: Mathematical, Physical and Engineering Sciences 2014;372. https://doi.org/10.1098/rsta.2013.0021.

[105] Paganin D, Mayo SC, Gureyev TE, Miller PR, Wilkins SW. Simultaneous phase and amplitude extraction from a single defocused image of a homogeneous object. J Microsc 2002;206:33–40. https://doi.org/10.1046/j.1365-2818.2002.01010.x.

[106] Morgan KS, Paganin DM, Siu KKW. Quantitative single-exposure x-ray phase contrast imaging using a single attenuation grid. J Phys D Appl Phys 2011;19:19781–9. https://doi.org/10.1364/OE.19.019781.

[107] Wang H, Kashyap Y, Cai B, Sawhney K. High energy X-ray phase and dark-field imaging using a random absorption mask. Sci Rep 2016;6. https://doi.org/10.1038/srep30581.

[108] Zdora MC. State of the Art of X-ray Speckle-Based Phase-Contrast and Dark-Field Imaging. J Imaging 2018;4. https://doi.org/10.3390/jimaging4050060.

[109] Olivo A, Speller R. Modelling of a novel x-ray phase contrast imaging technique based on coded apertures. Phys Med Biol 2007;52:6555–73. https://doi.org/10.1088/0031-9155/52/22/001.

[110] Berujon S, Wang H, Sawhney K. X-ray multimodal imaging using a random-phase object. Phys Rev A 2012;86. https://doi.org/10.1103/PhysRevA.86.063813.

[111] Endrizzi M, Murat BIS, Fromme P, Olivo A. Edge-illumination X-ray dark-field imaging for visualising defects in composite structures. Compos Struct 2015;134:895–9. https://doi.org/10.1016/j.compstruct.2015.08.072.

[112] Davis TJ, Gao D, Gureyev TE, Stevenson AW, Wilkins SW. Phase-contrast imaging of weakly absorbing materials using hard X-rays. Nature 1995;373:595–8. https://doi.org/10.1038/373595a0.

[113] Momose A, Kawamoto S, Koyama I, Hamaishi Y, Takai K, Suzuki Y. Demonstration of x-ray Talbot interferometry. Japanese Journal of Applied Physics, Part 2: Letters 2003;42. https://doi.org/10.1143/JJAP.42.L866.

[114] Talbot HF. LXXVI. Facts relating to optical science. No. IV . The London, Edinburgh, and Dublin Philosophical Magazine and Journal of Science 1836;9:401–7. https://doi.org/10.1080/14786443608649032.

[115] Zhang Z, Lei B, Zhao G, Ban Y, Da Z, Wang Y, et al. Distance and depth modulation of Talbot imaging via specified design of the grating structure. Opt Express 2022;30:10239. https://doi.org/10.1364/oe.449807.

[116] Weitkamp T, David C, Kottler C, Bunk O, Pfeiffer F. Tomography with grating interferometers at low-brilliance sources. Proc. SPIE 6318, Developments in X-Ray Tomography V, vol. 6318, SPIE; 2006, p. 63180S. https://doi.org/10.1117/12.683851.

[117] Pfeiffer F, Weitkamp T, Bunk O, David C. Phase retrieval and differential phase-contrast imaging with low-brilliance X-ray sources. Nat Phys 2006;2:258–61. https://doi.org/10.1038/nphys265.

[118] Olivo A. Edge-illumination x-ray phase-contrast imaging. Journal of Physics Condensed Matter 2021;33. https://doi.org/10.1088/1361-648X/ac0e6e.

[119] Lee S, Oh O, Kim Y, Kim D, Won J, Lee SW. Study on dark-field imaging with a laboratory X-ray source: Random stress variation analysis based on X-ray grating interferometry. Review of Scientific Instruments 2021;92. https://doi.org/10.1063/5.0011619.

[120] Weitkamp T, Diaz A, David C, Pfeiffer F, Stampanoni M, Cloetens P, et al. X-ray phase imaging with a grating interferometer. Opt Express 2005;13:6296–304. https://doi.org/10.1364/opex.13.006296.

[121] Velroyen A, Yaroshenko A, Hahn D, Fehringer A, Tapfer A, Müller M, et al. Grating-based X-ray Dark-field Computed Tomography of Living Mice. EBioMedicine 2015;2:1500–6. https://doi.org/10.1016/j.ebiom.2015.08.014.

[122] Epple FM, Potdevin G, Thibault P, Ehn S, Herzen J, Hipp A, et al. Unwrapping differential x-ray phase-contrast images through phase estimation from multiple energy data. Opt Express 2013;21:29101. https://doi.org/10.1364/oe.21.029101.

[123] Birnbacher L, Willner M, Velroyen A, Marschner M, Hipp A, Meiser J, et al. Experimental Realisation of High-sensitivity Laboratory X-ray Grating-based Phase-contrast Computed Tomography. Sci Rep 2016;6:1–8. https://doi.org/10.1038/srep24022.

[124] Massimi L, Savvidis S, Endrizzi M, Olivo A. Improved visualization of X-ray phase contrast volumetric data through artifact-free integrated differential images. Physica Medica 2021;84:80–4. https://doi.org/10.1016/j.ejmp.2021.03.024.

[125] Bech M, Bunk O, Donath T, Feidenhans'l R, David C, Pfeiffer F. Quantitative x-ray dark-field computed tomography. Phys Med Biol 2010;55:5529–39. https://doi.org/10.1088/0031-9155/55/18/017.

[126] Wang Z, Stampanoni M. Quantitative x-ray radiography using grating interferometry: A feasibility study. Phys Med Biol 2013;58:6815–26. https://doi.org/10.1088/0031-9155/58/19/6815.

[127] Donath T, Chabior M, Pfeiffer F, Bunk O, Reznikova E, Mohr J, et al. Inverse geometry for grating-based x-ray phase-contrast imaging. J Appl Phys 2009;106. https://doi.org/10.1063/1.3208052.

[128] Thuering T, Stampanoni M. Performance and optimization of X-ray grating interferometry. Philosophical Transactions of the Royal Society A: Mathematical, Physical and Engineering Sciences 2014;372. https://doi.org/10.1098/rsta.2013.0027.

[129] Yashiro W, Harasse S, Kawabata K, Kuwabara H, Yamazaki T, Momose A. Distribution of unresolvable anisotropic microstructures revealed in visibility-contrast images using x-ray Talbot interferometry. Phys Rev B Condens Matter Mater Phys 2011;84. https://doi.org/10.1103/PhysRevB.84.094106.

[130] Strobl M. General solution for quantitative dark-field contrast imaging with grating interferometers. Sci Rep 2014;4. https://doi.org/10.1038/srep07243.

[131] Lynch SK, Pai V, Auxier J, Stein AF, Bennett EE, Kemble CK, et al. Interpretation of dark-field contrast and particle-size selectivity in grating interferometers. Appl Opt 2011;50:4310–9. https://doi.org/10.1364/AO.50.004310.

[132] Malecki A, Potdevin G, Biernath T, Eggl E, Willer K, Lasser T, et al. X-ray tensor tomography. EPL (Europhysics Letters) 2014;105. https://doi.org/10.1209/0295-5075/105/38002.

[133] Prade F, Schaff F, Senck S, Meyer P, Mohr J, Kastner J, et al. Nondestructive characterization of fiber orientation in short fiber reinforced polymer composites with X-ray vector radiography. NDT and E International 2017;86:65–72. https://doi.org/10.1016/j.ndteint.2016.11.013.

[134] Felsner L, Hu S, Maier A, Bopp J, Ludwig V, Anton G, et al. A 3-D Projection Model for X-ray Dark-field Imaging. Sci Rep 2019;9. https://doi.org/10.1038/s41598-019-45708-9.

[135] Schaff F, Malecki A, Potdevin G, Eggl E, Noël PB, Baum T, et al. Correlation of x-ray vector radiography to bone micro-architecture. Sci Rep 2014;4. https://doi.org/10.1038/srep03695.

[136] Bayer F, Zabler S, Brendel C, Pelzer G, Rieger J, Ritter A, et al. Projection angle dependence in grating-based X-ray dark-field imaging of ordered structures. Opt Express 2013;21:19922. https://doi.org/10.1364/oe.21.019922.

5 Publications and scientific contribution

The following subchapters present the three most important peer-reviewed journal articles that have been published throughout the course of this doctoral work, as well as the preprint of a fourth article currently under review. A brief introduction and summary of the main findings are given for each article. Furthermore, contributions of each author are indicated following the CRediT taxonomy.[1] An overview of these scientific articles is shown in Fig. 27.

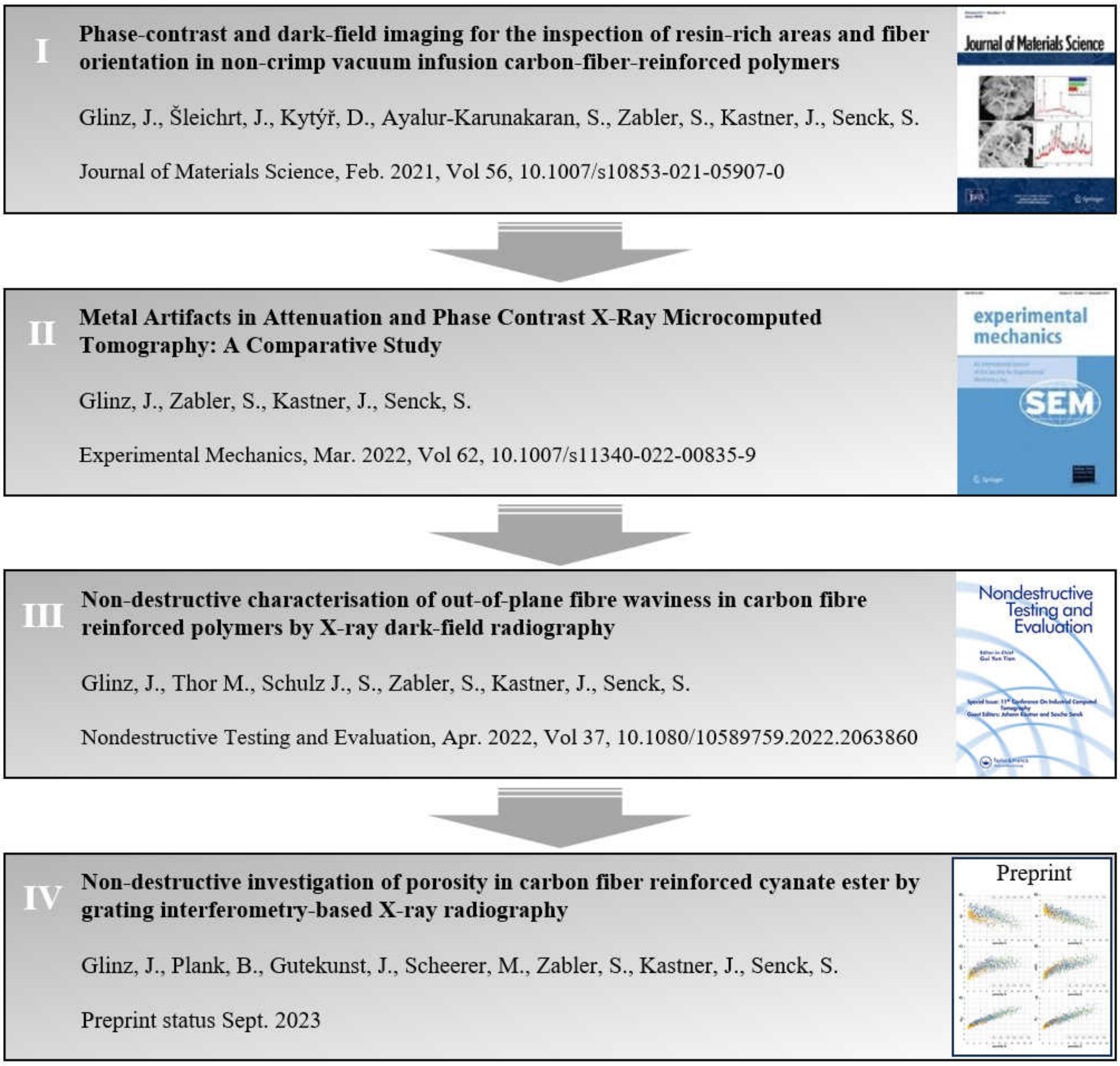

I **Phase-contrast and dark-field imaging for the inspection of resin-rich areas and fiber orientation in non-crimp vacuum infusion carbon-fiber-reinforced polymers**

Glinz, J., Šleichrt, J., Kytýř, D., Ayalur-Karunakaran, S., Zabler, S., Kastner, J., Senck, S.

Journal of Materials Science, Feb. 2021, Vol 56, 10.1007/s10853-021-05907-0

II **Metal Artifacts in Attenuation and Phase Contrast X-Ray Microcomputed Tomography: A Comparative Study**

Glinz, J., Zabler, S., Kastner, J., Senck, S.

Experimental Mechanics, Mar. 2022, Vol 62, 10.1007/s11340-022-00835-9

III **Non-destructive characterisation of out-of-plane fibre waviness in carbon fibre reinforced polymers by X-ray dark-field radiography**

Glinz, J., Thor M., Schulz J., S., Zabler, S., Kastner, J., Senck, S.

Nondestructive Testing and Evaluation, Apr. 2022, Vol 37, 10.1080/10589759.2022.2063860

IV **Non-destructive investigation of porosity in carbon fiber reinforced cyanate ester by grating interferometry-based X-ray radiography**

Glinz, J., Plank, B., Gutekunst, J., Scheerer, M., Zabler, S., Kastner, J., Senck, S.

Preprint status Sept. 2023

Fig. 27: Overview of scientific contributions.

---

[1] Brand, A., Allen, L., Altman, M., Hlava, M. and Scott, J. (2015), Beyond authorship: attribution, contribution, collaboration, and credit. Learned Publishing, 28: 151-155. https://doi.org/10.1087/20150211

These publications provide guidelines for characterizing lightweight materials and showcase industrial applications for TLGI. The first publication features an experimental study performed on vacuum-infusion-manufactured CFRP characterized via multimodal TLGI imaging. Next, a comparative study on the effects of beam hardening in attenuation and phase contrast imaging as experienced in a metal-polymer composite is presented. In the third publication, a new method for detecting and quantifying out-of-plane fiber waviness via TLGI radiography imaging is described. Finally, the fourth scientific contribution covers an experimental investigation on porosity within cyanate ester CFRP plates, where influences of varying specimen thickness on the results are considered.

Besides these journal articles, which are the main component of this doctoral thesis, numerous complementary scientific contributions have been published in the form of journal articles and conference proceedings. Although these works are not directly included in this doctoral thesis, they fit well within the wider scope of non-destructive testing of lightweight materials and thus complement the overall doctoral project. To remain within the constraints of this thesis, only full paper publications as the first author will be summarized, as follows:

1) J. Glinz et al., Fast Continuous In-Situ XCT of Additively Manufactured Carbon Fiber Reinforced Tensile Test Specimens, Acta Polytechnica CTU Proceedings, 2023 (Accepted for publication)
2) J. Glinz et al., Influence of Continuous Fiber Reinforcement on Tensile Properties in Fused Filament Fabricated Specimens, AIAA SciTech Forum 2023, American Institute of Aeronautics and Astronautics Inc., https://doi.org/10.2514/6.2023-2199
3) J. Glinz et al., In-situ Characterization of Additively Manufactured Continuous Fiber-Reinforced Tensile Test Specimens by X-ray Computed Tomography, AIAA SciTech Forum 2022, American Institute of Aeronautics and Astronautics Inc., https://doi.org/10.2514/6.2022-1426
4) J. Glinz et al., Inspection of Fiber Waviness in Carbon Fiber Laminates by Talbot-Lau X-ray Grating Interferometry, AIAA SciTech Forum 2021, American Institute of Aeronautics and Astronautics Inc., https://doi.org/10.2514/6.2021-0064
5) J. Glinz et al., In-situ Compression Test of Artificial Bone Foams in Controlled Environment using X-ray Micro-Computed Tomography. Acta Polytechnica CTU Proceedings, 2019, 25, 48–51. https://doi.org/10.14311/APP.2019.25.0048
6) J. Glinz et al., Porosity Determination in Additively Manufactured Ti Parts using X-ray Tomography. Proceedings of the 9th International Conference on Industrial Computed Tomography, 2019
7) J. Glinz et al., Determination of Pore Size Distribution and Finite Element Analysis of Additively Manufactured Ti Pedicle Screws using X-ray Microcomputed Tomography, Proceedings of the 12th European Conference on Non-destructive Testing, 2018
8) J. Glinz et al., Determination of Pore Size Distribution in Tannin- and Lignin-based Foams using X-ray Microcomputed Tomography, Proceedings of the 8th Conference on Industrial Computed Tomography, 2018

5.1 Phase-contrast and dark-field imaging for the inspection of resin-rich areas and fiber orientation in non-crimp vacuum infusion carbon-fiber-reinforced polymers

This work demonstrates the application of TLGI for inspecting CFRP specimens manufactured via vacuum infusion-assisted resin transfer molding. It shows that the complementary phase contrast and dark-field contrast images can be evaluated for increased contrast of resin-rich areas and additional information on fiber orientation within the specimens, respectively. Six token-sized specimens were cut from a larger component used in a passenger aircraft. The specimens were TLGI-XCT scanned in four different orientations to enable the extraction of fiber orientation within individual layers of the composite. Reference measurements were performed with a standard XCT device.

With the resulting DFC image data, a layer sequence consisting of 32 layers oriented in four main directions ([+45°/-45°/0°/90°]4S) was evaluated, while the increased contrast within DPC images allowed for a three-dimensional visualization of resin-rich areas. By combining both modalities, resin-rich areas could be differentiated into intra-layer and inter-layer resin-rich areas, predominantly caused by binder yarn collimation and fiber waviness, respectively. DFC imaging also proved useful for identifying resin-rich areas since the lack of fibers in those regions resulted in a significantly reduced scattering signal. Theoretically, the low requirements in spatial resolution qualify the methods presented for the investigation of larger components. However, the applicability of TLGIXCT is still limited to a rather small FOV due to, among other reasons, the difficulties in manufacturing sufficiently large gratings. Developments enabling a faster and more flexible application for defect characterization are still desirable.

Authorship contribution statement

J. Glinz: Conceptualization, Methodology, Validation, Formal Analysis, Investigation, Writing – Original Draft, Visualization, Funding Acquisition; **J. Šleichrt**: Investigation, Visualization, Writing – Review & Editing; **D. Kytýř**: Supervision, Writing – Review & Editing; **S. Ayalur-Karunakaran**: Resources; **S. Zabler**: Supervision, Writing – Review & Editing; **J. Kastner**: Supervision, Funding Acquisition, Writing – Review & Editing; **S. Senck**: Conceptualization, Methodology, Supervision, Project Administration, Funding Acquisition, Writing – Review & Editing

5.2 Metal Artifacts in Attenuation and Phase Contrast X-Ray Microcomputed Tomography: A Comparative Study

In this comparative study, the effects of beam hardening on image data recorded with X-ray attenuation and X-ray phase contrast computed tomography were explored. These effects are the cause for artifacts, particularly arising between and in close proximity to high-density components, and are a widely known problem in both medical and industrial investigations using XCT. To inspect beam-hardening effects on image quality, a phantom specimen consisting of polyamide and including four Ti6Al4V inserts was designed. Both the polyamide box and the Ti6Al4V inserts were additively manufactured by selective laser sintering and then mechanically joined. The specimen was subsequently investigated by phase contrast and attenuation-based XCT with varying amounts of metal pre-filtering and/or metal artifact reduction algorithm (MAR) applied. Finally, the artifacts and image quality were evaluated using the contrast-to-noise ratio (CNR), as well as a streak index, which provides a quantitative metric for assessing streak artifacts arising from beam hardening effects.

The results showed that the reduced sensitivity of phase contrast imaging to beam hardening effects can improve image quality in multi-material components and is matched by attenuation-based XCT only in combination with hardware pre-filtering of the X-ray beam and additional post-processing by a MAR algorithm. However, hardware pre-filtering worsens CNR, often requiring a compromise between CNR and effective artifact reduction to be made. Furthermore, artifacts in close proximity to the metal inserts could not be corrected sufficiently well, except by the use of phase contrast imaging. However, phase contrast imaging also introduced limitations, such as relatively low spatial resolution and artifacts caused by phase wrapping effects that need to be accounted for. Although phase contrast imaging is known to be less prone to metal artifacts caused by beam hardening, little effort has been thus made to compare it to other, more established methods. Therefore, in the course of this work, the first quantitative comparison of MAR, including phase contrast imaging XCT, was presented.

Authorship contribution statement

J. Glinz: Conceptualization, Methodology, Validation, Formal Analysis, Investigation, Writing – Original Draft, Visualization, Funding Acquisition; **S. Zabler**: Supervision, Writing – Review & Editing; **J. Kastner**: Supervision, Funding Acquisition, Writing – Review & Editing; **S. Senck**: Conceptualization, Methodology, Supervision, Project Administration, Funding Acquisition, Writing – Review & Editing

Experimental Mechanics
https://doi.org/10.1007/s11340-022-00835-9

RESEARCH PAPER

Metal Artifacts in Attenuation and Phase Contrast X-Ray Microcomputed Tomography: A Comparative Study

J. Glinz[1,2] · **S. Zabler**[3,4] · **J. Kastner**[2] · **S. Senck**[2]

Received: 11 August 2021 / Accepted: 25 February 2022

Abstract

Background Metal artifacts arising around high-density components are a widely known problem in X-ray computed tomography (XCT) for both medical and industrial applications. Although phase contrast imaging XCT (PCI-XCT) is known to be less prone to metal artifacts caused by beam hardening, so far only little effort was made for its comparison to other, more established methods.

Objective In the course of this work, this absence in literature is addressed by a quantitative comparison of PCI-XCT to attenuation contrast XCT (AC-XCT).

Methods A polymer specimen including four Ti6Al4V inserts was investigated by PCI- and AC-XCT with different pre-filter settings and metal artifact reduction (MAR) algorithm. Artifacts and image quality were evaluated by a streak index which provides a quantitative metric for the assessment of streak artifacts and contrast-to-noise ratio (CNR).

Results Results showed that streak artifacts are significantly reduced in PCI-XCT and only matched by AC-XCT in combination with hardware pre-filtering of the X-ray beam and post-processing by a MAR algorithm. However, hardware pre-filtering leads to worse CNR and artifacts close to the surface of metal inserts could not be removed sufficiently by the MAR algorithm.

Conclusions This work demonstrates the potential of PCI-XCT for the reduction of metal artifacts and presents the first quantitative comparison to established AC-XCT methods.

Keywords Metal artifacts · Beam hardening · Phase contrast imaging · X-ray microcomputed tomography

Introduction

In the past decades, X-ray microcomputed tomography (XCT) was established as an invaluable method for the three-dimensional characterization of components and materials. The possibility of an in-depth investigation of multi-material specimens is equally important in medical and industrial applications. However, XCT encounters some limitations when high-density materials such as metals are included in the specimen, particularly in close proximity to materials of lower density. The polychromatic nature of X-ray anodes in laboratory XCT devices causes well known beam hardening artifacts, which deteriorate the reconstructed XCT image data. Polychromatic beam hardening also plays an important role for metal artefacts which appear as bright and dark streaks between high-density objects (streak artifacts) [1]. Furthermore, gradients of decreasing grey values towards the center of otherwise homogeneous objects can appear (cupping artefacts).

Both streak and cupping artefacts are caused by the polychromatic X-ray spectrum which is not thoroughly considered in standard filtered backprojection (FBP) reconstruction algorithms. These algorithms are based on Lambert–Beer's law which implies a linear relationship between X-ray attenuation and specimen thickness and is strictly valid only for

---

✉ J. Glinz
jonathan.glinz@fh-wels.at

[1] Institut Für Werkstoffwissenschaft Und Werkstofftechnologie, TU Wien, Getreidemarkt 9, 1060 Wien, Austria

[2] Research Group Computed Tomography, University of Applied Sciences Upper Austria, Stelzhamerstraße 23, 4600 Wels, Austria

[3] Lehrstuhl Für Röntgenmikroskopie, Universität Würzburg, Josef-Martin-Weg 63, 97074 Würzburg, Germany

[4] Magnetic Resonance and X-Ray Department, Fraunhofer EZRT, Josef-Martin-Weg 63, 97074 Würzburg, Germany

monochromatic X-rays [2]. In a polychromatic spectrum, lower energy X-ray photons are attenuated more significantly. When beam hardening occurs, the X-ray spectrum is shifted to a higher mean energy while propagating through a specimen which results in a higher transmission as would be assumed from Lambert–Beer's law [3]. The resulting dark streaks between and around highly attenuating structures which are embedded in "softer" matrices usually appear in combination with bright ones as a result from high pass filtering in FBP reconstruction algorithms amplifying differences between adjacent pixels [4].

These streak artifacts are commonly encountered in XCT images of multi-material components, where they overlap with specimen features thereby hindering a proper materials segmentation by thresholding. Examples for metal artifacts in multi-material components like electrical plugs and circuit boards are shown in [5] and [6]. In medical imaging, these artifacts can greatly reduce the diagnostic value of XCT images and complicate the clinical reporting [7–9]. Typical scenarios of severe beam hardening occur in the monitoring of metal implants, e.g. after bone fracture. Meyer et al. [10] show cases of severe streak artifacts in patients with metallic hip prostheses, dental fillings and spine fixture. For these reasons, procedures to reduce beam hardening artifacts are a heavily addressed topic in medical imaging [3] and a considerable amount of scientific publications focus on their comparison [2, 7, 11–18]. However, phase contrast imaging (PCI) XCT, which is known to be less prone to metal artifacts caused by beam hardening effects [19, 20], has not yet been considered in these studies. In the course of this work, this absence in literature shall be addressed by a quantitative comparison of PCI to attenuation contrast (AC) XCT methods.

There are several techniques for the extraction of X-ray PCI explained in literature, such as analyzer crystal, propagation or edge illumination based methods [21]. In this work, we facilitate PCI by Talbot-Lau grating interferometer XCT (TLGI-XCT) [22]. In contrast to the majority of other methods, TLGI-XCT has rather low requirements in spatial and temporal coherence and is therefore applicable at most laboratory XCT devices with standard X-ray tubes [19]. As explained and demonstrated by Chabior et al. [19], beam hardening effects in PCI-XCT are qualitatively comparable to artifacts arising in AC-XCT. However, quantitatively, beam hardening artifacts are less pronounced because of a reduced dependency of X-ray refraction on X-ray energy. The linear attenuation coefficient μ is proportional to $\mu \sim 1/E^3$, while its equivalent in PCI $(2\pi/\lambda) \cdot \delta \sim 1/E$, where λ is the X-ray wavelength and δ the real refractive index decrement [19]. The dependency of attenuation and refraction on X-ray energy can also be expressed in terms of phase cross section σ_p and attenuation cross section σ_a. Figure 1 shows a comparison of σ_p and σ_a for titanium and carbon from 10 to 150 keV X-ray energy, in which the higher linearity of σ_p compared to σ_a is visible. Additionally, σ_p is up to three orders of magnitude higher than σ_a, which can result in better contrast-to-noise ratio (CNR) in PCI as shown by Zanette et al. [23] and Herzen et al. [24]. Because of this, PCI is most often used for the investigation of low density materials such as biological tissue [25] or polymers [26, 27]. Values for σ_p are calculated according to

$$\sigma_p = r_0 \lambda Z \tag{1}$$

where r_0 is the classical electron radius, the X-ray wavelength λ and the atomic number Z of the respective material [28].

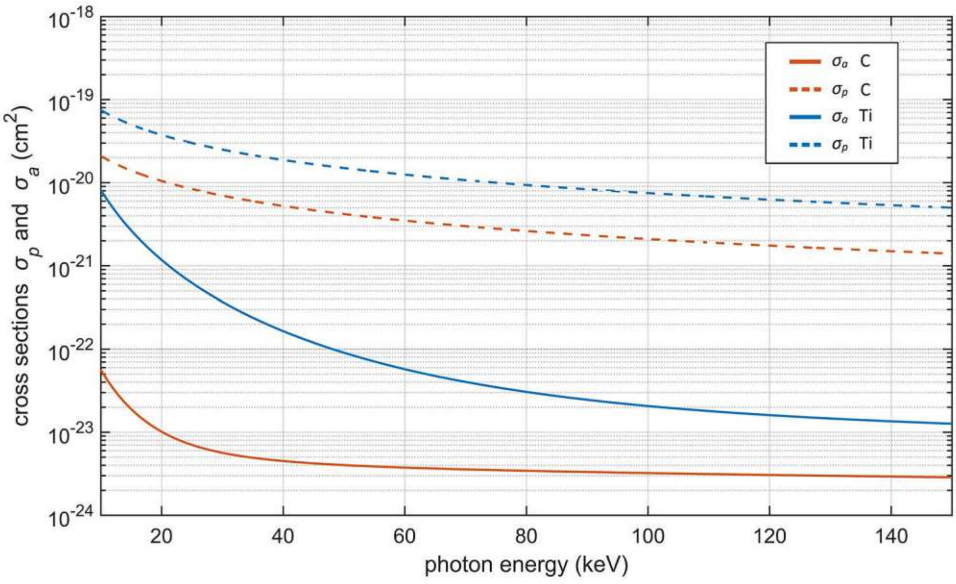

Fig. 1 Attenuation σ_a and phase cross section σ_p for titanium and carbon at X-ray energy from 10 to 150 keV. σ_p values were calculated according to equation (1) and σ_a values were obtained from XOP database [25]

Equation (1) is valid for X-ray energies far from absorption edges of the material. Values for σ_a are obtained from tabulated data in the XOP database software [29]. Further effects which contribute to a lower sensitivity of PCI-XCT to beam hardening effects are its reduced dependence on the actual signal intensity measured by the detector, and that in PCI using grating interferometry only a band of the X-ray energy spectrum, around the design energy of the interferometer, effectively contributes to the recorded phase image [30]. Gusenbauer et al. [31] have previously shown that PCI is capable to reduce metal artifacts in a carbon-fiber-reinforced polymer component including copper wires for lightning protection. Furthermore, Donath et al. [30] show a medical example of beam hardening artifact reduction by PCI.

In AC-XCT, one of the most commonly applied beam-hardening correction (BHC) methods is the pre-filtering of the X-ray beam with metallic plates (e.g. Al, Cu or Sn) which have 25%-50% of the objects attenuation length and remove low energy photons from the spectrum. Thereby, a harder energy spectrum is created at the expense of photon flux which generally contributes to a reduction of patient dose and beam hardening artifacts while slightly increasing the measurement time. I.e., the application of attenuation filters reduces photon statistics, leading to worse signal-to-noise ratios.

Another technique for the reduction of beam hardening effects which has been established particularly in medical imaging, is dual-energy XCT (DECT). At DECT, two images representing different energy spectra are recorded for every projection view and subsequently superimposed prior to XCT reconstruction. For most standard laboratory XCT devices this means two consecutive measurements at different acceleration voltages are required, which effectively at least doubles the measurement time. In medical XCT, dual source devices for the simultaneous acquisition of both energy channels are more commonly encountered. When the two different spectra are known, virtual monochromatic XCT images can be directly reconstructed from the dual projection data using an iterative reconstruction scheme. When applied at sufficiently high energy levels, these virtual monochromatic XCT images can reduce beam hardening artifacts significantly [4, 11]. However, consequently and contrary to PCI, contrast for low absorbing structures is reduced as well [11].

Besides DECT and attenuation-filtering digital metal artifact reduction (MAR) algorithms are commonly used due to their versatility and applicability on existing data. Consequently, many manufacturers of XCT systems already supply their devices with beam hardening correction methods, e.g. for the reduction of cupping effects, by default. MAR algorithms can be roughly categorized into physical effects correction (e.g. beam hardening, scatter, photon starvation), projection completion (interpolation) in the sinogram domain [32] and iterative reconstruction methods [33, 34]. However, hybrid forms combining different techniques have been developed as well [3]. Among these, the normalized MAR (NMAR) [10] was established as a state-of-the-art method [12, 34, 35]. Furthermore, MAR by deep learning methods gain increasing importance as computational power becomes more readily available with technological progress [34–36]. Comparative studies of different MAR algorithms for industrial [12] and medical applications [16, 37] can be found in literature. However, this work will extend literature by the quantitative comparison of PCI- to AC-XCT in combination with different hardware pre-filters and a MAR algorithm.

Materials and Methods

Specimen Design

For the investigation of beam hardening effects on image quality we designed a phantom specimen consisting of Polyamide 12 (PA12) including four Ti6Al4V inserts. The PA12 box of roughly 12×12×25 mm size was additively manufactured by selective laser sintering on an EOS P 396 device (EOS GmbH, Germany). The Ti6Al4V inserts of 1 mm diameter each were manufactured by selective laser melting on a Concept Laser M2 Cusing device (Concept Laser GmbH, Germany). The two components can be easily assembled and disassembled allowing measurements with and without metal parts in the specimen. A schematic image of the specimen can be seen in Fig. 2.

Experimental Setup and Parameters

Phase contrast measurements were performed on a SkyScan 1294 desktop device (Bruker microCT N.V., Belgium) which is a dedicated phase contrast system equipped with a Talbot-Lau grating interferometer formed by two absorption and one phase grating, with periods of 4.8 µm each, positioned in a symmetric setup. As the system was developed for a design energy of 30 keV, the maximum applicable acceleration voltage is limited to 50 kV. Additionally, a 0.045 mm thin copper pre-filter was applied to adjust the energy spectrum for the interferometry setup. For the measurement of titanium components this voltage is still rather low. However, a minimum transmission of roughly 7.5% was achievable. With a 4000×2672 pixel CCD camera in 2×2 binning mode the applicable voxel size of this system is fixed to 11.4 µm. Phase contrast images were extracted by a phase stepping procedure [38] in 4 steps over one grating period. As this effectively means a quadruplication of the acquisition time for each angular projection image, less projections and averaging were applied for PCI in order to reduce the total

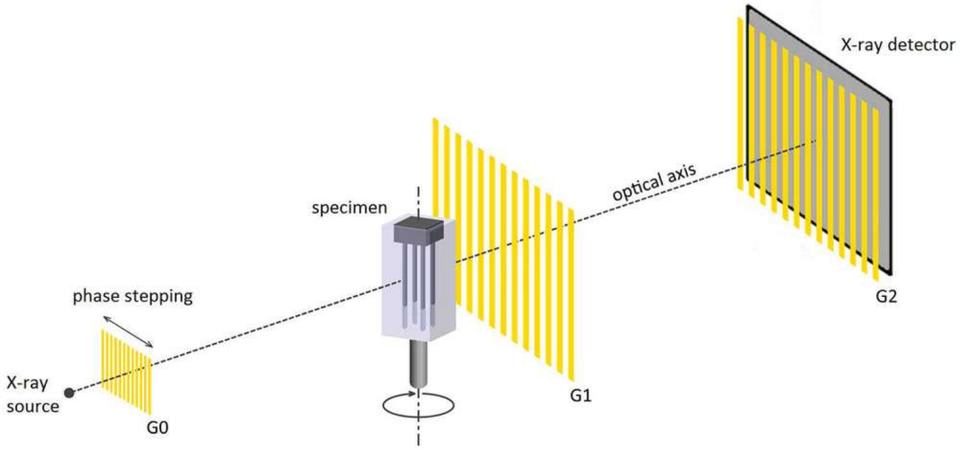

Fig. 2 Schematic grating interferometer setup of the SkyScan 1294 device used for phase contrast imaging. The specimen in the beam path as well as source- (G0), phase- (G1), and analyzer grating (G2) positions are indicated

scan time to approximately 3 h. Furthermore, to avoid grating misalignments caused by temperature drifts during the scans, the X-ray tube was conditioned for approximately 2 h prior to every scan. A voxel size calibration phantom (2 ruby ball bars, distance from sphere to sphere: 12 mm) was used for the calibration of voxel size in x–y and z direction.

Due to the low applicable voltage, the loss in photon flux caused by the interferometer gratings and the required phase stepping procedure, the SkyScan device is not particularly suited for standard AC measurements. Consequently, AC-XCT measurements were performed on a Nanotom 180NF (GE Sensing & Inspection Technologies GmbH, Germany) device for comparability. Two different parameter settings at 100 kV and 150 kV were used to investigate the effects of acceleration voltage in combination with varying pre-filter thickness on image quality. Furthermore, a reference scan of the PA12 box without titanium inserts was performed at a reduced acceleration voltage of 80 kV, to optimize image contrast. To allow for higher X-ray energies, a tungsten transmission target on diamond substrate was used in combination with a 2304 × 2304 pixel flat panel detector (Hamamatsu Photonics K.K., Japan). At the given specimen dimensions, a maximum resolution of 8 µm was achieved. The voxel size was calibrated by scanning of a commercially available ruby ball bar with 8 mm sphere distance. For comparability, measurement times were kept at approximately 3 h for all measurements. Detailed parameters are listed in Table 1.

Image Processing and Visualization

For comparability, all data sets have been reconstructed with the software X-AID (MITOS GmbH, Germany, version 2021.2.0, www.x-aid.de) by means of a filtered back-projection algorithm, which includes a feature for cupping and streaking artifact correction. The streak artifact correction method is based on an advanced NMAR algorithm and allows for an interactive reduction of streaks between and around high attenuating metal parts. Attenuation CT data was reconstructed with and without streaking correction for reference. Streak artifact correction parameters were determined empirically to minimize artifacts while avoiding overcorrection. No artifact correction was applied for PCI data. Reconstructed data was visualized in Volume Graphics Studio 3.4 (Volume Graphics GmbH, Germany) and aligned by a best fit algorithm.

Image Quality Metrics

For the quantification of streaking artifacts, we used a metric introduced by Cao et al. [39] which calculates the streak index (SI) on the basis of line profiles between two metal inserts as shown in Fig. 3. The equation defined by Cao et al. is as follows:

Table 1 Scanning parameters for attenuation- and TLGI-XCT

XCT-System	Voxel size µm	Voltage kV	Current µA	Exposure time ms	Projections	Averaging	Pre-filter mm	Time min
Nanotom 180 NF	8	100	120	500	2800	6	-	168
Nanotom 180 NF	8	150	150	800	2800	6	0.5 Cu	192
Skyscan 1294	11.4	50	1000	800	800	3	0.045 Cu	194
Nanotom 180 NF*	8	80	270	500	2800	6	-	168

*Parameters of the reference scan without titanium inserts

$$SI = \frac{1}{n} \times \sum_{i=1}^{n} \left(\frac{I_{ai} - I_{bi}}{\max\left(I_{ai}, I_{bi}\right) - M_b + C} \right) \tag{2}$$

where

$$I_a = \frac{I_{p1} + I_{p2}}{2} \tag{3}$$

and

$$I_b = \frac{I_{v1} + I_{v2}}{2} \tag{4}$$

However, equation (2) was slightly altered as it is designed for integer type datasets. As we were using floating comma point data for this work, the constant C, which keeps the SI in a range below 1, can be omitted. M_b is defined as the mean grey value in the image background (air) from a region not affected by streak artefacts. $I_{p1,2}$ and $I_{v1,2}$ are the line profile maxima and minima respectively, determined in the uncorrected dataset as shown in Fig. 3. Their positions in the line profile are used for the extraction of grey values in all following datasets. In the case of an overcorrection, the SI can reach negative values while (with the omission of C) a value above 1 indicates streak artifacts darker than the background grey value. From each data set, 60 line profiles were extracted from pore free regions and evaluated as explained above.

In order to compare the overall image quality and possible effects of MAR, the CNR was calculated subsequently according to [24]:

$$CNR = \frac{\left|\mu_m - \mu_b\right|}{\sqrt{\sigma_m^2 + \sigma_b^2}} \tag{5}$$

where μ_m and μ_b are the mean signals and σ_m and σ_b their standard deviations measured in the material and background (air) respectively. Material values were extracted from the whole cross section of the PA12 box excluding pores and titanium inserts. Pores and drill holes for titanium inserts were determined via a reference scan of the PA12 box without titanium inserts and subtracted from the cross-sections. For every dataset, CNR values were extracted in a region affected by streak artefacts and in an artefact free region below the height of the metal inserts for comparison.

Results

Reconstructed slice images of the specimen resulting from different beam hardening correction methods are shown in Fig. 4. Without the application of a pre-filter to remove low energy photons from the spectrum, severe streak artifacts emerge between and around the metal inserts (Fig. 4(a)) in AC-XCT. The streak artifacts cover potentially interesting structures in the lower attenuating polymer and, e.g., evaluation of porosity will be heavily affected. Also, with the application of a MAR algorithm, these artifacts are too severe to be completely removed by post-processing of the data (Fig. 4(b)). By application of a 0.5 mm copper pre-filter, streak artifacts can be significantly reduced, but not completely avoided as shown in Fig. 4(c). Though, with subsequent application of a MAR algorithm, a streak index close to zero can be achieved without significant overcorrection (Fig. 4(d)). In PCI-XCT streak artifacts are perceptibly lower. However, because of the high refraction of X-rays caused at the metal inserts, additional streaks in radial direction of the inserts arise because of phase wrapping effects [23]. Furthermore, when comparing PCI and AC slice images, the metal inserts appear to be larger in AC, because of their much higher attenuation in reference to the surrounding polymer. Consequently, the metal appears to be radiating across its actual material borders, which complicates the visualization of structures in close proximity to the metal inserts.

In Fig. 5, boxplots of the streak index for 60 line profiles in each dataset are shown. The mean streak index according to equation (2) is indicated with a cross (x) and outliers with a plus (+) symbol. The biggest improvement in SI by MAR algorithm can be observed in the AC dataset without pre-filtering applied, reducing it to a similar level as for the AC dataset with 0.5 mm copper pre-filter, but without MAR algorithm applied. This pre-filtered AC dataset can further

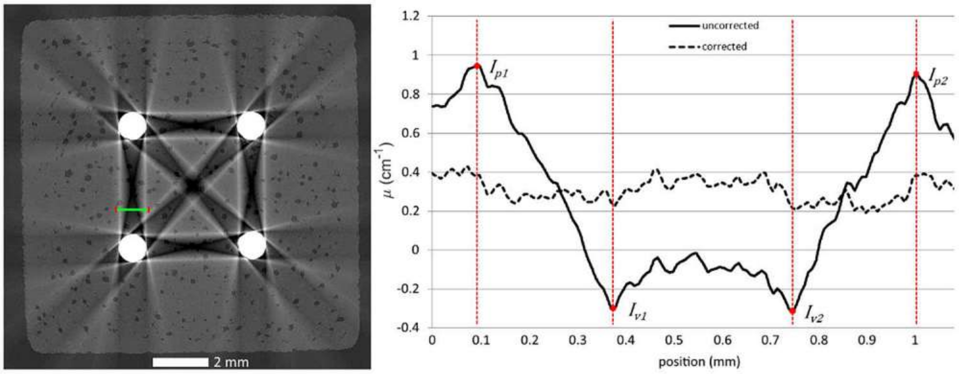

Fig. 3 Line profile across a streak artifact as indicated in the cross-section (green line) on the left. Maxima and minima (Ip1,2 and Iv1,2) detected in the uncorrected dataset are shown in comparison to the same line profile from a dataset corrected using a MAR algorithm

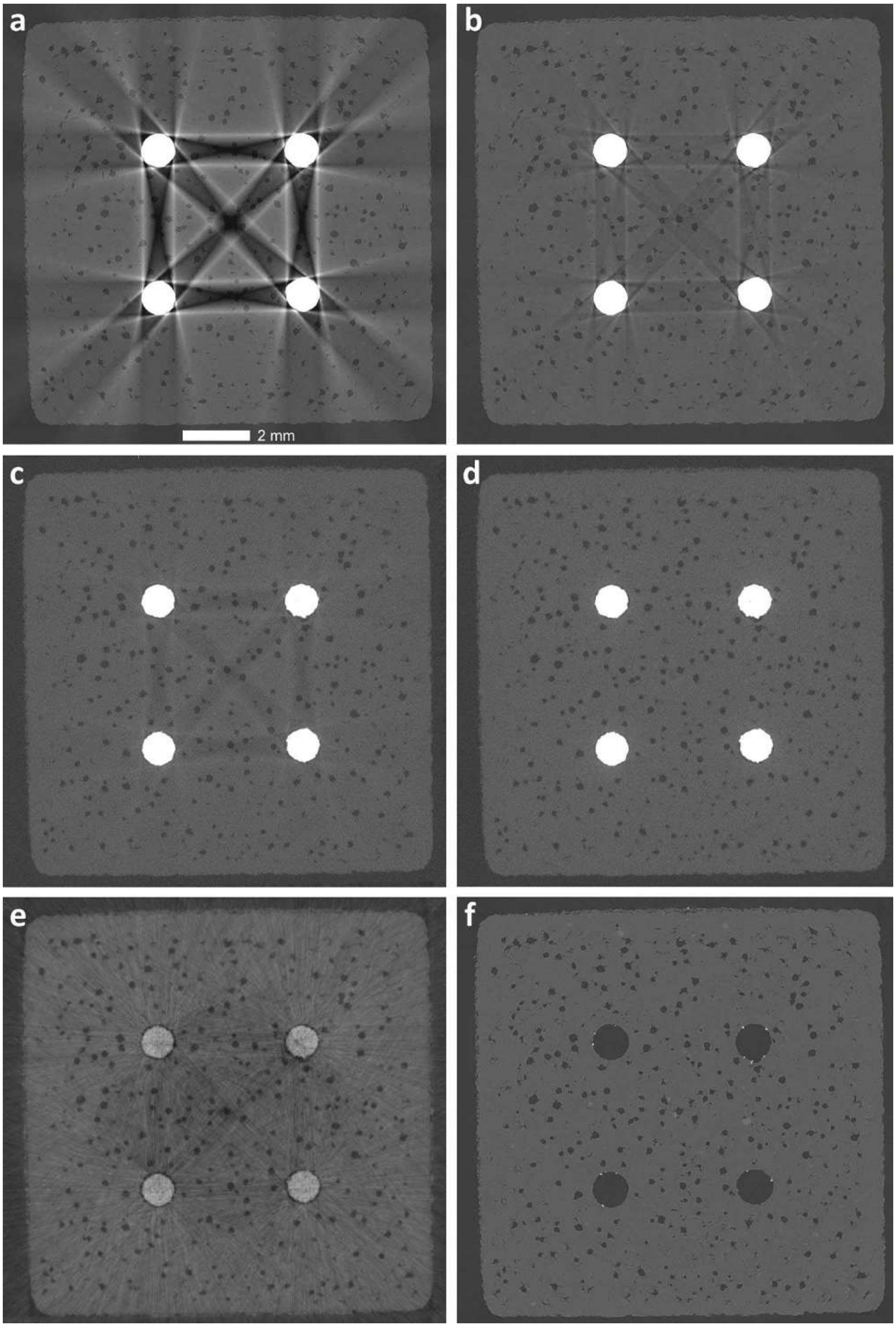

Fig. 4 Cross-sectional images of the specimen. (**a**) AC-XCT without pre-filter, without MAR. (**b**) AC-XCT without pre-filter, with MAR. (**c**) AC-XCT with 0.5 mm Cu pre-filter, without MAR (**d**) AC-XCT with 0.5 mm Cu pre-filter, with MAR. (**e**) PCI-XCT (**f**) AC-XCT reference scan without metal inserts. In PCI-XCT, additional streak artifacts emerging radial from the metal inserts (caused by phase wrapping) are visible

be corrected to a SI close to zero, while the SI of the PCI dataset levels somewhere midrange between MAR corrected and uncorrected pre-filtered AC data. As a reference, the SI in a dataset without metal inserts is plotted as well, which is slightly below zero, because of image noise.

For the investigation of edge sharpness and the effects of metal artifacts on the detectability of material interfaces, additional line profiles across two pores as well as one metal insert are shown in Fig. 6. Line profiles were plotted for both datasets with MAR algorithms applied, the PCI-XCT dataset and the dataset without metal inserts. A lower edge sharpness in PCI-XCT due to the reduced spatial resolution caused by the extended source size of the SkyScan system [40] can be seen by the reduced slope at pore interfaces. Additional edge enhancement in attenuation XCT data, caused by propagation based phase effects, is visible in some

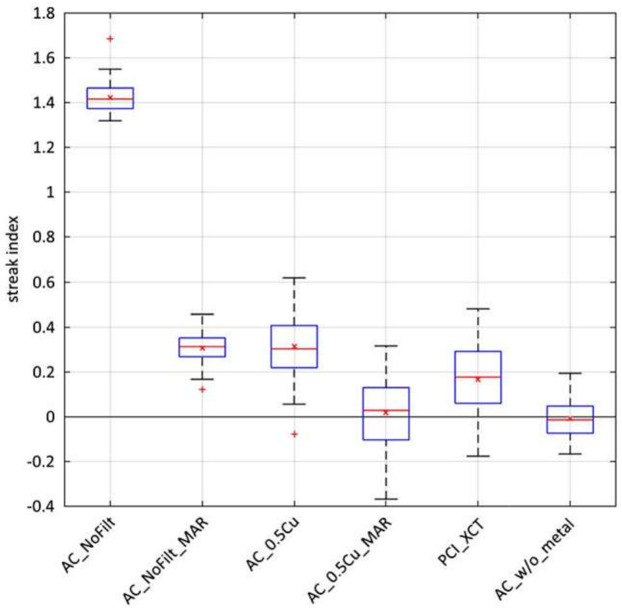

Fig. 5 Streak index boxplots for all datasets investigated. From left to right: AC-XCT without pre-filter, without MAR. AC-XCT without pre-filter, with MAR. AC-XCT with 0.5 mm Cu pre-filter, without MAR. AC-XCT with 0.5 mm Cu pre-filter, with MAR. PCI-XCT. AC-XCT without metal inserts. The mean streak index is indicated by a cross (x), outliers with a plus (+) symbol

cases. The low CNR in pre-filtered data is also clearly visible as well as declining grey values towards the center of the specimen in PCI. When comparing line profiles across the metal insert in AC and PCI, it becomes more obvious, that artifacts close to the metal surface overlap a gap between the metal insert and polymer box in AC. In PCI-XCT, such a gap is clearly visible in both the cross-section image and line profile. Mean grey values of the polymer material are indicated with dashed horizontal lines to highlight the increased grey values around the metal insert in AC.

CNRs in regions with and without streak artifacts are shown in Fig. 7. In regions without streak artifacts, unfiltered as well as PCI-XCT data show CNRs comparable to the reference measurement without metal inserts. However, in regions with streak artifacts, CNR is greatly reduced. Therefore, in unfiltered datasets, a significant part of CNR can be regained by application of artifact correction algorithms. Hardware pre-filtering on the other hand clearly reduces the CNR as a consequence of the reduction in photon count. Additionally, due to the higher acceleration voltage applied, increased photon energies lead to a reduction of the linear attenuation coefficient μ, which further reduces the CNR. Consequently, streak artifacts decrease the already low CNR only marginally as well as MAR algorithms have only minor effect on it. The CNR of PCI-XCT data positions on second place in the comparison. The consistent CNR in regions without streak artifacts before and after MAR algorithms were applied indicates that the applied algorithm affects only regions where actual streak artifacts are present. SI and CNR values evaluated are listed in Table 2.

Discussion

The comparison of five datasets with different streak artifact reduction approaches shows how significantly different contrast modalities can affect the resulting image quality. Besides well-established methods, such as hardware pre-filtering of the X-ray spectrum, we have shown that the reduced sensitivity of PCI-XCT to beam hardening effects can provide an alternative modality for investigations e.g. of multi material components. However, it is clear that PCI-XCT comes with its own limitations and problems when investigating multi material components including metal parts. As could be seen in Fig. 4(e), additional streak artifacts appearing in radial direction from the metal inserts can deteriorate image quality and also affect the CNR. Zanette et al. [23] found that such artifacts are entirely caused by phase wrapping effects whereas Massimi et al. [41] presented an artifact reduction algorithm significantly reducing these streaks recently. Moreover, a gradient towards lower grey values in the center of the specimen, between the metal inserts, can be observed. The reason for this lies in the X-ray energy dependent efficiency of the interferometer [30, 42]. Particularly the metal inserts cause a hardening of the X-ray spectrum and therefore a mismatch with the design energy of the grating interferometer. Consequently, a segmentation of the polymer material volume, e.g. by global threshold, is impeded. However, this effect can also be reduced by use of a more appropriate interferometer setup. The grating interferometer used for this work was not particularly designed for investigations including metal components, as its design energy lies at 30 keV with a maximum applicable peak energy of 50 keV. Using current state of the art interferometer gratings, significantly higher design and peak energies can be realized, which will positively affect beam hardening as well as measurement time can be reduced. Also, additional MAR methods for PCI-XCT may be developed, e.g. as shown by Yan et al. [43], who introduced a MAR method applicable for inhomogeneous, multi-material specimens.

The resulting SI in Fig. 5 showed that, in terms of streak artifacts, PCI-XCT is superior to AC-XCT when no MAR algorithms are applied. Nonetheless, larger, high density metallic components might still push PCI-XCT to its limits. The use of AC imaging in combination with pre-filters and/or MAR algorithms therefore is equally valid. Although, often a compromise between image noise and streak artifact reduction has to be made when hardware pre-filters are applied. In case of the specimen investigated, streak artifacts could not be completely removed by the MAR algorithm if

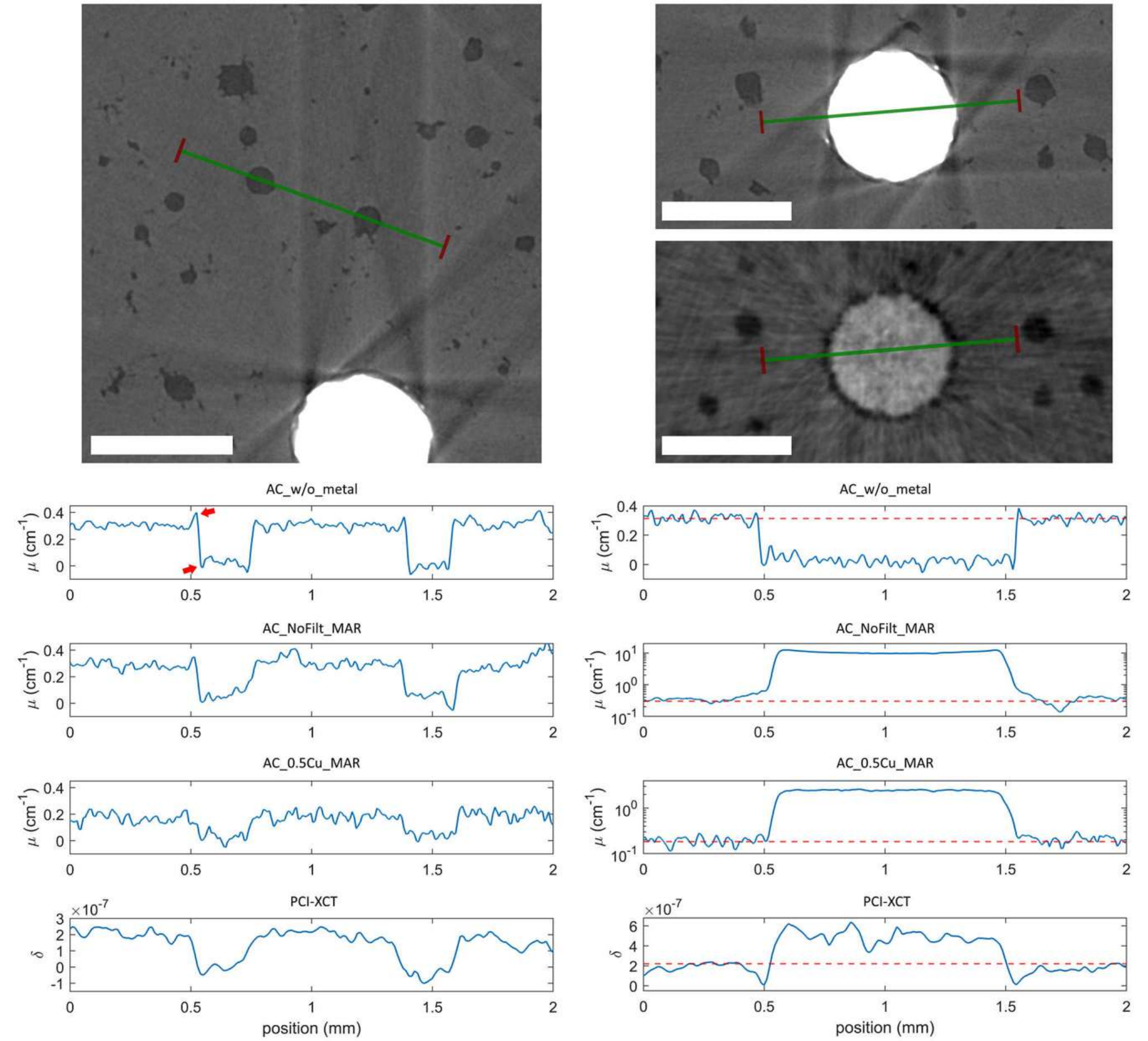

Fig. 6 Line profiles through two pores on the left and through a metal insert on the right. Polymer material mean grey values are indicated by horizontal dashed lines. Red arrows indicate edge enhancement caused by propagation based phase effects in AC_w/o_metal. Note the logarithmic scale in some of the plots. Scale bars correspond to 1 mm

no pre-filter was used at all. With a pre-filter of 0.5 mm Cu applied the remaining artifacts could be removed by the MAR algorithm sufficiently enough to achieve a SI of zero at a considerably reduced CNR. Consequently, a reduction of the pre-filter, e.g. to 0.2 mm Cu, might be the most obvious solution, as long as remaining artifacts can still be removed by MAR algorithms.

These MAR algorithms proved to be efficient for simple geometries as shown in this work. However, increasing size and geometrical complexity of metal parts will often lead to less satisfying results. Moreover, MAR algorithms can also introduce new artifacts, e.g. by overcorrection, as experienced at various examples in literature [15, 37, 44]. We also found, that although streak artifacts distant from the metal inserts can be removed acceptably well, artifacts close to the metal surface still remain. This can hinder the inspection of the metal-polymer interface and gaps between the materials might be underestimated or thin gaps even completely missed. Also in medical applications, regions in close proximity to metal implants often are of particular interest for diagnostic reasons [8].

The evaluation of CNR in streak affected and streak free regions indicates that the MAR algorithm used during this work does affect only regions where streak artifacts occur.

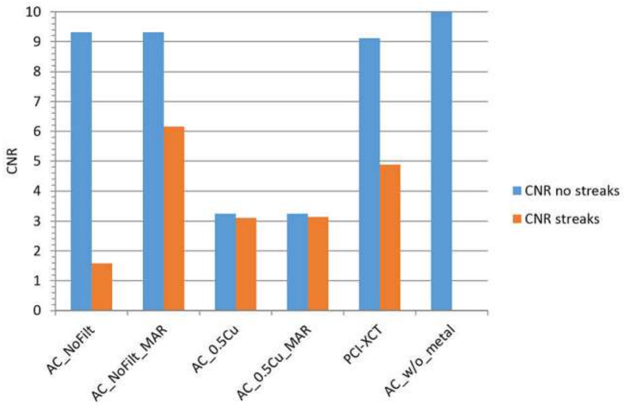

Fig. 7 Comparison of the CNR in all datasets investigated. Blue bars correspond to the CNR in regions unaffected by beam hardening artifacts. Orange bars correspond to the CNR in regions with beam hardening artifacts

In streak free regions, CNR is consistent before and after MAR. In case of the hardware pre-filtered datasets, CNR is mostly decreased by image noise and the reduced attenuation coefficient at high photon energies as the subsequent MAR has only little effect on it. On the contrary, datasets without pre-filtering show greatly increased CNR after the application of a MAR algorithm, indicating that the reduction in CNR is mostly caused by streak artifacts. The high CNR in PCI-XCT (being second only to the unfiltered but metal artifact corrected dataset) was previously also experimentally investigated by Zanette et al. [23] and Herzen et al. [24]. Furthermore, streak artifacts from phase wrapping effects as well as more pronounced ring artifacts most likely caused an additional reduction of CNR in the PCI-XCT dataset. Consequently, CNR could be enhanced significantly if respective artifact reduction methods are applied. However, the main focus of this work was the investigation of the influence of metal artifacts and artifact reduction methods on the CNR for which the uncorrected datasets are considered sufficient. For sake of comparability, parameters of individual measurements were chosen to achieve measurement times of approximately three hours. Nevertheless, PCI and pre-filtered AC scans took up to 26 min longer. Consequently, AC scans without pre-filtering might actually result in slightly better CNR values than depicted in Fig. 7.

Table 2 Streak index (SI) and contrast-to-noise ratio (CNR) evaluated in regions with and without streak artifacts of every dataset investigated

	SI	CNR no streaks	CNR streaks
AC_NoFilt	1.422 ± 0.066	9.315	1.582
AC_NoFilt_MAR	0.305 ± 0.066	9.315	6.157
AC_0.5Cu	0.313 ± 0.132	3.244	3.107
AC_0.5Cu_MAR	0.018 ± 0.161	3.244	3.131
PCI-XCT	0.167 ± 0.164	9.110	4.887
AC_w/o_metal	-0.008 ± 0.078	10.157	-

Conclusions

We have shown that the reduced sensitivity of PCI-XCT to beam hardening effects can improve streak artifacts in multi-material components. We presented the first quantitative comparison of PCI-XCT which has been widely neglected in comparative studies of MAR methods so far. Furthermore, PCI-XCT showed relatively high CNR while hardware pre-filtering in combination with MAR algorithms often requires a compromise between CNR and effective artifact reduction. However, PCI-XCT also comes with its own limitations such as relatively low spatial resolution and artifacts caused by phase wrapping. Most other drawbacks typically found in literature can widely be counteracted by use of appropriate phase contrast method and system design. To this end, PCI offers a lot of potential for industrial as well as medical applications. Future investigations will include the application to a selection of use-cases such as electronic devices or medical implants like bone fixations and artery stents.

Funding Open access funding provided by University of Applied Sciences Upper Austria. This work was financed by the project "Phad-CT" funded by the federal government of Upper Austria [FFG grant number: 875432], and the project "SpaceNDT" funded by the federal ministry for climate action, environment, energy, mobility, innovation and technology and the Austrian Space Applications Programme [FFG grant number: 866013].

Declarations

Conflict of Interests The authors declare that they have no known competing financial interests or personal relationships that could have appeared to influence the work reported in this paper.

References

1. Kastner J, Heinzl C (2019) X-ray tomography. In: Ida N, Meyendorf N (eds) Handbook of Advanced Nondestructive Evaluation. Springer, Cham, pp 1095–1166

2. Van de Casteele E (2004) Model-based approach for beam hardening correction and resolution measurements in microtomography. University of Antwerp, Belgium, pp 1–142 (PhD thesis)
3. Gjesteby L, De Man B, Jin Y et al (2016) Metal Artifact Reduction in CT: Where Are We After Four Decades? IEEE Access 4:5826–5849. https://doi.org/10.1109/ACCESS.2016.2608621
4. Boas FE, Fleischmann D (2012) CT artifacts: causes and reduction techniques. Imaging Med 4:229–240
5. Maier J (2019) Artifact Correction and Real-Time Scatter Estimation for X-Ray Computed Tomography in Industrial Metrology. Ruperto-Carola University, Heidelberg, pp 1–171. https://doi.org/10.11588/heidok.00026701 (PhD thesis)
6. Kano T, Koseki M (2017) Development of a multi-axis X-ray CT for highly accurate inspection of electronic devices. In: 7th Conference on Industrial Computed Tomography. Leuven, pp 1–7
7. Huang JY, Kerns JR, Nute JL et al (2015) An evaluation of three commercially available metal artifact reduction methods for CT imaging. Phys Med Biol 60:1047–1067. https://doi.org/10.1088/0031-9155/60/3/1047
8. Barrett JF, Keat N (2004) Artifacts in CT: Recognition and Avoidance. Radiographics 24:1679–1691. https://doi.org/10.1148/rg.246045065
9. Trieb K, Glinz J, Reiter M et al (2019) Non-Destructive Testing of Ceramic Knee Implants Using Micro-Computed Tomography. J Arthroplasty 34:2111–2117. https://doi.org/10.1016/j.arth.2019.05.006
10. Meyer E, Raupach R, Lell M et al (2010) Normalized metal artifact reduction (NMAR) in computed tomography. Med Phys 37:5482–5493. https://doi.org/10.1118/1.3484090
11. Katsura M, Sato J, Akahane M et al (2018) Current and novel techniques for metal artifact reduction at CT: Practical guide for radiologists. Radiographics 38:450–461. https://doi.org/10.1148/rg.2018170102
12. Gusenbauer C, Reiter M, Salaberger D, Kastner J (2016) Comparison of Metal Artefact Reduction Algorithms from Medicine Applied to Industrial XCT Applications. In: 19th World Conference on Non-Destructive Testing. Munich, pp 1–9
13. Diehn FE, Michalak GJ, DeLone DR et al (2017) CT Dental Artifact: Comparison of an Iterative Metal Artifact Reduction Technique with Weighted Filtered Back-Projection. Acta Radiol Open 6:1–8. https://doi.org/10.1177/2058460117743279
14. Joemai RMS, De Bruin PW, Veldkamp WJH, Geleijns J (2012) Metal artifact reduction for CT: Development, implementation, and clinical comparison of a generic and a scanner-specific technique. Med Phys 39:1125–1132. https://doi.org/10.1118/1.3679863
15. De Crop A, Casselman J, Van Hoof T et al (2015) Analysis of metal artifact reduction tools for dental hardware in CT scans of the oral cavity: kVp, iterative reconstruction, dual-energy CT, metal artifact reduction software: does it make a difference? Neuroradiology 57:841–849. https://doi.org/10.1007/s00234-015-1537-1
16. Wagenaar D, Van Der Graaf ER, Van Der Schaaf A, Greuter MJW (2015) Quantitative comparison of commercial and non-commercial metal artifact reduction techniques in computed tomography. PLoS ONE 10:1–9. https://doi.org/10.1371/journal.pone.0127932
17. Reiter M, de Oliveira FB, Bartscher M et al (2019) Case Study of Empirical Beam Hardening Correction Methods for Dimensional X-ray Computed Tomography Using a Dedicated Multi-material Reference Standard. J Nondestruct Eval 38:1–15. https://doi.org/10.1007/s10921-018-0548-3
18. Rodríguez-Gallo Y, Orozco-Morales R, Pérez-Díaz M (2021) Inpainting-filtering for metal artifact reduction (IMIF-MAR) in computed tomography. Phys Eng Sci Med 44:409–423. https://doi.org/10.1007/s13246-021-00990-8
19. Chabior M, Donath T, David C et al (2011) Beam hardening effects in grating-based x-ray phase-contrast imaging. Med Phys 38:1189–1195. https://doi.org/10.1118/1.3553408
20. Bevins N, Zambelli J, Li K et al (2011) Beam hardening in x-ray differential phase contrast computed tomography. In: Proceedings of the SPIE, pp 1–6
21. Endrizzi M (2018) X-ray phase-contrast imaging. Nucl Instruments Methods Phys Res Sect A Accel Spectrometers. Detect Assoc Equip 878:88–98. https://doi.org/10.1016/j.nima.2017.07.036
22. Pfeiffer F, Weitkamp T, Bunk O, David C (2006) Phase retrieval and differential phase-contrast imaging with low-brilliance X-ray sources. Nat Phys 2:258–261. https://doi.org/10.1038/nphys265
23. Zanette I, Weitkamp T, Lang S et al (2011) Quantitative phase and absorption tomography with an X-ray grating interferometer and synchrotron radiation. Phys Status Solidi Appl Mater Sci 208:2526–2532. https://doi.org/10.1002/pssa.201184276
24. Herzen J, Donath T, Pfeiffer F et al (2009) Quantitative phase-contrast tomography of a liquid phantom using a conventional x-ray tube source. Opt Express 17:10010–10018. https://doi.org/10.1364/oe.17.010010
25. Olivo A, Gkoumas S, Endrizzi M et al (2013) Low-dose phase contrast mammography with conventional x-ray sources. Med Phys 40:1–6. https://doi.org/10.1118/1.4817480
26. Gusenbauer C, Leiss-Holzinger E, Senck S et al (2016) Characterization of medical and biological samples with a Talbot-Lau grating interferometer µXCT in comparison to reference methods. Case Stud Nondestruct Test Eval 6:30–38. https://doi.org/10.1016/j.csndt.2016.02.001
27. Glinz J, Šleichrt J, Kytýř D et al (2021) Phase-contrast and dark-field imaging for the inspection of resin-rich areas and fiber orientation in non-crimp vacuum infusion carbon-fiber-reinforced polymers. J Mater Sci 56:9712–9727. https://doi.org/10.1007/s10853-021-05907-0
28. Zanette I (2011) Interférométrie X à réseaux pour l’imagerie et l’analyse de front d’ondes au synchrotron. Université Grenoble Alpes, France, pp 1–201 (PhD thesis)
29. Sanchez del Rio M, Dejus RJ (2004) Status of XOP: an x-ray optics software toolkit. In: Proc. SPIE, Bellingham, pp 171–174
30. Donath T, Pfeiffer F, Bunk O et al (2010) Toward clinical X-ray phase-contrast CT: Demonstration of enhanced soft-tissue contrast in human specimen. Invest Radiol 45:445–452. https://doi.org/10.1097/RLI.0b013e3181e21866
31. Gusenbauer C, Reiter M, Plank B et al (2017) Multi-modal Talbot-Lau grating interferometer XCT data for the characterization of carbon fibre reinforced polymers with metal components. In: Proceedings of the 7th Conference on Industrial Computed Tomography, pp 1–9
32. Amirkhanov A, Heinzl C, Reiter M et al (2011) Projection-Based Metal-Artifact Reduction for Industrial 3D X-ray Computed Tomography. IEEE Trans Vis Comput Graph 17:2193–2202. https://doi.org/10.1109/TVCG.2011.228
33. Hsieh J, Molthen RC, Dawson CA, Johnson RH (2000) An iterative approach to the beam hardening correction in cone beam CT. Med Phys 27:23–29. https://doi.org/10.1118/1.598853
34. Zhang Y, Member S, Yu H, Member S (2018) Convolutional Neural Network Based Metal Artifact Reduction in X-Ray Computed Tomography. IEEE Trans Med Imaging 37:1370–1381. https://doi.org/10.1109/TMI.2018.2823083
35. Gjesteby L, Yang Q, Xi Y et al (2017) Reducing Metal Streak Artifacts in CT Images via Deep Learning: Pilot Results. In: The 14th International Meeting on Fully Three-Dimensional Image Reconstruction in Radiology and Nuclear Medicine, pp 611–614
36. Willemink MJ (2019) The evolution of image reconstruction for CT – from filtered back projection to artificial intelligence. Eur Radiol 29(5):2185–2195
37. Golden C, Mazin SR, Boas FE et al (2011) A comparison of four algorithms for metal artifact reduction in CT imaging. Med Imaging 2011 Phys Med Imaging 7961:841–852. https://doi.org/10.1117/12.878896

38. Weitkamp T, Diaz A, David C et al (2005) X-ray phase imaging with a grating interferometer. Opt Express 13:6296–6304. https://doi.org/10.1364/OPEX.13.006296
39. Cao W, Sun T, Fardell G et al (2018) Comparative performance assessment of beam hardening correction algorithms applied on simulated data sets. J Microsc 272:229–241. https://doi.org/10.1111/jmi.12746
40. Birnbacher L, Willner M, Velroyen A et al (2016) Experimental Realisation of High-sensitivity Laboratory X-ray Grating-based Phase-contrast Computed Tomography. Sci Rep 6:1–8. https://doi.org/10.1038/srep24022
41. Massimi L, Savvidis S, Endrizzi M, Olivo A (2021) Improved visualization of X-ray phase contrast volumetric data through artifact-free integrated differential images. Phys Medica 84:80–84. https://doi.org/10.1016/j.ejmp.2021.03.024
42. Yashiro W, Vagovič P, Momose A (2015) Effect of beam hardening on a visibility-contrast image obtained by X-ray grating interferometry. Opt Express 23:23462–23471. https://doi.org/10.1364/oe.23.023462
43. Yan A, Wu X, Liu H (2017) Beam hardening correction in polychromatic x-ray grating interferometry. Opt Express 25:24690–24704. https://doi.org/10.1364/oe.25.024690
44. Wayer DR, Kim NY, Otto BJ et al (2019) Unintended consequences: Review of new artifacts introduced by iterative reconstruction CT metal artifact reduction in spine imaging. Am J Neuroradiol 40:1973–1975. https://doi.org/10.3174/ajnr.A6238

5.3 Non-destructive characterization of out-of-plane fiber waviness in carbon fiber reinforced polymers by X-ray dark-field radiography

Fiber waviness is a manufacturing defect frequently encountered in fiber-reinforced composites that can severely degrade the mechanical strength of a component. Consequently, detecting and characterizing unintended deviations from the designed fiber orientation are important tasks in the quality assessment of safety-critical components. This work proposed a new method for detecting and quantifying out-of-plane fiber waviness in carbon fiber composites that utilizes the directional sensitivity of X-ray dark-field imaging. In contrast to full XCT scanning of a specimen, this method relies on radiographic imaging of only a few angles to reduce measurement times and enable investigation of relatively large components. The method was tested on two token-sized specimens, including non-uniform, out-of-plane fiber waves with an amplitude of 2 mm at a length of 15 mm and 10 mm, respectively. These were compared to a reference specimen with identical fiber layup but no waviness.

Fiber waviness has been shown to be qualitatively detectable by single radiographic images due to the strong scattering signal caused by fibers aligned parallel to the X-ray beam. Furthermore, the study introduced a procedure for quantitatively evaluating waviness angles, which typically requires recording a series of projection images in the low two-digit range. With this approach, the maximum occurring wave angles could be determined within the test specimens at less than ± 1.5° error compared to results achieved by full computed tomography scans. Although some restrictions existed regarding detectable fiber orientation and some prior knowledge is necessary to minimize measurement time, the method provides a valid option, for example, for in-line monitoring, in which specimens of similar features and waviness are expected.

Authorship contribution statement

J. Glinz: Conceptualization, Methodology, Validation, Formal Analysis, Investigation, Writing – Original Draft, Visualization, Funding Acquisition; **M. Thor**: Resources; **J. Schulz**: Resources; **S. Zabler**: Supervision, Writing – Review & Editing; **J. Kastner**: Supervision, Funding Acquisition, Writing – Review & Editing; **S. Senck**: Supervision, Project Administration, Funding Acquisition, Writing – Review & Editing

Non-destructive investigation of porosity in carbon-fiber-reinforced cyanate ester by grating interferometry-based X-ray radiography

Authors: Jonathan Glinz[a,b,*], Bernhard Plank[b], Josephine Gutekunst[c], Michael Scheerer[d], Simon Zabler[e,f], Johann Kastner[b], Sascha Senck[b]

[a] Institut für Werkstoffwissenschaft und Werkstofftechnologie, TU Wien, Getreidemarkt 9, 1060 Wien, Austria
[b] University of Applied Sciences Upper Austria, Research Group Computed Tomography, Stelzhamerstraße 23, 4600 Wels, Austria
[c] Microworks GmbH, Schnetzlerstraße 9, 76137 Karlsruhe, Germany
[d] Aerospace & Advanced Composites GmbH, Viktor Kaplan-Straße 2, 2700 Wiener Neustadt, Austria
[e] Lehrstuhl für Röntgenmikroskopie, Universität Würzburg, Josef-Martin-Weg 63, 97074 Würzburg, Germany
[f] Deggendorf Institute of Technology DIT – Applied Computer Science, Josef-Görlitz-Platz 2, 94469, Deggendorf, Germany
* Corresponding author

Abstract:

In this work we explore the capabilities of Talbot-Lau grating interferometry (TLGI) radiography for the inspection of porosity in structural specimens of cyanate ester carbon fiber reinforced polymer. The influence of system resolution and varying specimen thicknesses on mean values and standard deviations (STDV) in all three image modalities acquired by TLGI are addressed. Results show that mean absorption contrast (AC) values are highly affected by specimen thickness and strong negative correlation ($r \leq -0.8$) is found only after correction via preliminary thickness measurements. Although dark-field contrast (DFC) is affected by changes in specimen thickness as well, the signal can be corrected by normalization with the inherently available AC. Consequently, strong positive correlation with porosity was found both in high- and low-resolution imaging ($r = 0.83$ and 0.71 respectively). Without the need for high image resolution or thickness measurements, the normalized DFC is a promising option for large field of view inspections. Investigations of STDV revealed strong positive correlations between porosity and AC STDV as well as differential phase contrast (DPC) STDV ($r = 0.95$ and 0.92 respectively) but high image resolution is required. Furthermore, results suggest increased robustness against variations in specimen thickness of AC and DPC STDV analyses.

Keywords: Cyanate ester composites, Porosity, Non-destructive testing, X-ray radiography, Grating interferometry

1 Introduction

Ever since the introduction of composite material systems to automotive, aerospace and energy related industries, the characterization of structural components has been of particular interest for manufacturers as well as maintenance and service providers. Cyanate esters are thermosetting polymers popular in aerospace applications due to favorable mechanical properties, low water absorption and high temperature stability [1,2]. Nevertheless, insufficient impregnation or inadequately chosen curing parameters can lead to porosity within carbon fiber reinforced polymers (CFRPs) often in the form of needle-shaped pores aligned with fiber orientation [3,4]. Such porosity can negatively affect the mechanical strength of a composite material as, e.g., interlaminar shear strength as well as tensile and flexural properties are directly relatable to component porosity [5–7]. Consequently, high demanding applications often require porosity contents not to exceed 1-2 % in finished components [8]. Especially in high aspect ratio components three-dimensional non-destructive testing (NDT) methods such as X-ray microcomputed tomography (XCT) often fail to provide results within reasonable time and detail. Therefore, radiographic methods for a faster inspection at larger field of view (FOV) are desirable. However, the quantification of porosity via X-ray absorption based radiographic testing (RT) has proven to be difficult as variations in specimen thickness directly affect the absorption signal.

With the development of dark-field- and phase-contrast sensitive methods such as Talbot-Lau grating interferometry (TLGI) [9,10] or Edge-Illumination based setups [11,12], new possibilities for the inspection of otherwise low contrast materials have emerged. The dark-field contrast (DFC) is sensitive to small angle scattering caused by microstructures even below the imaging resolution. In previous publications this sensitivity was utilized for the investigation of porosity in aluminum weld lines [13], micro cracks and porosity in CFRP [14–16], characterization of carbon fiber orientation [17–19], microstructures in biological materials [20] as well as further medical applications [21–23]. In comparison to the standard absorption contrast (AC) the differential phase contrast (DPC) shows higher sensitivity for low attenuating, low atomic number materials [24] such as polymers and biological tissue [25,26] and is less prone to beam hardening effects [27,28]. Recently, Shoukroun et al. [29] demonstrated how the refraction of X-rays at material interfaces affects the standard deviation (σ) of the DPC signal which consequently can be used for the inspection of porosity from structures larger than the imaging resolution, e.g., in CFRPs. Conversely, the sub-pixel detail detectability of the DFC makes it a promising modality for the detection of porosity below the imaging resolution such as micro-porosity between individual carbon fibers [30].

In this work we explore the effects of porosity in cyanate ester CFRP specimens on all three imaging modalities acquired by TLGI including changes in mean values as well as standard deviations of the signals. Furthermore, the effect of varying specimen thicknesses on recorded image modalities will be addressed as well. For that, two different TLGI setups are utilized to acquire high- and low-resolution images in small and large FOVs respectively.

2 Materials and Methods

Six specimens manufactured from unidirectional cyanate ester prepreg sheets (CNT-PT-30/Carbon fiber) at a quasi-isotropic layup of +45°/-45°/0°/90° fiber orientation were investigated (see Figure 1b). Specimen dimensions are 50 mm height, 20 mm with and $1.85^{\pm 0.07}$ mm in thickness.

Specimen porosity was determined by X-ray micro-CT on a Nanotom 180NF (GE Sensing & Inspection Technologies GmbH, Germany) device. At a voxel size of (12.5 µm)^3 a region of roughly 19 mm height in the center of each specimen could be captured. Consequently, the following evaluations were also limited to these regions. To account for porosity smaller than the imaging resolution, additional region of interest scans have been performed at (4.8 µm)^3 voxel size. Porosity was evaluated in these regions by ISO50 thresholding. Subsequently, the ISO threshold for porosity evaluation in the (12.5 µm)^3 voxel size data was adjusted until porosity values matched those of the higher resolution scans [31]. Specimen porosity ranged from roughly 2.5 % to 11 %.

The specimens were investigated in two different TLGI devices for low- and high-resolution radiography imaging. The low-resolution device consists of an interferometer grating setup of the “Talint-LAB” series with 40 keV design energy provided by microworks GmbH (Germany) implemented in a RayScan 250E device (see Figure 1a). The source- (G0), phase- (G1), and analyzer-grating (G2) are fabricated with periods of 10 µm, 8.9 µm and 8 µm respectively and are placed at distances of 72.5 cm (G0-G1) and 57.6 cm (G1-G2). At these specifications, the system allows relatively large components to be measured in a field of view of roughly 50x50 mm at an isometric resolution of 140 µm and an autocorrelation length of 2 µm. A specimen stage was implemented for remote controlled specimen centering and recording of flat-field references. The high-resolution device is a commercial Bruker Skyscan 1294 TLGI-XCT system with a design energy of 30 keV and grating periods of 4.8 µm each. Gratings are placed in a symmetric setup at 28 cm total length. At an isometric resolution of 5.7 µm (without binning) and an autocorrelation length of 1.6 µm a FOV of 20x16 mm can be imaged.

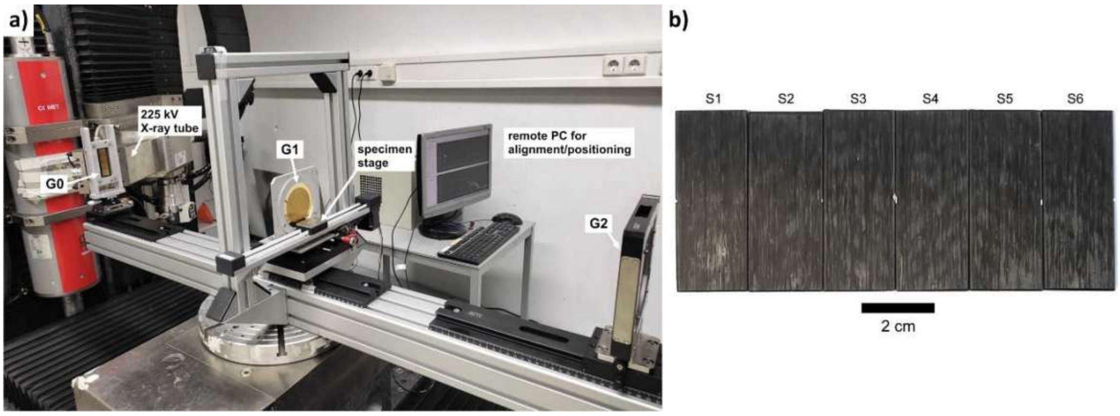

Figure 1: a) Photography of the low-resolution TLGI-System implemented in the RayScan 250E device. The X-ray detector is situated to the right of the G2 grating outside of the FOV. b) Photography of specimens S1 to S6.

Each specimen was imaged separately in the center of the FOV to avoid eventual shadowing effects towards the borders of the FOV [32]. Absorption, dark-field and phase contrast modalities were extracted by a phase stepping procedure [33] in 4 steps over one grating period. Each detector pixel thereby records a sinusoidal intensity function whose visibility is defined as $V = A/I_0$, with the signal amplitude A and mean intensity I_0. The change in mean intensity, visibility, and phase shift φ in reference to image data without a specimen in the beam path the absorption, dark-field and differential phase contrast can be calculated:

$$AC = -\ln\left(\frac{I_{0,obj}}{I_{0,ref}}\right), \qquad DFC = -\ln\left(\frac{V_{obj}}{V_{ref}}\right), \qquad DPC = \varphi_{obj} - \varphi_{ref} \tag{1}$$

To avoid image quality degradation, low-resolution AC images were recorded separately without interferometer gratings in the beam path of the RayScan device. High-resolution AC images were extracted from TLGI data, as the interferometer gratings of the Skyscan device are not removable. However, for each projection image 10 frames were averaged to compensate for low photon statistics. Detailed imaging parameters are listed in Table 1.

XCT-System	Voxel size	Voltage kV	Current µA	Exposure time ms	Projections	Averaging	Pre-filter mm
Rayscan w/ TLGI	140	60	2500	5000	1	-	-
Rayscan w/o TLGI	140	60	2500	1000	1	-	-
Skyscan 1294	11.4	35	1300	1300	1	10	0.025 Al
Nanotom 180 NF	12.5	60	260	900	1800	4	-

Table 1: Parameter settings for radiography and XCT measurements on the devices used.

To correct for variations in specimen thickness in DFC, the normalized DFC (nDFC) [34,35] was calculated using the AC of the respective TLGI measurement:

$$nDFC = \frac{DFC}{AC} \tag{2}$$

Since in TLGI the AC and DFC modality are acquired simultaneously, they are perfectly registered inherently. Furthermore, specimen thickness d was measured with a high precision outside micrometer to calculate the linear absorption coefficient from AC data:

$$\mu = \frac{AC}{d} \tag{3}$$

For the correlation analysis a quadratic region of (18x18) mm² within the recorded FOV was defined which was subsequently sectioned into 20x20 tiles, each significantly larger than the average pore diameter. Within these tiles, mean value and standard deviation (σ) of all three modalities were calculated and standardized to zero mean and unit standard deviation for comparability. However, mean values of the DPC signal were not further evaluated as the TLGI method is sensitive to the first derivative of the phase shift [24] and consequently, mean values should always be zero. Due to the limited FOV of the Skyscan system only the top 15 rows of these tiles have been evaluated. Furthermore, the gratings of the system are not bent to fit the cone beam geometry, which causes shadowing effects reducing the visibility close to the left and right borders of the FOV. Since the specimens barely fit the field of view, these effects can negatively influence the image quality of the measurements [32] which is why the 5 columns closest to the left and right image border were excluded from further evaluations. As the FOV of the low-resolution TLGI system is large enough that only approximately 50 % in width are covered by each specimen, shadowing effects are considered negligible.

Correlation (r) between individual imaging modalities and porosity was evaluated in MATLAB R2021b by means of two-sided Spearman correlation.

3 Results and discussion

In this section, the results from XCT porosity analysis in comparison to AC, DPC and DFC radiography measurements are presented. Resulting image data is plotted and for selected modalities the 20x20 tiles evaluated are shown in color coded distribution. Investigations of 3D-XCT data revealed that porosity within the specimens mainly occurs in the form of needle-shaped pores aligned with the direction of fiber orientation in the respective layer. Figure 2 shows the minimum intensity projections of the 3D-XCT data across the flat side of the specimens to give an overall impression of the porosity distribution within the specimens. Only the central, XCT scanned part of the specimens is shown, and regions evaluated for specimen porosity are indicated in cyan. Specimens S2, S5 and S6 appear notably darker indicating higher porosity compared to specimens S1, S3 and S4.

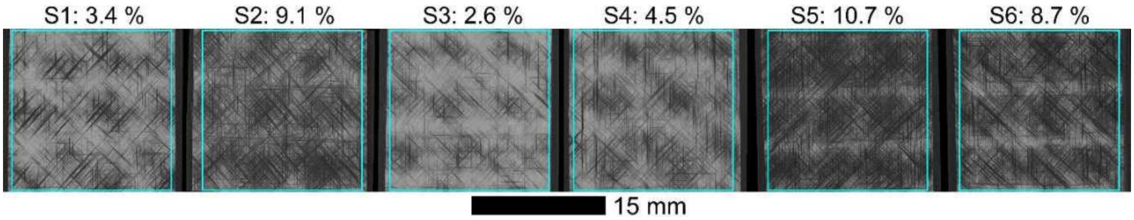

Figure 2: Minimum intensity projection of 3D-XCT volume data of specimen S1 to S6. The investigated regions are indicated in cyan. Porosity evaluated is indicated above each respective specimen.

The image data acquired via low- and high-resolution TLGI radiography are presented in Figure 3 and Figure 4 respectively. Due to the larger FOV of the low-resolution TLGI-system, the complete specimens could be depicted. However, since reference data from 3D-XCT is only available for the central indicated regions, only these were further evaluated. The high-resolution TLGI-system in return covers a FOV too small for the whole region of interest. Consequently, only the upper three quarters of each region were imaged with this system as notable in Figure 4.

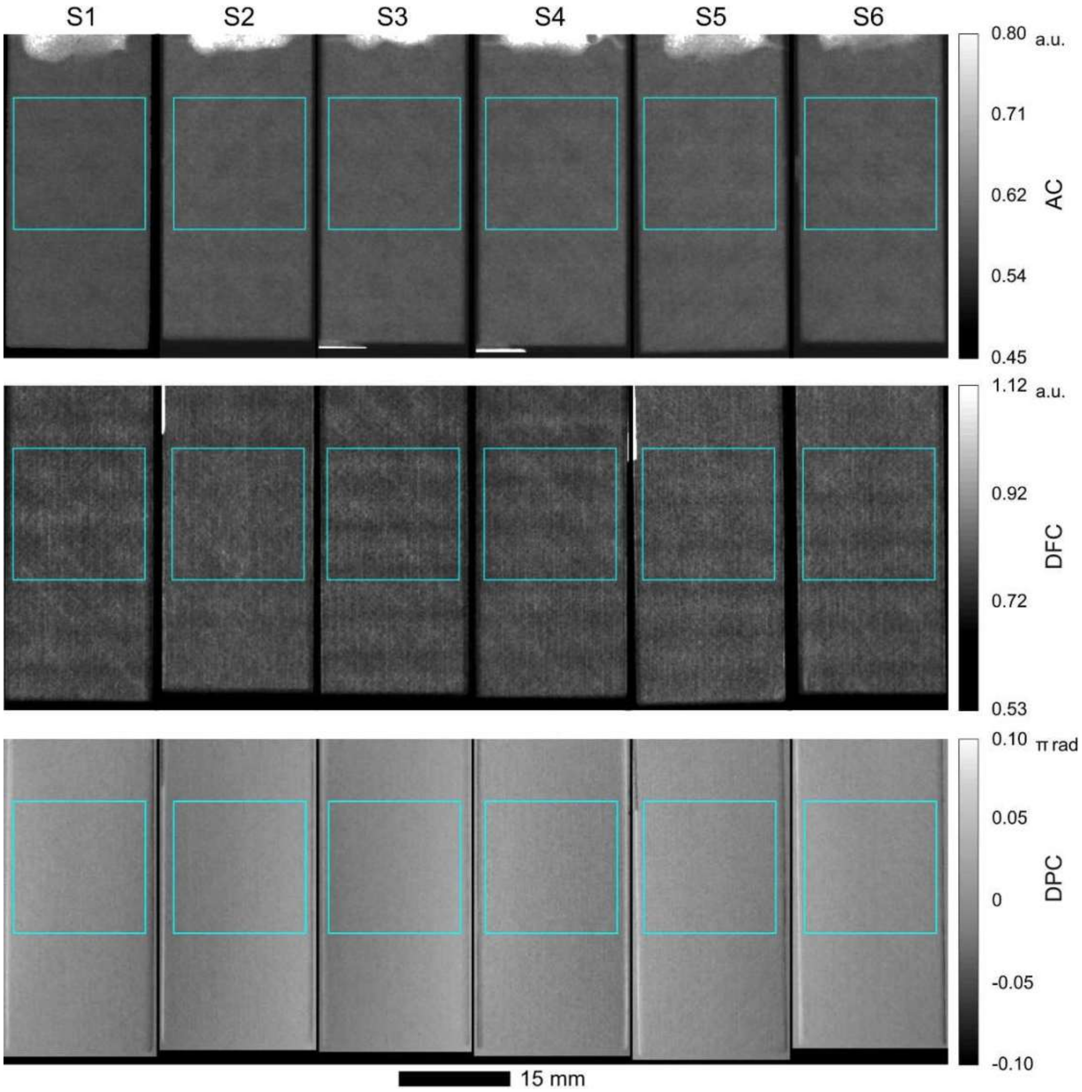

Figure 3: AC-, DFC- and DPC-radiography data recorded with the low-resolution TLGI-system. Specimens S1-S6 are shown from left to right. The regions evaluated are indicated by cyan squares.

The results from the correlation analysis are shown in Table 2. As expected, it is notable, that mean AC values show rather weak negative correlation ($r > -0.40$) with porosity because of the varying specimen thickness. After the correction for these variations by calculating the linear absorption coefficient μ, the correlation is significantly increased ($r \leq -0.8$). Similarly, the correction for variations in specimen thickness by calculating the nDFC increases the correlation of the dark field mean values up to $r = 0.71$ in low-resolution and $r = 0.83$ in high-resolution scans (see Figure 5c-d and Figure 6c-d). As mentioned earlier, mean values of the DPC signal were not further evaluated as they should always be zero inherently. Investigations of standard deviations revealed no significant correlation in dark-field modalities as well as low-resolution absorption- and phase-contrast data (see APPENDIX Fig. A.1 & A.2). However, very strong positive correlation ($r \geq 0.90$) was found between porosity and high-resolution absorption- and phase-contrast standard deviations (see Figure 6 e-h). All results shown proved to be significant ($P \ll 0.05$) with exception of standard deviation data from dark-field modalities and low-resolution $\sigma_{DPC} \cdot$ mm-1.

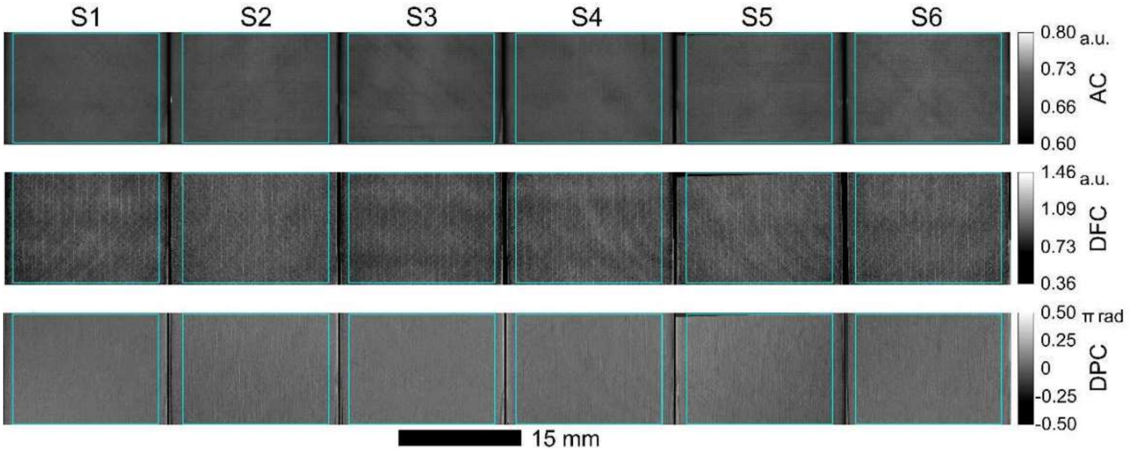

Figure 4: AC-, DFC- and DPC-radiography data recorded with the high-resolution TLGI-system. Specimens S1-S6 are shown from left to right. The regions evaluated are indicated by cyan squares. Note that the regions evaluated are smaller in height due to the limited FOV of the system.

	r	
Modality	**Low-res**	**High-res**
AC	-0.33	-0.40
μ	-0.86	-0.80
σ_{AC}	0.11	0.95
σ_{μ}	-0.06	0.93
DFC	0.64	0.74
nDFC	0.71	0.83
σ_{DFC}	-0.12	-0.12
σ_{nDFC}	-0.06	0.12
σ_{DPC}	0.18	0.92
$\sigma_{DPC} \cdot mm^{-1}$	0.02	0.90

Table 2: Correlation (r) for all modalities evaluated from low- and high-resolution data.

The comparison of AC and μ mean values in Figure 5a-b (low-res) and Figure 6a-b (high-res) shows the effect of specimen thickness on the AC signal. While correlation between AC and porosity is strong within each individual specimen ($r \leq -0.62$), differences in specimen thickness cause an offset between specimens, reducing the overall correlation. Although thickness among specimens varies in a range of less than ±4 %, the effect on AC correlation with porosity is obvious. This effect can be observed in low- as well as high-resolution scans and can be considered the main limiting factor for AC measurements without preliminary thickness evaluations. After taking specimen thickness into consideration by calculation of μ, relatively strong (negative) correlation with porosity could be achieved. Since μ was calculated with a single value acquired by measurement with an outside micrometer, thickness variations within a specimen naturally are not taken into consideration.

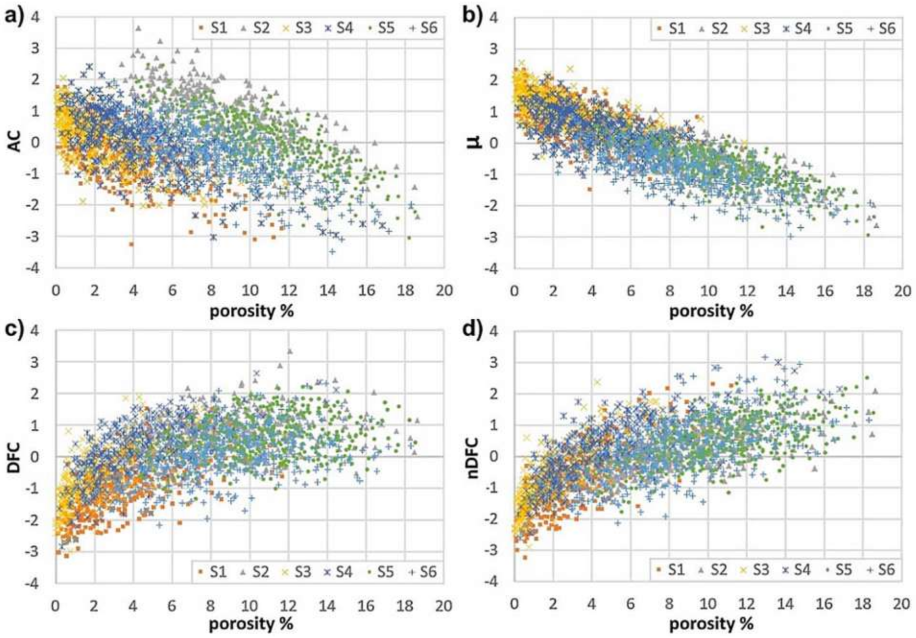

Figure 5: Mean values within each tile evaluated from low-resolution data plotted against porosity. Data is standardized to zero mean and unit standard deviation. a) AC without correction for specimen thickness. b) AC with correction for specimen thickness (µ). c) DFC without correction for specimen thickness. d) normalized DFC (nDFC).

The influence of specimen thickness on standard deviation in AC and DPC measurements is visible from Figure 6e-h. A change in r of less than 0.02 suggests the standard deviation measurements to be more robust against thickness variations. However, sufficiently high image resolution is required, as only porosity larger than the system resolution will affect the STDV beyond changes in image noise. Consequently, the method is limited to relatively small FOVs. Furthermore, while mean values can theoretically be evaluated pixel-by-pixel, standard deviations must be evaluated in regions significantly larger than the average pore size, which limits detail investigations to some extent.

Figure 5c and Figure 6c show the non-linear relationship between mean DFC values and porosity where specimens with high porosity tend to show weaker correlation. It is likely, that this behavior is caused by the structure size selectivity of the DFC signal which peaks approximately at structure sizes twice the diameter of the autocorrelation length and decreases at larger structure size [36]. Consequently, equal porosity formed by many small pores can cause more scattering than porosity formed by fewer large pores. At autocorrelation lengths of 2 µm and 1.6 µm of the low- and high-res systems used respectively, ideal structure size in direction of sensitivity would be about 3-4 µm. However, 3D-CT data revealed that pores can occasionally accumulate to structures spanning more than 100 µm in direction of sensitivity, which explains weak correlation for high porosity regions in DFC.

The calculation of the nDFC with the measured AC signal (Eq. 2) counteracts this effect to some extent as the AC is not only affected by specimen thickness but porosity as well. Consequently, the nDFC signal in regions or specimens of high porosity is increased while at the same time accounting for variations in specimen thickness.

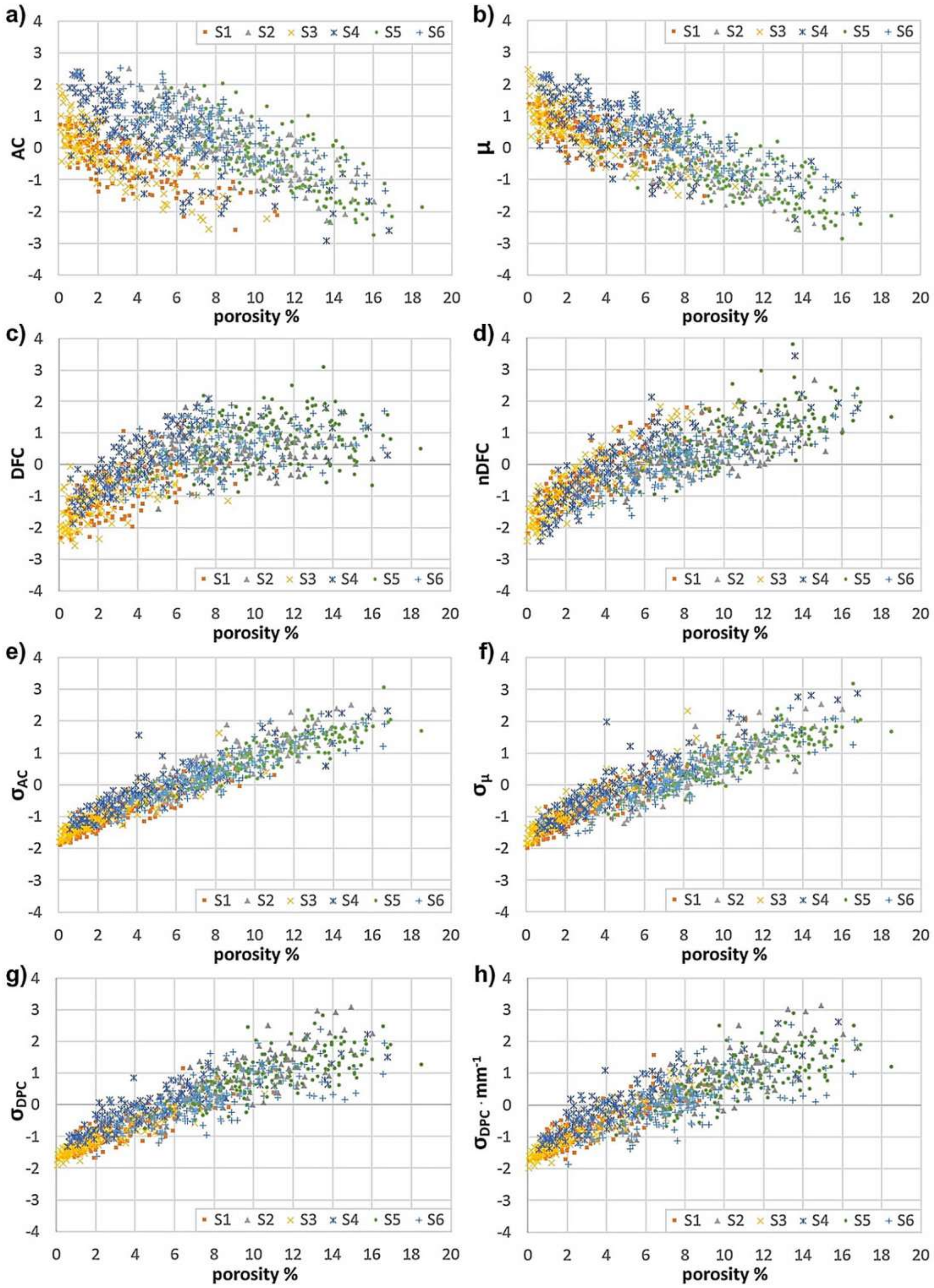

Figure 6: Mean and standard deviation values within each tile evaluated from high-resolution data plotted against porosity. Data is standardized to zero mean and unit standard deviation for comparability. a) Mean AC without correction for specimen thickness. b) Mean AC with correction for specimen thickness (μ). c) Mean DFC without correction for specimen thickness. d) Mean normalized DFC (nDFC). e) Standard

deviation in AC without correction for specimen thickness. f) Standard deviation in AC with correction for specimen thickness (μ). g) Standard deviation in DPC without correction for specimen thickness. h) Standard deviation in DPC with correction for specimen thickness.

The correlation between porosity and (n)DFC could thereby be increased by up to 0.56 as in specimen S2 from r=0.08 to r=0.64. A separate comparison of the effects of the dark-field normalization for individual specimens is shown in Table 3.

	Low-res			**High-res**			
Specimen #	**r_{DFC}**	**r_{nDFC}**	**Δr**	**r_{DFC}**	**r_{nDFC}**	**Δr**	**porosity %**
S1	0.66	0.75	+0.09	0.68	0.84	+0.16	3.43
S2	0.25	0.62	+0.38	0.08	0.64	+0.56	9.11
S3	0.76	0.83	+0.07	0.73	0.85	+0.12	2.58
S4	0.66	0.79	+0.13	0.75	0.88	+0.13	4.54
S5	0.24	0.58	+0.34	0.27	0.71	+0.44	10.73
S6	0.41	0.62	+0.20	0.50	0.79	+0.29	8.72

Table 3: Correlation between porosity and DFC or nDFC respectively for individual specimens. An increase in correlation by normalizing the DFC is especially notable in specimens with high porosity.

The correlation between porosity and AC mean values in comparison is relatively unaffected by total specimen porosity. For specimens with low porosity (< 5%), the nDFC shows stronger correlation than AC. For specimens with high porosity (> 8%) the AC shows stronger correlation. Consequently, the nDFC proved useful primarily for samples with low porosity and pore size, and varying wall thickness, where the AC is impractical without preliminary thickness evaluations.

For modalities that revealed strong correlation (r > 0.65) results were plotted in a color-coded map of evaluated tiles within the regions of interest in Figure 7. Note that the linear absorption coefficient μ correlates negatively with porosity and consequently, colors appear inverted. It is notable, that the nDFC shows strong positive correlation also in low-resolution measurements (r = 0.68).

Due to the directional sensitivity of the grating interferometry method it has to be mentioned that, despite the quasi-isotropic layup of the CFRP, not all porosity contributes to the results equally. Needle shaped pores oriented in direction of sensitivity, i.e., perpendicular to the grating orientation, will evoke less scatter and phase signal. Consequently, the results presented in this paper primarily represent porosity oriented parallel to the gratings, followed by pores oriented in diagonal orientation. This fact might as well reduce the correlation of DFC & DPC modalities, as the compared porosity results consider all porosity equally, regardless of its orientation in space. Therefore, correlation of DFC & DPC modalities with porosity could be more significant for specimens including rather spherically shaped pores. Furthermore, the gratings of the high-resolution TLGI System are not removable, which is why high-res AC is recorded with gratings in the beam path reducing its image quality. Consequently, high-res AC results could possibly be improved by switching to a standard high-resolution X-ray device.

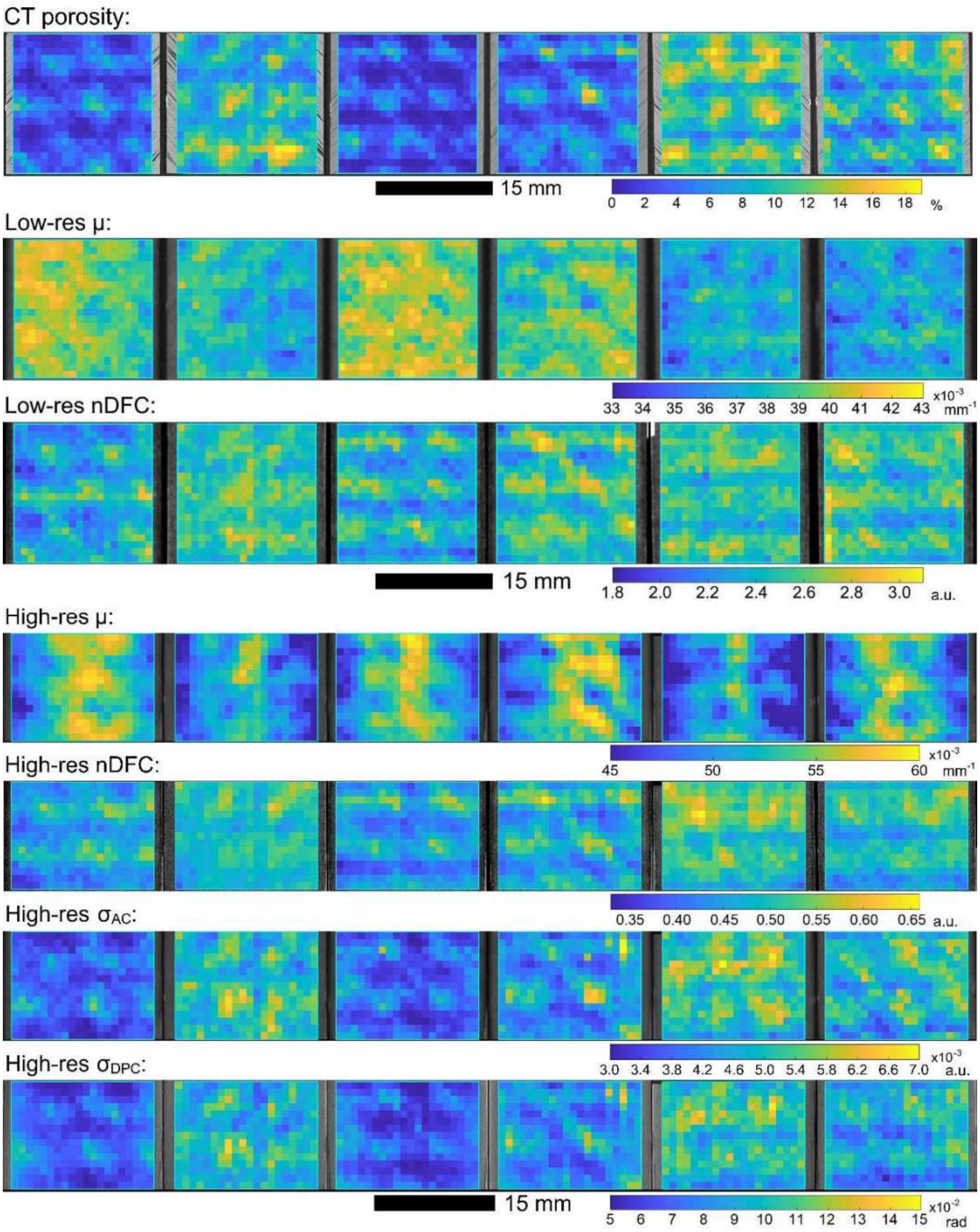

Figure 7: Color coded distribution of porosity and selected modalities evaluated. Only modalities that revealed strong correlation ($r > 0.65$) are shown. Border tiles of High-res measurements are shown in the images but were excluded for evaluations of correlation.

4 Conclusion

We have found that at sufficiently high resolution the standard deviation of the AC is an equally valid measure for the estimation of specimen porosity as is the standard deviation of the DPC. While the AC signal is heavily affected by specimen thickness and preliminary measurements are necessary for correction, results suggest relatively high robustness of standard deviation in AC and DPC against variations in specimen thickness. The DFC signal in comparison can be normalized (nDFC) by the inherently available AC data and shows strong correlation also with porosity of scale below the resolution of the TLGI system. Moreover, compared to the DFC, the nDFC revealed higher sensitivity for porosities above approximately 8% in the case of the specimens investigated. Without the need for high system resolution or preliminary thickness measurements, the nDFC is a promising option for large FOV investigations, currently limited primarily by grating dimensions. However, multiple gratings can be stitched together as demonstrated in [37], to achieve a FOV of 45 cm in width.

5 Acknowledgments

This work was financed by the project "Phad-CT" funded by the federal government of Upper Austria [FFG grant number: 875432].

Data availability

The raw data required to reproduce these findings cannot be shared at this time due to technical or time limitations. The processed data required to reproduce these findings cannot be shared at this time due to technical or time limitations.

APPENDIX

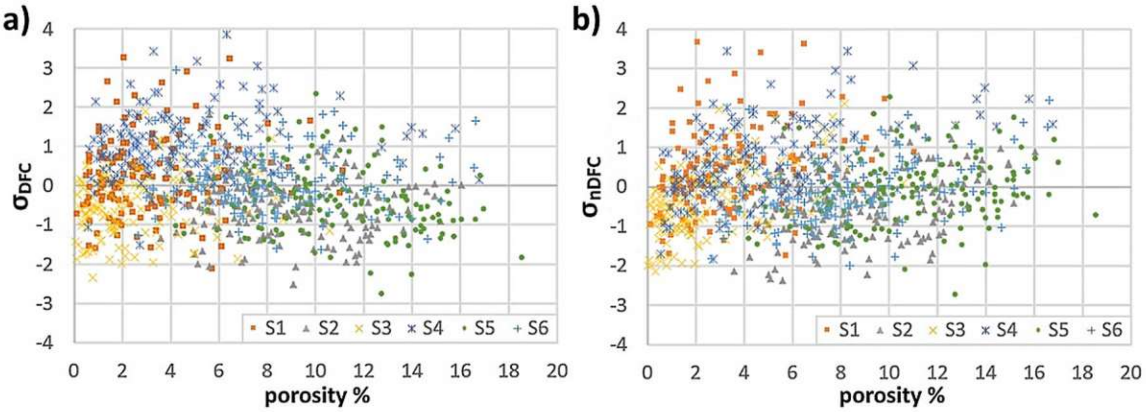

Figure A.1: Standard deviation values evaluated from high-res data plotted against porosity. Data is standardized to zero mean and unit standard deviation. a) High-res DFC without correction for specimen thickness. b) High-res DFC with correction for specimen thickness (nDFC).

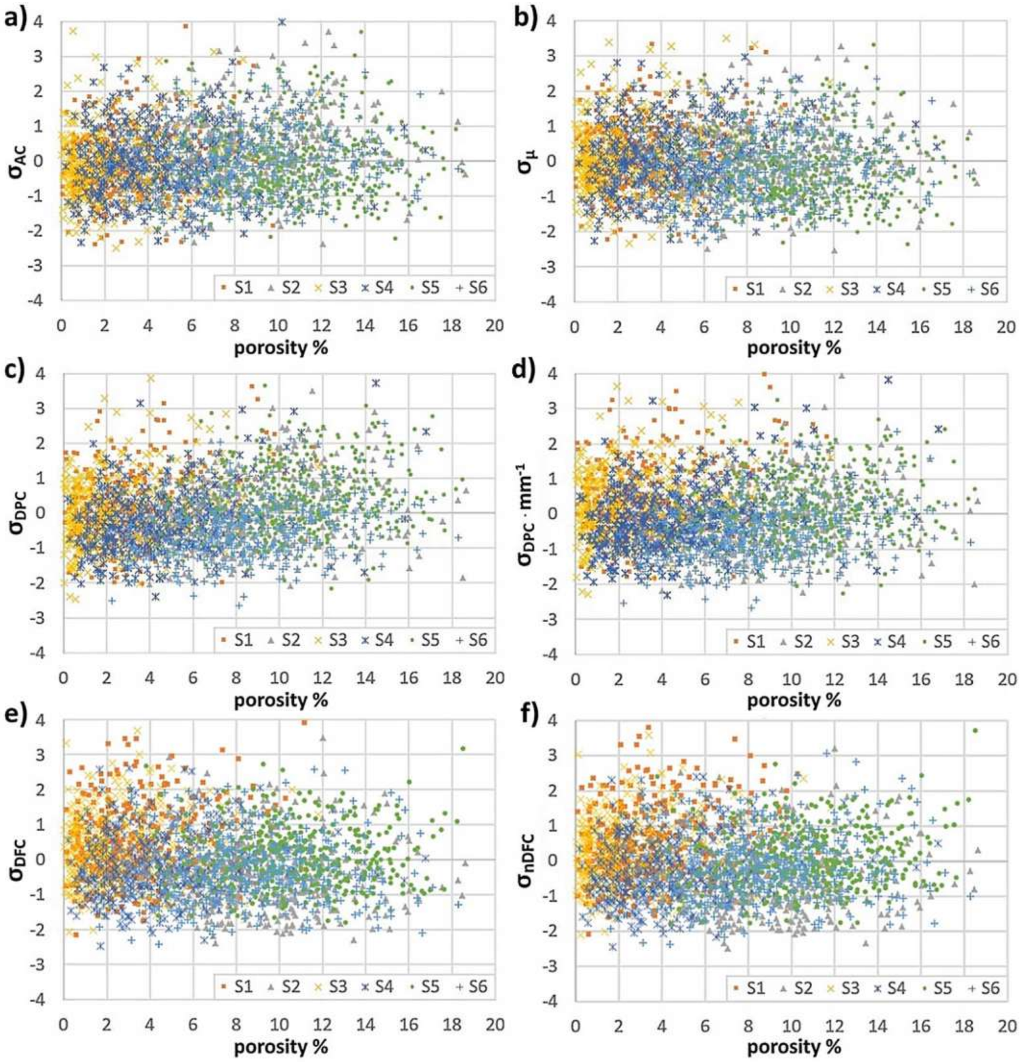

Figure A.2: Standard deviation values evaluated from low-res data plotted against porosity. Data is standardized to zero mean and unit standard deviation. a) Low-res AC without correction for specimen thickness. b) Low-res AC with correction for specimen thickness (μ). c) Low-res DPC without correction for specimen thickness. d) Low-res DPC with correction for specimen thickness. e) Low-res DFC without correction for specimen thickness. f) Low-res DFC with correction for specimen thickness (nDFC).

References

[1] Goertzen WK, Kessler MR. Thermal and mechanical evaluation of cyanate ester composites with low-temperature processability. Compos Part A Appl Sci Manuf 2007;38:779–84. https://doi.org/10.1016/j.compositesa.2006.09.005.

[2] Hillermeier RW, Seferis JC. Environmental effects on thermoplastic and elastomer toughened cyanate ester composite systems. J Appl Polym Sci 2000;77:556–67. https://doi.org/10.1002/(SICI)1097-4628(20000718)77:3<556::AID-APP11>3.0.CO;2-9.

[3] Stamopoulos AG, Tserpes KI, Dentsoras AJ. Quality assessment of porous CFRP specimens using X-ray Computed Tomography data and Artificial Neural Networks. Compos Struct 2018;192:327–35. https://doi.org/10.1016/j.compstruct.2018.02.096.

[4] Hernández S, Sket F, Molina-Aldareguí a JM, González C, LLorca J. Effect of curing cycle on void distribution and interlaminar shear strength in polymer-matrix composites. Compos Sci Technol 2011;71:1331–41. https://doi.org/10.1016/j.compscitech.2011.05.002.

[5] Olivier P, Cottu JP, Ferret B. Effects of cure cycle pressure and voids on some mechanical properties of carbon/epoxy laminates. Composites 1995;26:509–15. https://doi.org/10.1016/0010-4361(95)96808-J.

[6] Mehdikhani M, Gorbatikh L, Verpoest I, Lomov S v. Voids in fiber-reinforced polymer composites: A review on their formation, characteristics, and effects on mechanical performance. J Compos Mater 2019;53:1579–669. https://doi.org/10.1177/0021998318772152.

[7] Stamopoulos AG, Tserpes KI, Prucha P, Vavrik D. Evaluation of porosity effects on the mechanical properties of carbon fiber-reinforced plastic unidirectional laminates by X-ray computed tomography and mechanical testing. J Compos Mater 2016;50:2087–98. https://doi.org/10.1177/0021998315602049.

[8] Bayat S, Jamzad A, Zobeiry N, Poursartip A, Mousavi P, Abolmaesumi P. Temporal enhanced Ultrasound: A new method for detection of porosity defects in composites. Compos Part A Appl Sci Manuf 2023;164. https://doi.org/10.1016/j.compositesa.2022.107259.

[9] Pfeiffer F, Weitkamp T, Bunk O, David C. Phase retrieval and differential phase-contrast imaging with low-brilliance X-ray sources. Nat Phys 2006;2:258–61. https://doi.org/10.1038/nphys265.

[10] Pfeiffer F, Bech M, Bunk O, Kraft P, Eikenberry EF, Brönnimann C, et al. Hard-X-ray dark-field imaging using a grating interferometer. Nat Mater 2008;7:134–7. https://doi.org/10.1038/nmat2096.

[11] Endrizzi M, Diemoz PC, Millard TP, Louise Jones J, Speller RD, Robinson IK, et al. Hard X-ray dark-field imaging with incoherent sample illumination. Appl Phys Lett 2014;104. https://doi.org/10.1063/1.4861855.

[12] Olivo A, Arfelli F, Cantatore G, Longo R, Menk RH, Pani S, et al. An innovative digital imaging set-up allowing a low-dose approach to phase contrast applications in the medical field. Med Phys 2001;28:1610–9. https://doi.org/10.1118/1.1388219.

[13] Revol V, Jerjen I, Kottler C, Schtz P, Kaufmann R, Lthi T, et al. Sub-pixel porosity revealed by x-ray scatter dark field imaging. J Appl Phys 2011;110. https://doi.org/10.1063/1.3624592.

[14] Endrizzi M, Murat BIS, Fromme P, Olivo A. Edge-illumination X-ray dark-field imaging for visualising defects in composite structures. Compos Struct 2015;134:895–9. https://doi.org/10.1016/j.compstruct.2015.08.072.

[15] Senck S, Scheerer M, Revol V, Plank B, Hannesschläger C, Gusenbauer C, et al. Microcrack characterization in loaded CFRP laminates using quantitative two- and three-dimensional X-ray dark-field imaging. Compos Part A Appl Sci Manuf 2018;115:206–14. https://doi.org/10.1016/j.compositesa.2018.09.023.

[16] Senck S, Scheerer M, Revol V, Dobes K, Plank B, Kastner J. Non-Destructive Evaluation of Defects in Polymer Matrix Composites for Aerospace Applications Using X-ray Talbot-Lau Interferometry and Micro CT. 58th AIAA/ASCE/AHS/ASC Structures, Structural Dynamics, and Materials Conference, Grapevine, Texas: 2017, p. 1–9. https://doi.org/10.2514/6.2017-0355.

[17] Glinz J, Šleichrt J, Kytýř D, Ayalur-Karunakaran S, Zabler S, Kastner J, et al. Phase-contrast and dark-field imaging for the inspection of resin-rich areas and fiber orientation in non-crimp vacuum infusion carbon-fiber-reinforced polymers. J Mater Sci 2021;56:9712–27. https://doi.org/10.1007/s10853-021-05907-0.

[18] Glinz J, Thor M, Schulz J, Zabler S, Kastner J, Senck S. Non-destructive characterisation of out-of-plane fibre waviness in carbon fibre reinforced polymers by X-ray dark-field radiography. Nondestructive Testing and Evaluation 2022;37:497–507. https://doi.org/10.1080/10589759.2022.2063860.

[19] Bayer F, Zabler S, Brendel C, Pelzer G, Rieger J, Ritter A, et al. Projection angle dependence in grating-based X-ray dark-field imaging of ordered structures. Opt Express 2013;21:19922. https://doi.org/10.1364/oe.21.019922.

[20] Gusenbauer C, Leiss-Holzinger E, Senck S, Mathmann K, Kastner J, Hunger S, et al. Characterization of medical and biological samples with a Talbot–Lau grating interferometer µXCT in comparison to reference methods. Case Studies in Nondestructive Testing and Evaluation 2016;6:30–8. https://doi.org/10.1016/j.csndt.2016.02.001.

[21] Willner M, Herzen J, Grandl S, Auweter S, Mayr D, Hipp A, et al. Quantitative breast tissue characterization using grating-based x-ray phase-contrast imaging. Phys Med Biol 2014;59:1557–71. https://doi.org/10.1088/0031-9155/59/7/1557.

[22] Gassert FT, Urban T, Frank M, Willer K, Noichl W, Buchberger P, et al. X-ray dark-field chest imaging: Qualitative and quantitative results in healthy humans. Radiology 2021;301:389–95. https://doi.org/10.1148/radiol.2021210963.

[23] Viermetz M, Gustschin N, Schmid C, Haeusele J, von Teuffenbach M, Meyer P, et al. Dark-field computed tomography reaches the human scale. Proceedings of the National Academy of Sciences 2022;119. https://doi.org/https://doi.org/10.1073/pnas.2118799119.

[24] Mayo S, Endrizzi M. X-Ray Phase Contrast Methods. In: Nathan I, Meyendorf N, editors. Handbook of Advanced Non-Destructive Evaluation, Springer, Cham; 2018, p. 1–42. https://doi.org/https://doi.org/10.1007/978-3-319-30050-4_54-1.

[25] Momose A. Recent advances in X-ray phase imaging. Japanese Journal of Applied Physics, Part 1: Regular Papers and Short Notes and Review Papers 2005;44:6355–67. https://doi.org/10.1143/JJAP.44.6355.

[26] Birnbacher L, Braig EM, Pfeiffer D, Pfeiffer F, Herzen J. Quantitative X-ray phase contrast computed tomography with grating interferometry: Biomedical applications of quantitative X-ray grating-based phase contrast computed tomography. Eur J Nucl Med Mol Imaging 2021;48:4171–88. https://doi.org/10.1007/s00259-021-05259-6.

[27] Glinz J, Zabler S, Kastner J, Senck S. Metal Artifacts in Attenuation and Phase Contrast X-Ray Microcomputed Tomography: A Comparative Study. Exp Mech 2022;62:837–47. https://doi.org/10.1007/s11340-022-00835-9.

[28] Chabior M, Donath T, David C, Bunk O, Schuster M, Schroer C, et al. Beam hardening effects in grating-based x-ray phase-contrast imaging. Med Phys 2011;38:1189–95. https://doi.org/https://doi.org/10.1118/1.3553408.

[29] Shoukroun D, Olivo S, Fromme P. Edge Illumination X-Ray Phase Contrast Imaging and Ultrasonic Attenuation for Porosity Quantification in Composite Structures. 48th Annual Review of Progress in Quantitative Nondestructive Evaluation 2021. https://doi.org/10.1115/QNDE2021-75009.

[30] Plank B, Mayr G, Reh A, Kiefel D, Stoessel R, Kastner J. Evaluation and Visualisation of Shape Factors in Dependence of the Void Content within CFRP by Means of X-ray Computed Tomography. 11th European Conference on Non-Destructive Testing 2014.

[31] Plank B, Sause MGR, Kastner J. High-resolution X-ray computed tomography simulations of synthetically-generated volume porosity in continuous carbon fibre-reinforced polymer samples. Nondestructive Testing and Evaluation 2022;37:645–65. https://doi.org/10.1080/10589759.2022.2086547.

[32] Revol V, Kottler C, Kaufmann R, Jerjen I, Lüthi T, Cardot F, et al. X-ray interferometer with bent gratings: Towards larger fields of view. Nucl Instrum Methods Phys Res A 2011;648:302–5. https://doi.org/10.1016/j.nima.2010.11.040.

[33] Weitkamp T, Diaz A, David C, Pfeiffer F, Stampanoni M, Cloetens P, et al. X-ray phase imaging with a grating interferometer. Opt Express 2005;13:6296–304. https://doi.org/10.1364/OPEX.13.006296.

[34] Wang Z, Stampanoni M. Quantitative x-ray radiography using grating interferometry: A feasibility study. Phys Med Biol 2013;58:6815–26. https://doi.org/10.1088/0031-9155/58/19/6815.

[35] Ludwig V, Seifert M, Niepold T, Pelzer G, Rieger J, Ziegler J, et al. Non-destructive testing of archaeological findings by grating-based X-ray phase-contrast and dark-field imaging. J Imaging 2018;4. https://doi.org/10.3390/jimaging4040058.

[36] Lynch SK, Pai V, Auxier J, Stein AF, Bennett EE, Kemble CK, et al. Interpretation of dark-field contrast and particle-size selectivity in grating interferometers. Appl Opt 2011;50:4310–9. https://doi.org/10.1364/AO.50.004310.

[37] Viermetz M, Gustschin N, Schmid C, Haeusele J, von Teuffenbach M, Meyer PBF, et al. Dark-field computed tomography reaches the human scale. Proceedings of the National Academy of Sciences 2022;119. https://doi.org/https://doi.org/10.1073/pnas.2118799119.

5.5 Summary

In light of the ongoing importance of a sustainable use of resources in the transportation sector, fiber-reinforced polymers continue to experience increasing popularity in the automotive and aerospace industries due to their potential for weight reduction and associated CO2 savings. The demands on these composite structures are also increasing, with ever more complex designs and, for example, the integration of embedded electronics for in-service monitoring. Due to this complexity, as well as the susceptibility of fiber-reinforced polymers to invisible damages (e.g., those originating from manufacturing errors or impact damage during operation), monitoring via non-destructive testing throughout the entire life cycle is required. However, the typically large scale of automotive and aerospace components makes the detection and characterization of (sub-) micron defects challenging, and new methods of non-destructive investigation are still sought in industry.

In the recent years, Talbot-Lau grating interferometry (TLGI) has proven to be a promising technology for medical applications, which typically feature low-density and low-atomic-number materials. However, practical applications for industrial materials are still scarce, mostly due to the restrictions in field-of-view and applicable X-ray energy, as well as the lack of standard protocols. Consequently, the aim of this thesis was to explore the possibilities and develop new methods for the application of TLGI to industrial lightweight materials, such as carbon-fiber-reinforced polymers.

Two scientific papers were published focusing on the three-dimensional investigation of composites via full TLGI X-ray computed tomography (XCT), followed by two additional papers demonstrating the potential of two-dimensional TLGI radiographic imaging. The first paper showed how complementary phase contrast (DPC) and dark-field contrast (DFC) data can be evaluated for increased contrast of resin-rich areas and additional information on fiber orientation within resin transfer-molded specimens, respectively. Using the extracted DFC data, the layer sequence of the specimens oriented in four main directions was evaluated, while the increased contrast within the DPC data allowed for a three-dimensional visualization of resin-rich areas. By combining both modalities, the resin-rich areas could be differentiated into intra-layer and inter-layer resin-rich areas, predominantly caused by binder yarn collimation and fiber waviness, respectively. Additionally, DFC imaging also proved useful for identifying resin-rich areas since the lack of fibers in those regions results in a significantly reduced scattering signal.

The next comparative study explored the effects of beam hardening in a metal-polymer composite on image data recorded with X-ray attenuation and X-ray phase contrast computed tomography. It showed that the reduced sensitivity of phase contrast imaging to beam hardening effects can be utilized for the investigation of components including metallic features (e.g., those from embedded electronics) to improve metal artifacts. However, attenuation-based XCT combined with hardware pre-filtering of the X-ray beam and additional post-processing by metal artifact reduction algorithms has shown reasonable results as well. Nevertheless, hardware pre-filtering typically leads to worse image noise, which often requires a compromise between noise and effective artifact reduction. Furthermore, phase contrast imaging showed superior artifact reduction in close proximity to highly dense metallic inserts, which allows for a more detailed investigation of metal-polymer interfaces.

In contrast to full XCT scanning of a specimen, the method introduced in the third publication relies on two-dimensional radiographic imaging to reduce measurement times and enable investigation of relatively large components. It demonstrated how the directional sensitivity of the DFC can be utilized for detecting and characterizing out-of-plane fiber waviness, a manufacturing defect frequently encountered in fiber-reinforced composites that can severely degrade the mechanical strength of a component. The procedure was found to be capable of detecting fiber waviness and quantifying the maximum wave angle by recording a series of projection images in the low two-digit range. Compared to full computed tomography scans, which typically require hundreds of projection images, a significant reduction in measurement time was achieved, while wave angles within the test specimens were quantified with an error of less than ± 1.5° in comparison to results from full XCT data.

Finally, within the fourth contribution, a study on the effects of porosity in cyanate ester carbon-fiber-reinforced polymer on all three modalities captured by TLGI radiographic testing was presented. Porosity in composites can be caused by various origins and has been shown to be a major factor influencing component strength, rendering methods for fast and non-destructive investigation invaluable for the qualification of aerospace components. Consequently, this work demonstrated how the complementary modalities extracted by TLGI can provide additional insights compared to standard attenuation contrast radiography alone. While the mean intensity of the attenuation contrast is heavily affected by specimen thickness and preliminary measurements are necessary for correction, the results of the study suggested relatively high robustness against variations in specimen thickness of the standard deviation in both the attenuation and differential phase contrast. Furthermore, at sufficiently high resolution, the standard deviation within the phase contrast correlated equally well with specimen porosity, as did the standard deviation within the attenuation contrast. Although the dark-field contrast was also affected by changes in specimen thickness, the signal could be corrected by normalization with the inherently available attenuation contrast. Therefore, a strong positive correlation with porosity was found both in high- and low-resolution imaging without the need for preliminary thickness measurements. Consequently, the high sensitivity to microporosities of size below the actual image resolution, in combination with the low sensitivity to variations in specimen thickness, renders the normalized DFC a promising option for large field-of-view investigations.

In conclusion, this thesis covered four studies on the application of TLGI for lightweight materials, introducing new methods and providing insights for industrial application. These include full TLGI-XCT for a three-dimensional, in-depth characterization of specimens as well as fast, two-dimensional radiographic testing enabling the investigation of larger components.

5.6 Outlook

Although the low requirements in spatial resolution qualify the presented methods for the investigation of larger components, most experimental investigations were performed only on token-sized specimens. One of the reasons for this is the limited dimensions of standard-sized gratings implemented in the TLGI systems that were utilized throughout the studies of this thesis. For most industrial applications, a larger field-of-view (FOV) is desirable, and although recent publications have demonstrated how stitching several gratings can increase the FOV to a width of about 45 cm [91,94], standardized methods do not yet exist.

Nevertheless, the method presented for two-dimensional investigation of out-of-plane fiber waviness characterizes components under a shallow angle with respect to the direction of X-ray propagation. Consequently, a region of a component much wider than the actual width of the FOV can possibly be captured within a single projection image. Preliminary results have shown that a plate of 3 cm height and 13 cm width can easily be characterized within a FOV of 4 by 4 cm. Another outlook for the investigation of fiber waviness is the application for components manufactured from sheets of woven fibers and/or isotropically oriented long fibers, as current experiments were limited to specimens from unidirectional prepreg fibers.

Furthermore, the reduced sensitivity of phase contrast imaging has been shown capable of reducing beam hardening effects. However, severe phase wrapping artifacts deteriorate the image quality, which was not accounted for in the present study. Consequently, by applying an additional phase wrapping correction algorithm, the image quality of the DPC could be further increased.

Curriculum Vitae

Name: Jonathan Glinz
Address: [redacted]
Phone: [redacted]
E-Mail: [redacted]

■ Education

Since 2019	**PhD Study** Technical University Vienna Institute of Materials Science and Technology **PhD Thesis:** „Quantitative Phasen- und Dunkelfeld-Kontrast - Computertomografie für industrielle Anwendungen an Leichtbauwerkstoffen“
2014 - 2016	**MSc in Healthcare and Rehabilitation Technology** FH Technikum Wien **Master Thesis:** Simulation of Muscle Spindle Responses and Behavior during Coupling with Extrafusal Muscle under Central Nervous System Control.
2011 - 2014	**BSc in Biomedical Engineering** FH Technikum Wien **Bachelor Thesis:** Development of an EMG-Electrode Array for TMR patients.
2005 - 2010	**Mechanical Engineering** HTL St. Pölten

■ Research and professional experience

Since 2020	**Part-time teaching** FH OÖ Studienbetriebs GmbH **Course:** New technologies in materials analysis and characterization
Since 2017	**Research Associate** FH OÖ Research & Development GmbH Research Group Computed Tomography
01/2014 – 06/2014	**Otto Bock Healthcare Products GmbH** Strategic technology management

■ Peer reviewed journal publications

[1] **Glinz, J**., Šleichrt, J., Kytýř, D. et al. Phase-contrast and dark-field imaging for the inspection of resin-rich areas and fiber orientation in non-crimp vacuum infusion carbon-fiber-reinforced polymers. J Mater Sci 56, 9712–9727 (2021). https://doi.org/10.1007/s10853-021-05907-0

[2] **Glinz, J**., Zabler, S., Kastner, J. et al. Metal Artifacts in Attenuation and Phase Contrast X-Ray Microcomputed Tomography: A Comparative Study. Exp Mech (2022). https://doi.org/10.1007/s11340-022-00835-9

[3] **Glinz, J.**, Thor, M., Schulz, J., Zabler, S., Kastner, J., & Senck, S. (2022). Non-destructive characterisation of out-of-plane fibre waviness in carbon fibre reinforced polymers by X-ray dark-field radiography. Nondestructive Testing and Evaluation, 37(5), 497-507. https://doi.org/10.1080/10589759.2022.2063860

[4] **Glinz, J.**, Plank, B., Gutekunst, J., Scheerer, M., Zabler, S., Kastner, J., Senck, S., Non-destructive investigation of porosity in carbon fiber reinforced cyanate ester by grating interferometry-based X-ray radiography, 2023 (under review @ Composite Structures)

[5] **Glinz, J.**, Maurer, J., Holzleitner, M., Pace, F., Stamopoulos, A., Vopalensky, M., Kumpova, I., Eckl, M., Kastner, J., Senck, S., Fast Continuous In-Situ XCT of Additively Manufactured Carbon Fiber Reinforced Tensile Test Specimens, Acta Polytechnica CTU Proceedings, 2023 (Accepted)

[6] Pace, F., Stamopoulos, A., Eckl, M., Senck, S., **Glinz, J.**, Analysis of the Manufacturing Porosity in Additively Manufactured Onyx/Long Fiber Reinforced Composites Using X-Ray Computed Tomography. J Nondestruct Eval 42, 86 (2023). https://doi.org/10.1007/s10921-023-01000-5

[7] **Glinz, J.**, Kytýř D, Fíla T, Šleichrt J, Schrempf A, Fürst D, et al. In-situ compression test of artificial bone foams in controlled environment using X-ray micro-computed tomography. Acta Polytechnica CTU Proceedings, 2019, 25, 48–51. https://doi.org/10.14311/APP.2019.25.0048

[8] Kiss, P., **Glinz, J**., Stadlbauer, W., Burgstaller, C., Archodoulaki, V.-M. The Effect of Thermally Desized Carbon Fibre Reinforcementon the Flexural and Impact Properties of PA6, PPS and PEEK Composite Laminates: A Comparative Study. Compos. Part B Eng.2021, 215, 108844. https://doi.org/10.1016/j.compositesb.2021.108844

[9] Kastner, J., Gusenbauer, C., Plank, B., **Glinz, J.**, Senck, S., Challenges for grating interferometer X-ray computed tomography for practical applications in industry, Insight - Non-Destructive Testing and Condition Monitoring, Vol. 61(3), pp. 149-152. https://doi.org/10.1784/insi.2019.61.3.149

[10] Trieb, K., **Glinz, J.**, Reiter, M., Kastner, J., Senck, S. (2019) Non-Destructive Testingof Ceramic Knee Implants Using Micro-Computed Tomography.J Arthroplasty. 34:2111–2117. https://doi.org/10.1016/j.arth.2019.05.006

[11] Senck, S., Happl, M., Reiter, M., Scheerer, M., Kendel, M., **Glinz, J.**, Kastner, J. (2020) Additive manufacturing and non-destructive testing of topology-optimised aluminium components, Nondestructive Testing and Evaluation, 35:3, 315-327, https://doi.org/10.1080/10589759.2020.1774582

[12] Šleichrt, J., Fíla, T., Koudelka, P., Adorna, M., Falta, J., Zlámal, P., **Glinz, J.**, Neuhäuserová, M., Doktor, T., Mauko, A., Kytýř, D., Vesenjak, M., Duarte, I., Ren, Z., Jiroušek, O., Dynamic penetration of cellular solids: Experimental investigation using Hopkinson bar and computed tomography. Materials Science and Engineering A 2021;800. https://doi.org/10.1016/j.msea.2020.140096.

■ Conference proceedings publications

[1] **Glinz, J.**, Pace, F., Maurer, J., Vopálenský, M., Kumpová, I., Eckl, M., Stamopoulos, A., Kastner, J., Senck, S., Influence of continuous fiber reinforcement on tensile properties in fused filament fabricated specimens, AIAA SciTech Forum 2023, https://doi.org/10.2514/6.2023-2199

[2] Gutekunst, J., Fettig, R., Schulz, J., **Glinz, J.**, Advancing research and education with simple setup Talbot-Lau-Interferometers, Proceedings of 12th Conference on Industrial Computed Tomography (iCT) 2023, Fürth, Germany, 2023

[3] **Glinz, J.**, Kastner, J., Šleichrt, J., Schulz, J., Eckl, M., Kytýr, D., Ayalur-Karunakaran, S., Senck, S., 3D-characterization of composite materials by Talbot-Lau grating interferometer radioscopy and computed tomography, 13th European Conference on Non-Destructive Testing, Lisbon, Portugal, 2023 (poster + talk)

[4] Maurer, J., Heupl, S., Kendel, M., Holzleitner, M., **Glinz, J.**, Senck, S., Auer, J., Kastner, J., MIST – Mechanical In-situ Stage with Temperature control for X-ray computed tomography, Proceedings of 12th Conference on Industrial Computed Tomography (iCT) 2023, Fürth, Germany, 2023

[5] Senck, S., Miloradovic, A., Holzleitner, M., **Glinz, J.**, Kastner, J., Koutny, D., Gneiger, S., Wire Arc Additive Manufacturing (WAAM) and microstructural analysis of Magnesium parts, Proceedings of 12th Conference on Industrial Computed Tomography (iCT) 2023, Fürth, Germany, 2023

[6] **Glinz, J.**, Reiter, M., Gastinger· T., Kytýř, D., Huskic, A., Plank, B., Kastner, J., Senck, S. (2022). Image quality metrics for 3D-printed titanium parts: A feasibility study. iCT 2022: 11th International Conference on Industrial Computed Tomography, Wels, Österreich (Poster)

[7] **Glinz, J.**, Maurer, J., Eckl, M., Kastner, J., & Senck, S. (2022). In-situ characterization of additively manufactured continuous fiber reinforced tensile test specimens by X-ray computed tomography. in AIAA SciTech Forum 2022 [AIAA 2022-1426], American Institute of Aeronautics and Astronautics Inc. (AIAA). https://doi.org/10.2514/6.2022-1426

[8] **Glinz, J.**, Thor, M., Eckl, M., Schulz, J., Kastner, J., Senck, S., Detection and quantification of out-of-plane fiber waviness by X-ray dark-field radiography, 5th International Conference on Tomography of Materials & Structures, Grenoble, France, 2022 (Poster + talk)

[9] Frank, M., Mrozek, D., **Glinz, J.**, Senck, S., & Hinterhölzl, R. M., Build quality analysis of additively manufactured locally endless fiber reinforced polyamide. 20th European Conference on Composite Materials (ECCM20), Lausanne, Schweiz.

[10] Nafre, A., **Glinz, J.**, Schulz, J., & Senck, S. (2022). TALINT grating kits for X-ray interferometry in the industrial laboratory. in 11th Conference on Industrial Computed Tomography (S. 1-9)

[11] Hinterhölzl, R., Shehata, K., Sendner, F., Wolfahrt, M., Schneiderbauer, G., **Glinz, J.**, Semlitsch, K., Thor, M., Design for innovative and cost-efficient manufacturing of composite sandwich structures with foam molded cores for high-rate production of wing movables. 20th European Conference on Composite Materials (ECCM20), Lausanne, Schweiz

[12] Höglinger, M., Plank, B., **Glinz, J.**, Schulz, J., Heinzl, C., & Kastner, J. (2021). Multimodale und Multiskalare dreidimensionale Materialcharakterisierung von faserverstärkten Kunststoffen mit Röntgen-Computertomografie (Poster)

[13] **Glinz, J.**, Thor, M., Ayalur Karunakaran, S., Kastner, J., & Senck, S. (2021). Inspection of fiber waviness in carbon fiber laminates by talbot-lau x-ray grating interferometry. in AIAA SciTech 2021 Forum (S. 1-8), American Institute of Aeronautics and Astronautics Inc. (AIAA). https://doi.org/10.2514/6.2021-0064

[14] Senck, S., **Glinz, J.**, Happl, M., Scheerer, M., Reiter, T., & Kastner, J. (2021). Quantification of surface-near porosity in additively manufactured aluminum brackets using x-ray microcomputed tomography. in AIAA Scitech 2021 Forum (S. 1-7), American Institute of Aeronautics and Astronautics Inc. (AIAA). https://doi.org/10.2514/6.2021-0536

[15] **Glinz, J.**, Senck, S., Plank, B., Spindler, C., Kastner, J., & Röper, F. (2020). Assessment of CFRP fiber lay-up and orientation using small-angle X-ray scattering CT. iCT 2020: 10th International Conference on Industrial Computed Tomography, Wels, Österreich (Poster)

[16] Trieb, K., **Glinz, J.**, Reiter, M., Kastner, J., & Senck, S. (2020). Micro-computed tomography for non-destructive testing of ceramic knee implants. 1-4. iCT 2020: 10th Conference on Industrial Computed Tomography, Wels, Österreich (Poster)

[17] Röper, F., Plank, B., **Glinz, J.**, Wolfahrt, M., Kucher, G., & Pinter, G. (2020). X-ray computed tomography in bonded aircraft repairs for composites. in Proceedings of 10th Conference on Industrial Computed Tomography (iCT) 2020 (S. 1-6).

[18] Senck, S., Weißenbacher, P., **Glinz, J.**, Kastner, J., Hofstaetter, S. G., & Trieb, K. (2019). Eine neue Methode zur Berechnung der Kortikalis- und Knorpeldicke im arthrotischen Kniegelenk mittels Mikro-Computertomographie und deformationsbasierter Morphometrie. 1-1. Beitrag in 35. Jahrestagung der Österreichischen Gesellschaft für Orthopädie und orthopädische Chirurgie, Wels, Österreich.

[19] da Cunha Melo, L., Fröhler, B., **Glinz, J.**, Kastner, J., & Heinzl, C. (2019). Exploration of Talbot-Lau Grating Interferometry Computed Tomography Data by Interactive Transfer Function Combination. Abstract von 5th International Conference on X-ray and Neutron Phase Imaging with Gratings (XNPIG), Sendai (Japan), Japan.

[20] Senck, S., **Glinz, J.**, Plank, B., Schrempf, A., Haider, A., & Kastner, J. (2019). Grating-based dark-field imaging of additively manufactured carbon fiber reinforced composite parts. 1-2. Abstract von 5th International Conference on X-ray and Neutron Phase Imaging with Gratings (XNPIG), Sendai (Japan), Japan.

[21] **Glinz, J.**, Senck, S., Reiter, M., Schrempf, A., Fürst, D., & Kastner, J. (2019). Improved Visualization of Polymer Foams using Talbot-Lau Grating Interferometry to Reduce Metal Artifacts. in Proceedings of Symposium on Digital Industrial Radiology and Computed Tomography (DIR2019), Fürth (S. 1-9)

[22] **Glinz, J.**, Senck, S., Plank, B., Spindler, C., Kastner, J., & Röper, F. (2019). Inspection of patch repaired carbon-fiber reinforced polymers using Talbot-Lau grating interferometry. in XNPIG 2019 (Poster)

[23] Senck, S., Šleichrt, J., Plank, B., **Glinz, J.**, Kastner, J., Ayalur-Karunakaran, S., & Kytýř, D. (2019). Multi-modal characterization of CFRP samples produced by resin infusion using phase contrast and dark-field imaging. 1-2. Abstract von International Conference on Tomography of Materials & Structures, Cairns, Australien.

[24] **Glinz, J.**, Reiter, M., Gastinger, T., Huskic, A., Plank, B., Kastner, J., & Senck, S. (2019). Porosity determination in additively manufactured Ti parts using X-ray tomography. in 9th International Conference on Industrial Computed Tomography (iCT) 2019 (S. 1-7)

[25] Kastner, J., Gusenbauer, C., Plank, B., **Glinz, J.**, & Senck, S. (2018). Challenges for grating interferometer X-ray computed tomography for practical applications in industry. in Proceedings of the 12th European Conference on Non-destructive Testing

[26] **Glinz, J.**, Weißenbacher, P., Senck, S., Schrempf, A., Fürst, D., Gastinger, T., Huskic, A., Reiter, T., & Kastner, J. (2018). Determination of pore size distribution and finite element analysis of additively manufactured Ti pedicle screws using X-ray microcomputed tomography. in Proceedings of the 12th European Conference on Non-destructive Testing (S. 1-8)

[27] **Glinz, J.**, Senck, S., Kastner, J., & Tondi, G. (2018). Determination of pore size distribution in Tannin- and Lignin-based foams using Xray microcomputed tomography. in Proceedings of the 8th Conference on Industrial Computed Tomography, Wels, Austria (iCT 2018) (S. 1-7)

[28] Kastner, J., Heinzl, C., & **Glinz, J.** (2018). X-ray computed tomography for applications in industry and materials science. in Proceedings of the 57th Annual British Conference on Non-Destructive Testing (S. 1-12)